CONTROL SYSTEM DESIGN FOR NANOMETER SCALE POSITIONING SYSTEMS

FRANK JAMES GOFORTH

Bachelor of Science in Electrical Engineering

Massachusetts Institute of Technology

June, 1977

Master of Science in Industrial Engineering

Cleveland State University

May, 2000

submitted in partial fulfillment of requirements for the degree

DOCTOR OF ENGINEERING

at the

CLEVELAND STATE UNIVERSITY

May, 2006

This dissertation has been approved
for the Department of Electrical and Computer Engineering
and the College of Graduate Studies by

____

Dissertation Committee Chairperson, Dr. Zhiqiang Gao

Department & Date

Dr. Dan Simon

Department & Date

Dr. Ana Stankovic

Department & Date

Dr. Lili Dong

Department & Date

Dr. Hanz Richter

Department & Date

Dr. Nolan Holland

Department & Date

Dr. Sally Shao

Department & Date

ACKNOWLEDGEMENT

I must thank my dissertation advisor, Dr. Zhiqiang Gao, for his encouragement, guidance and instruction. I am also grateful for the support and patience of my dissertation committee members, Dr. Dan Simon, Dr. Ana Stankovic, Dr. Lili Dong, Dr. Hanz Richter, Dr. Nolan Holland and Dr. Sally Shao.

I must extend special appreciation to Dr. Xiaobo Tan, Assistant Professor, Michigan State University and Dr. Kam Leang, Assistant Professor, Virginia Commonwealth University for the gracious use of their hysteresis model measurement data used in the construction of my simulation.

I must extend my profound appreciation to Dr. Pavel Krejci, Academy of Sciences of the Czech Republic, for enthusiastically providing me a rare copy of his widely referenced and impossible to obtain book, “Hysteresis, Convexity and Dissipation in Hyperbolic Equations”. This information was critical to my understanding of hysteresis and the analysis of stability using the Active Disturbance Rejection Control.

Most importantly, I owe my eternal gratitude to my spouse, Lynn Lilly, who has been steadfast and patient these past four years. I am blessed.

CONTROL SYSTEM DESIGN FOR NANOMETER SCALE POSITIONING SYSTEMS

FRANK JAMES GOFORTH

ABSTRACT

Nanometer positioning presents unique challenges because devices capable of this accuracy exhibit hysteretic behavior. Hysteresis is characterized by rate independent memory and multi-valued output, limiting even the application of nonlinear control. Previous researchers have pursued a control strategy dependent on precision models of hysteresis. The physical principles of these hysteretic devices are not well understood and the models exhibiting best fidelity to experimental evidence are phenomenological, not analytic, thus they are computationally intensive for reasonable accuracy and their behavior is unique to each device.

Our thesis is that one may treat hysteretic behavior as a disturbance and compensate for it as one would for other disturbance. Three hysteresis compensation strategies are demonstrated which exhibit performance superior to prior reported results and none of which require a hysteresis model. Novel passive and active disturbance rejection strategies, as well as a hybrid combination inheriting favorable characteristics of both strategies, are successfully developed and implemented.

TABLE OF CONTENTS

NOMENCLATURE

Abbreviations

ADRC: Active Disturbance Rejection Control

AFM: Atomic Force Microscope

BIBO: Bounded Input Bounded Output

CTOC: Continuous Time Optimal Control

DOB: Disturbance Observers

DTOC: Discrete Time Optimal Control

ESO: Extended State Observer

H_∞: H infinity

IR: Isochronic Region

LTI: Linear Time Invariant

PID: Proportional Integral Derivative

PZT: Lead Zirconate Titanate

TD: Tracking Differentiator

TOC: Time Optimal Control

UUT: Unit Under Test

Symbols

X_m: Mechanical Strain

x_m: Mechanical Stress

d_{em}: Piezoelectric Strain Coefficient relates electrical Polarization, P_e, to mechanical strain X_m.

e_{em}: Piezoelectric Stress Coefficient relates electrical Polarization, P_e, to mechanical stress x_m.

s_{mn}: Elastic compliance coefficient.

c_{mn}: Elastic stiffness coefficient.

E: Electric field.

D: Electric displacement.

P: Electric polarization.

ε: Dielectric permittivity

Y: Young's elastic modulus = tensile stress/ tensile strain.

ρ: Material density

λ_n: Wavelength of n^{th} harmonic.

ω_n: Frequency in radians of n^{th} harmonic.

ζ_n: Damping ratio of n^{th} harmonic.

f_n: Frequency in Hertz of n^{th} harmonic.

c_n: Wave velocity of n^{th} harmonic.

Q_n: Quality factor of n^{th} harmonic.

LIST OF FIGURES

Figure **Page**

CHAPTER 1

INTRODUCTION

The 20th century saw the transition from macro to micro scale precision in measurement and control. The 21st century begins with the inevitable step to the nanometer scale. But this is not an easy step, for one now stands on the threshold of quantum physics. One leaves the relatively weak Newtonian mechanics forces behind and moves into the uncertain realm of the strong atomic forces. Model-based controls will not likely, and certainly not easily, make this transition.

Nanometer scale research requires new tools to yield its potential, and positioning at this scale is an early challenge. The Atomic Force Microscope (AFM) is today the most common tool for measuring and/or manipulating nanometer scale objects. It is the tool of choice for research in semiconductors, nano biology, nano materials, etc. As such it provides a leading edge reference for the study of nanometer scale positioning control. The AFM vividly illustrates measurement and control technology must be reevaluated at a fundamental level because many of the advancements at the macro and micro scale in the past century have led to assumptions which are no longer valid.

Sensor dynamics are again significant, if not critical, components of the control loop. Mechanical disturbances of very minor consequence at macro, or even micro scale, now overwhelm the sensors, not to mention their effect on tool holders and samples measured in micro and nano grams. Nano sensors are significantly disturbed by footsteps, even when mounted on anti-vibration tables, on a concrete slab, in the basement. Disturbances are easily nano scale. Radio frequency radiation is more prevalent today with wireless connections ubiquitous, so while meters of displacement requires amps of current at the human scale, this does not scale well to nano amps with so many noise sources available. Thermal noise can deflect tools hundreds of nanometers, requiring hourly recalibration of an AFM using linear controls. Mechanical tolerance buildup, not to mention thermal expansion and contraction, imply energy must be directly converted to mechanical displacement for nanometer scale precision, no intervening transmission medium has been found acceptable. So, as the distance becomes smaller by three orders of magnitude, the problems scale in inverse proportion.

Piezoceramic actuators are used for both cantilever oscillator and sample scanner for the AFM because they leverage relatively large voltages and forces to small distances, thus providing manageable signal/noise ratios. They convert energy directly to small displacement, and generate significant force relative to their mass, so a mismatch with their load is to be expected. They also exhibit some of the nonlinear control issues shared with other sensor/actuator materials capable of meeting the nanometer scale challenges. Piezo ceramics generate displacement via strain in their crystalline structure, and thus their axes motion is highly coupled. Their electrical properties vary significantly with temperature. They operate due to their polarization, which can change due to voltage “creep”. And, common to many useful devices at every scale, they exhibit significant hysteresis, but whereas thermal drift and voltage creep are relatively slow, hysteresis affects motion at the desired operating frequencies.

The Primary Challenge: Hysteresis

During the course of research it became apparent hysteresis would be the most difficult and interesting challenge to face in nanometer positioning, and also provided a topic that had much broader impact. It is a critical challenge for so many processes, whether mechanical, thermal, chemical, pressure, flow, etc. so it was natural to concentrate on this nonlinearity. Hysteresis exhibits rate independent behavior and non local memory, its output is multi valued and so not conducive to straightforward methods of linear or nonlinear analysis and control. The piezo ceramic actuator as used in the AFM will be used as the example medium for study, but as will be seen, our results are more broadly applicable to hysteretic processes in general, and thus open the door wider for future research opportunities.

Controlling hysteretic piezo ceramic devices has been a low bandwidth compromise to date. A precision model-based linearization using either series inversion or feed forward compensation has been the rule, and as will be shown, precision of modeling has differentiated performance in control. Unfortunately, each hysteretic device is unique, and with no first principle knowledge to guide the process the models are empirical, by necessity. In most all examples of nanometer scale positioning, of which there are still relatively few, linear control methods have been used, sometimes with the addition of nonlinear adaptive tuning. It seemed natural, in this environment, to study the Active Disturbance Rejection Controller (ADRC), using the Extended State Observer (ESO), as a plausible solution. The present dependency on unique precision modeling for control and the highly disturbing environment matches the strengths previously exhibited by the ADRC addressing these challenges at the macro scale. The historical effectiveness of “dithering” a device to alleviate hysteresis inspired consideration of Time Optimal Control (TOC) as another alternative to compensate hysteresis, as it too can be empirically designed and tuned independent of a precise model.

An explanation of the technical challenges, a summary of prior control strategies and a review of literature are contained in Chapter 2. Chapter 3 contains a more detailed explanation of hysteresis fundamentals, and how we creatively frame them as a disturbance rejection problem. In Chapter 4 the complete model for the piezo ceramic actuator is developed, only in order to facilitate the simulation and testing of the hysteresis compensation strategies, not as a component of those strategies. Simulation results will be presented in Chapter 5 for the ADRC and closed form discrete time optimal control of Han Jingqing, demonstrating their superiority to existing hysteresis compensation methods. The stability of the ADRC with ESO solution will be analyzed and shown for this hysteretic process in Chapter 6. Conclusions and future research possibilities in this dynamic field are discussed in Chapter 7.

CHAPTER 2

BACKGROUND AND LITERATURE REVIEW

The progress in controlling position at the nanometer scale has been sporadic since Binnig, Quate, and Gerber invented the AFM in 1986 [6]. They had first implemented simple Proportional plus Integral (PI) control, and this remains the choice in commercial systems today. The bandwidth for even a pure linear piezoceramic actuator would be limited by this choice, as shall be shown when the model is developed in Chapter 4. Qualitatively, a piezoceramic develops significant power for the mass, so inertia matching is a challenge from the start. The positive contribution from the direct energy to displacement conversion is balanced by an absence of viscous damping in a transmission, moving high frequency complex eigenvalues even closer to and farther along the imaginary axis. Exacerbating this is the elastic properties of the material, contributing harmonics of its natural resonant/anti-resonant pairs of eigenvalues, which, due to the nanometer scale displacements considered, can place the primary harmonic very near the force transmission eigenvalues, as we have simulated.

Santosh Devasia has studied this problem over a decade, and I quote from his paper [131].

"In general, the tracking performance of piezo-based positioning systems can be improved by using feedback control, for example, to reduce positioning errors due to creep and hysteresis. … However, a problem with using feedback-based approach is the low-gain margin, of piezo-based positioners, that limits the achievable improvements because high-gain feedback tends to destabilize piezo-based STM scanners. (The low gain margin is due to low structural damping in piezo-actuators that results in high-quality factor *Q*, i.e., a sharp-resonant peak accompanied by a rapid-phase drop in the frequency response.) In practice, a compromise is sought between performance and instability; feedback gains are adjusted to improve performance without instability. Thus, the tendency to become unstable at high gains (due to low-gain margins) has limited the success of typical feedback-based techniques to achieve high-speed positioning in STM applications."

We agree this is a valid comment for linear controls, sometimes even with hysteresis linearization, but is not necessarily true for nonlinear controls, as will be shown.

2.1 Nano-positioning Control: Stuck in a Model-Based Paradigm

The control details for commercial nanometer scale positioning tools are not shared, but what is known is that they use calibrated models of the actuator to compensate for their linear PI controls. Research in the past two decades has focused almost exclusively on improving these calibration models and continued use of standard linear PI [19,33,41,69,83], loop shaping [26,121] or H_∞ [16,53,107-114,121] control techniques. Some researchers modeling techniques have been straightforward linear frequency or time domain empirical models [83,108,121], while most have attempted to model the nonlinear hysteresis [16,19,22,23,34,41,53,57,63,82,96] and/or voltage creep [22,63,69,104,125]. A few have been unique [16,23,34,53,82,83], but most have adapted known hysteresis theory, which unfortunately has very few recognized experts [10,61,70,76,89-91,100-102,127]. Almost all these hysteresis models have been empirical models, by necessity, and only recently have a very few researchers chosen to explore anew the challenging fundamental principles underlying hysteresis [53].

Hysteresis compensation has generally followed 3 alternatives, all classical, and all critically dependent on a precise model of hysteresis. One alternative is feed forward compensation, a similar alternative is a classic “prefilter” configuration, and a third popular alternative is the application of an inverse of the hysteresis nonlinearity in series with the process.

Many researchers evaluate strain displacement of the piezo device without external load. A more valid example applies a force to an external load, which introduces 2 poles, usually very near the axis. Additionally, even those comparisons with an external load utilize a semilinear hysteresis model [10,76,127] relying on an “equivalent”, but nonexistent, hysteresis damping coefficient, b_{eq}. [14,62,87,124,129]

$$m\ddot{x}(t) + b_{eq}\dot{x}(t) + kx(t) = F(t) + P[x](t) \tag{2.1}$$

A more recent alternative model attributed to Della Torre [27] is quasilinear,

$$m\ddot{x}(t) + kv(t) = F(t), \;\; x(t) = (I+P)[v](t), \;\; v(t) = (I+P)^{-1}[x](t) \tag{2.2}$$

and we will explain our preference for this model in Chapter 3.

D. A. Hall [47] has recently presented an excellent overview of the state of the understanding for piezo ceramic actuators. Thermal nonlinearities are the most pronounced in piezo devices, whereas voltage “creep” and other elastic/plastic nonlinearities are less pronounced and better managed. These two nonlinearities, though significant, are very slow responding compared to the hysteresis nonlinearity of piezo devices. Thermal drift and voltage creep can be and usually are modeled and controlled as slowly time varying parameters in the motion equations.

2.1.1 Thermal Drift Models

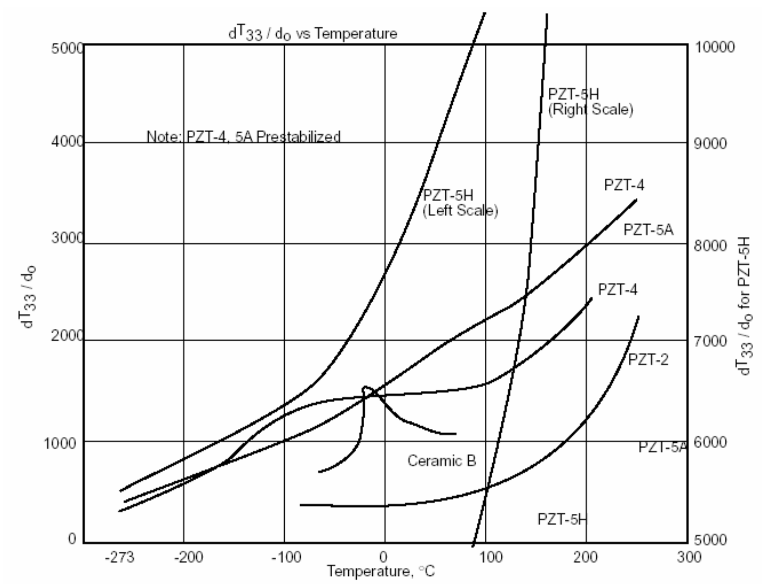

Figure 1 Variation of piezoelectric constant with temperature.

(Morgan Electro Ceramics, Inc. Bedford, Ohio, USA, Technical Publication TP-226 [5])

There has been minimal research done to date to address thermal drift within the nanometer control system [97,103], even though it is the most significant nonlinear factor affecting the performance accuracy, because its effect is very slow. Requicha [103] has reported, "*A typical value for drift velocity is 0.05 nm/s*." It is evident in Figure 1 the thermal drift of many piezo ceramic materials can be several percent over even small changes in temperature, and is extremely nonlinear, so a model-based solution is a questionable strategy. The preferred solution thus far has usually been to tightly manage the operating environment for both temperature and vibration, but we will demonstrate a better solution.

2.1.2 Voltage Creep Models

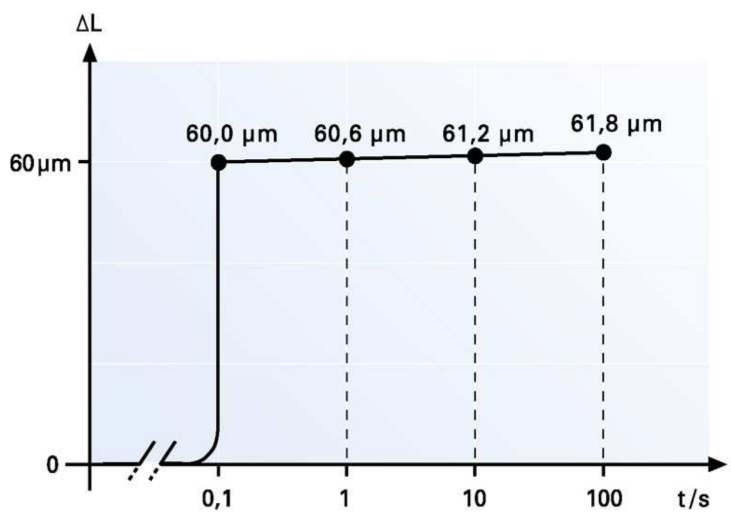

Figure 2 Piezo DC Input Creep (courtesy Physik Instrumente)

Application of a DC bias, such as the "engage" offset voltage, to a piezo tube scanner causes an initial and abrupt change in deflection, but the subsequent "creep" to a final position is slow. This slow change in position bias is additional to any localized oscillation in position due to the scanning. As with thermal drift, little research having been done to date [46,63,69,104].

S. Vieira did the earliest study of AFM creep at IBM research labs in 1986 [125], no doubt with the direction of Binnig, Quate and Gerber [6]. The mechanical strain, Δ*length/length*, changed 1-2% over a period of 200 seconds. Richter et al, in 2001 [104] had modeled and confirmed creep as a function of impressed voltage on the input to the mechanical subsystem, reinforcing Vieira's earlier experimental results. Again, our proposed solutions address voltage creep well.

2.1.3 Hysteresis Models

The earliest study of the hysteresis phenomenon began in the late 19th century in the area of elasto-plasticity and ferromagnetism. A few descriptions existed before the 20th century, as that of Duhem [30], but the most detailed analysis occurred early in the 20th century with Ludwig Prandtl [100,101] 1924 study of fluid flow, rediscovered by Ishlin'skii in 1944 [61]. Ferenc Preisach [102] 1935 research into ferromagnetism led to an alternative phenomenological description which is more general, and which we use in our simulated plant. Stephen Timoshenko [124] in 1928 refers to hysteresis dissipation in the first edition of his seminal work on harmonic elastic/plastic motion, wherein he diagrammed the hysteresis similar to Prandtl's "play" and "stop" operators, and even describes an "equivalent hysteretic damping constant" for calculating the dissipation attributed to the nonlinear motion. Cady [14] also describes in his book on piezoelectricity a “friction factor” with units of *mass/(distance*time)* and for the same purpose as Timoshenko, to account for the observed energy damping, for otherwise there is no component in the unforced linear equations to explain the observed dissipative behavior when the device is disturbed from equilibrium and released. Both Timoshenko and Cady resorted to a semilinear model description of the system utilizing the “equivalent hysteretic damping constant” to determine the dissipative force, $F_d = b_{eq}(x)\dot{x}$.

Fundamental research in closed loop control of piezo actuator position had some early and positive results reported by Tamer & Dahleh in 1994 [121], so the authors, triggering the bias to model-based control, recommended future research toward better modeling. Ge and Jouaneh in 1995 [41,42] suggested the phenomenological Preisach hysteresis model as a piezo compensator. Their techniques measured the first order reversal curves of a particular piezoceramic actuator, without any load, and used these data points within an algorithm to predict the hysteretic response of the particular device. Chen et al in 1999 [16], with a very precise stochastic model of their hysteretic device and a linear H∞ control, achieved 0.8% error. Other researchers [19,22,34,57,60,63,83,131], as did Chen, have tried alternatives to the Preisach model in both feed forward and feedback configurations, with less success. Mittal and Meng [96], in 2000, used an inverse Preisach operator within the closed loop of a nonlinear H∞ controller and achieved 0.3% error. These controls all followed the semilinear plant model.

Ku et al in 2000 [78] as well as Li and Tan in 2005 [82] proposed the use of neural networks to adapt their hysteresis model in real time. Their results were acceptable, but not exemplary, and slow. Neural network adaptive controllers might be feasible with much higher bandwidth processors.

2.2 The Active Disturbance Rejection Control Paradigm: New Thinking

Excellent controllers existed before the development and mathematical rigor of process models. The practical preference for Minorsky's [95] Proportional, Integral, Derivative (PID) controls and Ziegler-Nichols [130] associated empirical design methods attest to this. Models enable detailed mathematical design and analysis, and knowledge of them improve the design, but by definition the quality of model-based controls are directly correlated to the quality of the model, if one exists, as well as the quality of the output measurement. Control design in the absence of a model must be empirical, by necessity, and most often are based on minimizing an error to some desired response. The quality of error based designs is correlated to the quality of the measurement. Error based designs may also be analyzed as is a model-based design, using the same derived, and assumed valid, model. Most times these error based controls represent themselves quite well under analysis, or they may not, but seldom is the model challenged. The value of this analysis is no more or less than before, independent of the control choice.

In the presence of a perfectly accurate model and absence of any disturbance no feedback would be required, one could command a reference control signal and the desired position would result, $\ddot{x} = u$. This is not reality. The sources of error to the desired response may be varied, and under many names. Poorly modeled internal dynamics, whether in the model of the process or the realized controller hardware and software, is one common cause of error. External disturbances to the load are even more common, as are disturbances in measurement, and the list grows.

The disturbance paradigm is simplicity itself, all difference to the desired reference, whether internally or externally provoked, is considered a disturbance. The disturbance may be passively filtered, or it may be actively rejected. The design emphasis is on timeliness and accuracy of measurement and/or estimation of the disturbance, rather than on accuracy of a model. In many practical cases this is quite achievable, where modeling may not be.

Most often reality is a process output the sum of a control command *u* scaled by some factor *b* and perturbed by some general disturbance *f*, $\ddot{x} = f + bu$. The difference between the practical control command *u* and the desired control u_0 is:

$$u = \frac{u_0 - \hat{f}}{b} \tag{2.3}$$

such that the accuracy and timeliness of the estimate $\hat{f}$ determines the convergence of $\ddot{x} \approx u_0$.

Passive disturbance rejection via a closed form discrete optimal control solution is described by Gao in 2003 [37]. We will adapt this for our passive strategy. We will also follow his active disturbance rejection paradigm from 2006 [38]. In this effort we will treat hysteresis as a disturbance like any other, so in the next chapter we will develop this thesis.

CHAPTER 3

HYSTERESIS AS A DISTURBANCE: REFORMULATING THE PROBLEM

Our primary thesis is that hysteresis may be treated as any other disturbance in the context of compensating its effect in a control system. The hysteresis phenomena has been characterized by the leading authorities as a nonlinear transformation from a series of piecewise continuous monotonic inputs to similar series of outputs, possessing the rate independent memory and multi-output characteristics from experimental data. Unlike previous research which attempts to compensate for hysteresis through inversion of these complex models, we will account for hysteresis as a deviation from an otherwise linear input to output transformation.

It is well understood that it is not necessary to characterize external disturbances in order to compensate for them in control systems, and in fact systems are proven stable given unknown yet bounded disturbance. Our thesis is not different from this, full knowledge of the hysteresis character is not necessary for our purpose, given that it is bounded. It should be necessary to examine these complex models in order to best satisfy ourselves in this reformulation of the problem.

The understanding of hysteresis has been extensively enhanced recently through the work of mathematicians Krasnosel'skii & Pokrov'skii [70], Brokate & Sprekels [10], Visintin [127], Krejci [76] and Mayergoyz [91]. The majority of the development contained herein are based on Brokate & Sprekels [10] and Krejci [76], so their books are recommended. Mayergoyz' book [91] is more "engineer friendly" and so is recommended as a first primer for those interested in learning more. The other researchers are mostly mathematicians, and thus their work more abstract.

3.1 Hysteresis: A Qualitative Review of its Characteristics

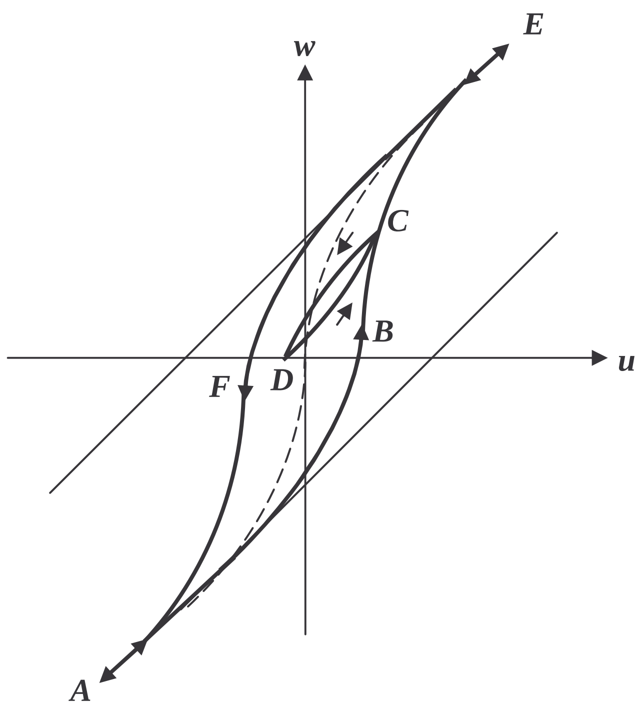

Figure 3 Hysteresis Input/Output Relationship

The Greek “*υστερεσυσ*” means “to lag in arrival”. This qualitatively describes what is observed, the output of some process is not synchronous with the change of input. The fundamental physics being observed is not always well understood for processes exhibiting hysteretic reaction, as is the case for our investigation, so an alternative mathematical device is required to describe the phenomena, a phenomenological description. A narrative is a much easier way to begin, before we investigate the mathematics.

Hysteresis, illustrated in Figure 3, is a process where a time dependent scalar valued variable u is transformed into time dependent multi-valued variables, w. We assume that if u increases from u_A to u_E, then the state (u,w) moves along the path ABCE, and if u decreases from u_E to u_A then state (u,w) moves along path EFA. The “major hysteresis loop” ABCEFA defines a closed region $\Theta \in \mathbb{R}^2$. Moreover, if u inverts its movement at u_C , or any other state $u_A < u < u_E$ along the boundary $\partial\Theta$, it moves into the interior of Θ and will describe a “minor hysteresis cycle” according to the hysteresis model. The limit of these minor cycles is the “*anhysteretic*” [127] curve. If $u < u_A$, *or* $u_E < u$ then the state (u,w) will move along the boundary as illustrated by the double ended direction arrows. At any instant t, including the initial instant, t_0, the value of $w(t)$ depends on the evolution of the state as well as the initial state. The hysteresis transform must be causal but the output $w(t)$ must not depend on $u|_{(t,T]}$.

$$w(t) = P[u, w_0, \lambda_0](t), \quad \forall t \in [t_0, T]. \tag{3.1}$$

A defining characteristic of most, but not all, hysteresis is *rate independent memory*, the output depends on the input value and its history regardless of rate of change. It transforms the input to one of infinitely many possible values, dependent on its history, thus most common nonlinear analysis techniques are not applicable. The Preisach operator used for our simulation is a *phenomenological* model, it is a mathematic device to describe the transform and it is not based in physics first principles.

Hysteresis is associated with energy dissipation, which is proportional to the area enclosed by the hysteresis cycle described by the operator (whether minor or major). Rate independent hysteresis dissipation, a function of strain, and rate dependent "viscous" dissipation, a function of strain "velocity", usually exist simultaneously, with the latter vanishing as the rate tends to zero, while the former is more dominant at slower speeds. Accounting for this dissipation, or disregarding it, will prove a differentiating factor in our preferred choice of hysteresis model.

3.2 Hysteresis Transforms: An Infinite Series of Basis Functions

Most hysteresis transformations are constructed as an infinite series sum or integral using a basis function, and then taken to the limit as the quantity or time approaches infinity. The quality of the transform is then contingent on the quantity or time interval used. (One could speculate a wavelet would be a better basis function candidate, but that is a thesis for another dissertation.)

The scalar Preisach model uses a fundamental relay with delay operator as a basis function and the output is a weighted sum/integral of the constituent basis. The practical constraint on this model is that the weight function(s) must be empirically determined in each instance and accuracy is dependent on the dimension of the weight vector. The advantage is the fidelity to actual results, compared to other models (again dependent on the weight vector dimension), and the simplicity of implementation as linear algebraic equations in real time. This is consistent with the application of model-based controls. A Preisach operator, per Brokate & Sprekels [10], Visintin [127] and Krejci [76], will be used for our simulation. It is globally Lipschitz and invertible, as is its derivative, and results in continuous piecewise monotonic output for comparable input.

Definition: The Preisach memory curve:

$$\begin{aligned}&\Lambda := \left\{ \varphi \middle| \varphi : \mathbb{R}_+ \to \mathbb{R}, \left|\varphi(r) - \varphi(\bar{r})\right| \le \left|r - \bar{r}\right| \ \mathit{for\ all}\ r, \bar{r} \ge 0, R_{supp}(\varphi) < +\infty \right\} \\ &R_{supp}(\varphi) := \sup\left\{ r \middle| r \ge 0, \varphi(r) \ne 0 \right\}\end{aligned} \tag{3.2}$$

where R_{supp} represents the saturation value for the hysteresis. Examples of elements of this set, $\lambda_t(t_1, r) \in \Lambda$ and $\lambda^0 = \lambda_t(t_0, r) \in \Lambda$ are shown in Figure 6.

The "relay" operator $R_{\rho 1,\rho 2}[\lambda^0,u](t) = R_{s-r,s+r}[\lambda^0,u](t) = w(t)$ is shown in Figure 4. The "stop" and "play" operators are shown in Figure 5.

The "play" operator may be defined inductively, referring to Figure 5, as:

$$\begin{aligned}&F_r[\lambda^0, u](t) = w(t), \\ &w(0) = f_r(u(0), 0), \\ &w(t) = f_r(u(t), w(t_i)), \ \mathit{for}\ t_i < t \le t_{i+1},\ 0 \le i \le N-1, \\ &\mathit{where}\ u(t)\ \mathit{is\ monotone\ in}\ N\ \mathit{subintervals\ of}\ [0,T], \\ &f_r(u,w) = \max\left\{u - r, \min\left\{u + r, w\right\}\right\}, r \ge 0.\end{aligned} \tag{3.3a}$$

The "stop" operator may be defined inductively, referring to Figure 5, as:

$$
\begin{aligned}
&E_r[\lambda^0, u](t) = w(t), \\
&w(0) = e_r(u(0)), \\
&w(t) = e_r(u(t) - u(t_i) + w(t_i)),\ \mathit{for}\ t_i < t \le t_{i+1},\ 0 \le i \le N-1, \\
&\mathit{where}\ u(t)\ \mathit{is\ monotone\ in}\ N\ \mathit{subintervals\ of}\ [0,T], \\
&e_r(u) = \min\left\{r, \max\left\{-r, u\right\}\right\}, r \ge 0
\end{aligned}
\tag{3.3b}
$$

The single dimension "play" operator is an instance of the two dimension "relay" operator, as it can be expressed as a superposition of relay elements:

$$
F_r[\lambda^0, u](t) = \frac{1}{2}\int_{-\infty}^{\infty} R_{s-r,s+r}[\lambda^0, u](t)ds \tag{3.3c}
$$

where $R_{s-r,s+r}[\lambda^0,u](t) = +1$ *for* $s < 0$ *and* -1 *for* $s \ge 0$.

The "play" and "stop" operator are related by the identity operator:

$$
F_r + E_r = I_d \quad \text{such that} \quad F_r[\lambda^0, u](t) + E_r[\lambda^0, u](t) = u(t) \tag{3.3d}
$$

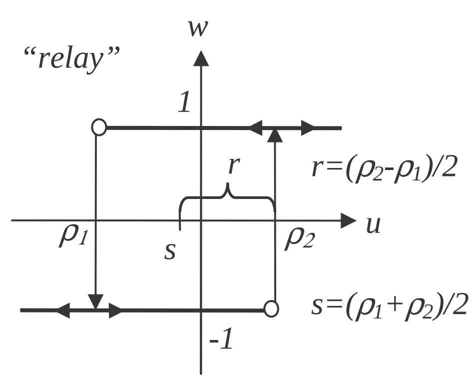

Figure 4 The "Relay" Operator

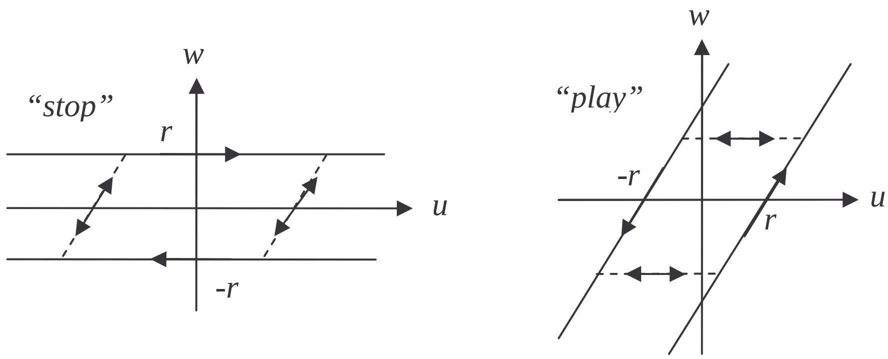

Figure 5 “Stop” and “Play” Operators

NOTE: In the interest of brevity one may here forward drop the understood dependence of hysteresis operators on the initial memory curve λ^0.

A Preisach operator then transforms a continuous piecewise monotonic input function *u(t)* into another continuous piecewise monotonic output *w(t)* as:

$$P[u](t) = w(t) = \int_0^{\infty}\int_{-\infty}^{\infty} \mu(r,s) R_{s-r,s+r}[u](t)dsdr \tag{3.4}$$

Where $\mu(r,s)$ is a nonnegative weighting function assumed to vanish for large values of *r* and *s*. The Prandtl-Ishlinskii operator can be expressed in terms of the “stop” and “relay” operators as:

$$\begin{aligned} PI[u](t) = w(t) &= \int_0^{\infty}\int_{-\infty}^{\infty} \rho(r) E_r[u](t)dr \\ &= \int_0^{\infty}\int_{-\infty}^{\infty} -\frac{\rho(r)}{2} R_{s-r.s+r}[u](t)dsdr + u(t)\int_0^{\infty} \rho(r)dr \end{aligned} \tag{3.5}$$

where $\rho(r)$ is a calculated weighting function different from, but similar to, $\mu(r,s)$.

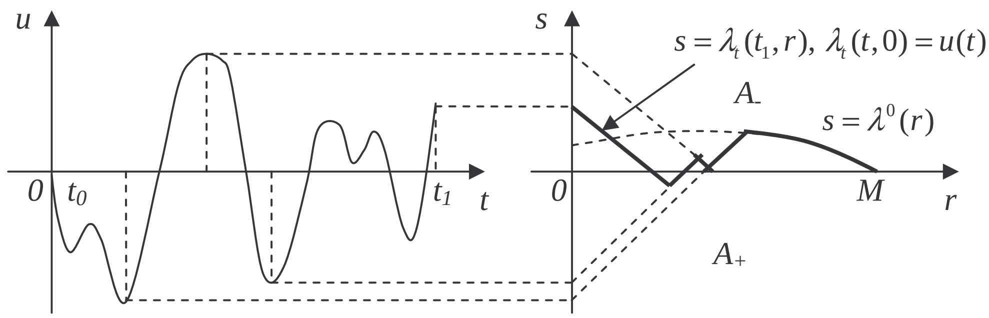

Figure 6 The Preisach Operator memory curve $s=\lambda_t(t,r)$

For input *u(t)* a piecewise continuous monotonic function, and $\lambda^0 \in \Lambda$ the memory curve at time t_0 recording all past history of local minimum and local maximum values for $u(t_{0-})$ in the Preisach plane is shown in Figure 6. *"M"* is the maximum past value of *r,s* which is usually, but not always, the saturation value, R_{supp}. The bold line demarks the boundary $\lambda_t(t_1,r)$ which separates the two sets:

$$A_{\pm}=\left\{(r,s)\in \mathbb{R}_+\times\mathbb{R}\,\middle|\,R_{s-r,s+r}[\lambda^0,u](t)=\pm 1\right\},\ A_+=+1 \textit{ and } A_-=-1 \tag{3.6}$$

So that:

$$P[u](t)=w(t)=\iint_{A_+(t)}\mu(r,s)dsdr-\iint_{A_-(t)}\mu(r,s)dsdr \tag{3.7}$$

and if one can determine the boundary function $\lambda_t(t,r) = \partial A_+(t) \cap \partial A_-(t)$, where $\lambda_t(t_0,r) = \lambda^0$, then one can determine *w(t).* By the definition of the "play" operator one has the identity:

$$\lambda_t(t,r)=F_r[u](t) \tag{3.8}$$

(This defines the method for most digital estimation algorithms, whereby a set of discrete weights $\mu(r,s)$ for the right half plane, determined from measured data of the hysteretic device first order reversal curves, can be interpolated over the areas A_+ and A_- determined by the function $\lambda_t(t,r)$ and then summed for the value $w(t)$.)

The Preisach operator can also be expressed in terms of the "play" operator:

$$P[u](t) = \int_0^\infty q\left(r, F_r[u](t)\right)dr + w_{00} \tag{3.9a}$$

where:

$$\begin{aligned} q(r,s) &= 2\int_0^s \mu(r,\xi)d\xi, \\ w_{00} &= \int_0^\infty \int_{-\infty}^0 \mu(r,s)dsdr - \int_0^\infty \int_0^\infty \mu(r,s)dsdr \end{aligned} \tag{3.9b}$$

and if the hysteresis is symmetric:

$$w_{00} = 0 \textit{ if } \ \mu(r,s) = \mu(r,-s) \ \textit{ for all r and s} \tag{3.9c}$$

This becomes very important as one determines the energy equations for the stress/strain relationships of the piezoceramic.

3.3 Hysteresis Represents Dissipated Energy

Hysteresis is a manifestation of the energy dissipated in the device. The area prescribed by a hysteresis cycle is proportional to the energy dissipated during that cycle. This relationship has been extensively studied only the past decade, predominately by Brokate & Sprekels [10,11] and Krejci [71,76,77], and it is a critical dimension connecting hysteresis transformations and physical reality. This relation explains the convergence of the phenomena toward the anhysteretic response, and why techniques such as dithering are effective. These energy relations are not incorporated in the hysteresis transforms, the appropriate incorporation of hysteresis transforms in the system force equations are crucial to proper accounting for the energy dissipation, and were first posed by Della Torre [27]. This proper accounting for energy allows one to reframe hysteresis as a disturbance, because it represents energy dissipation, it is not simply a mathematic transformation.

The potential energy operator, associated with the Preisach operator, using the “play” operator as basis, is:

$$U[u](t) = \int_0^\infty Q\left(r, F_r[u](t)\right) dr \tag{3.10}$$

where:

$$Q(r,s) = 2\int_0^s \xi\mu(r,\xi)d\xi \tag{3.11}$$

and the dissipation operator is:

$$D[u](t) = \int_0^\infty r\, q\left(r, F_r[u](t)\right) dr \tag{3.12}$$

and again:

$$q(r,s) = 2\int_0^s \mu(r,\xi)d\xi \tag{3.13}$$

where the following identity holds:

$$\dot{w}(t)u(t) = \frac{d}{dt}U[u](t) + \left|\frac{d}{dt}D[u](t)\right| \tag{3.14}$$

This is the energy dissipation justification for the quasilinear form of the mechanical force equation of the piezo actuator.

3.4 The Dynamic of Hysteresis: semilinear versus quasilinear

The contribution of hysteretic energy dissipation does not manifest itself in the commonly applied semilinear series configuration for the mechanical subsystem in Figure 7. Hysteretic dissipation can only be incorporated as part of an “equivalent hysteretic damping coefficient”, b_{eq}, in this series connection, in which case it acts as a rate dependent viscous damping, rather than as a rate independent dissipation. This does not match the observed behavior of hysteresis dissipation at slow rates.

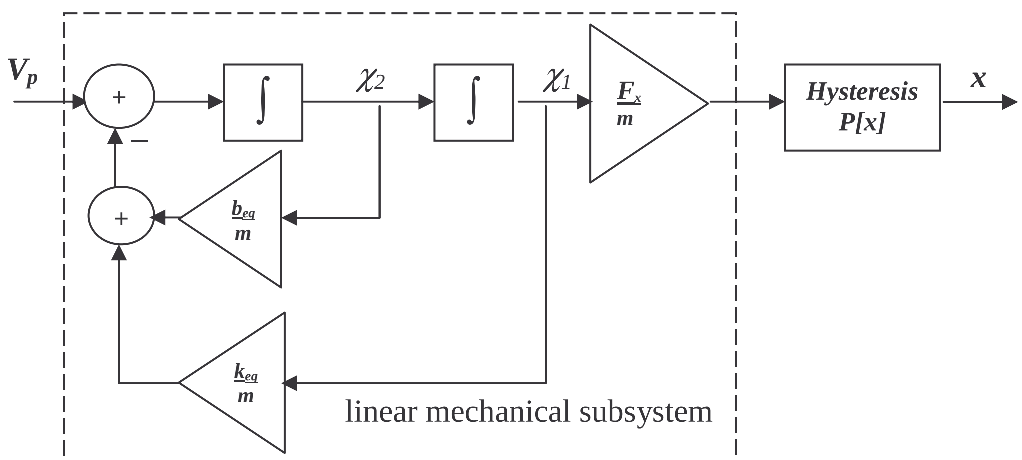

Figure 7 The semilinear mechanical subsystem diagram.

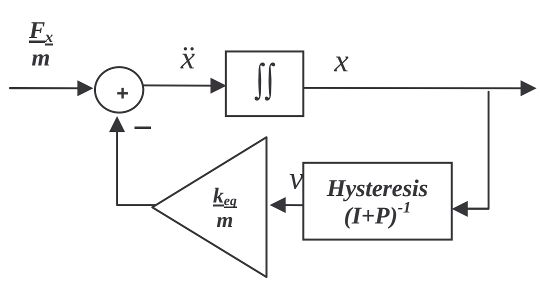

Figure 8 The quasilinear mechanical subsystem diagram.

The mechanical system model in Figure 8 has much to recommend it for matching observation and the saturation effects, as well as simulation in regards dissipation. This modified “moving model” may trace its origin to Della Torre [27] research in magnetic media. The model incorporates the inverse of the hysteresis operator [10,76,127] in the elastic feedback of the device, thus its dissipation contribution is rate independent, as observed, and not dependent on an “equivalent hysteresis damping” coefficient *(b_{eq}=0, there is no separate viscous damping in our system).* Additionally, extending the simple saturated operator *P[u]* in Figure 9 to *I+P[u]* as shown in Figure 10 and Figure 11 as proposed by Krejci [76,77] has addressed the saturation limit and provided a hysteresis model which more realistically represents observed behavior, even if used simply as a series inverse.

This system is quasilinear, incorporating the Preisach hysteresis operator and its derivative [10,71,73,76,77,126,127].

$$\begin{aligned}&\ddot{x}(t)+v(t)=F_x(t),\ \ x(t)=v(t)+P[v](t),\ \ v(t)=(I+P)^{-1}[x](t),\\&x\in C^2,\ v\in C^0,\ F_x\in L^\infty(0,\infty),\ t\geq 0\end{aligned}\tag{3.15}$$

and the Preisach operators, inverse operators and their derivatives are Lipschitz [10,11,28,29,76,127] under the assumption of continuous piecewise monotonic inputs:

$$\begin{aligned}&\left|P[u]-P[w]\right|\leq\left\|u-w\right\|_{[0,t]}\\&\textit{and}\ \left|(I+P)^{-1}[u]-(I+P)^{-1}[w]\right|\leq\left\|u-w\right\|_{[0,t]}\ \ u,w\in C^0,\ t\geq 0\end{aligned}\tag{3.16}$$

$$\begin{aligned}&\ddot{x}(t)=\frac{F_x(t)}{m}-\frac{k_{eq}}{m}v(t)\\&=\frac{F_x(t)}{m}-\frac{k_{eq}}{m}(I+P)^{-1}[x](t)\end{aligned}\tag{3.17}$$

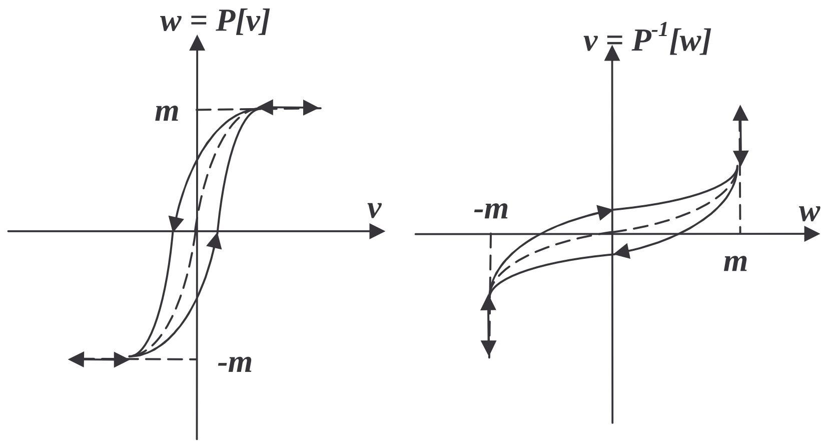

Figure 9 Simple Hysteresis Operator and Inverse

(Note the operator's counterclockwise, CCW, and the inverse clockwise, CW, evolution, as well as the major loop region and the "anhysteretic" collapsed curve.)

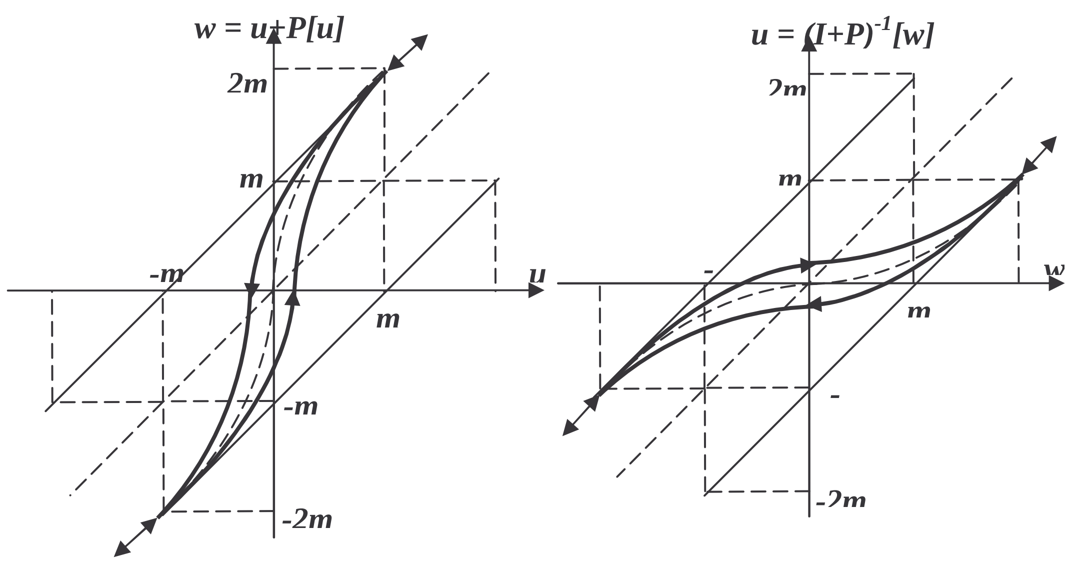

Figure 10 Extended Hysteresis Model and inverse

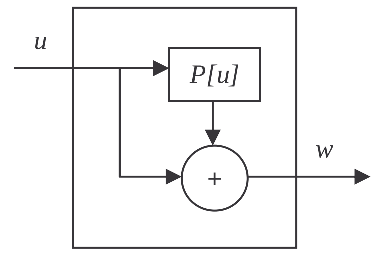

Figure 11 Extended Hysteresis model block diagram representation.

3.5 Hysteresis as a Disturbance: the Problem Reformulated

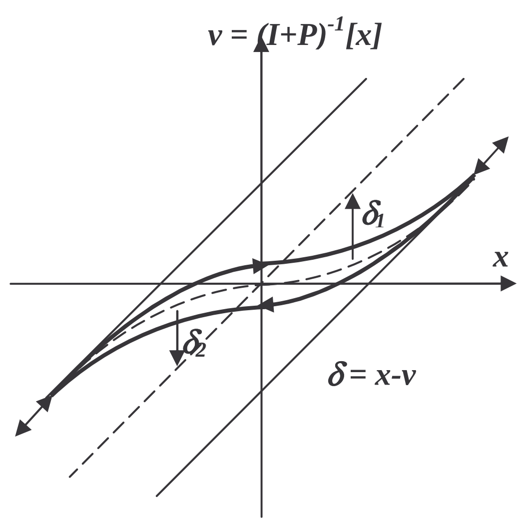

Figure 12 Inverse Hysteresis Function as a Disturbance from the Linear Response.

Let us consider for now only the nonlinearity attributed to hysteresis and assume a simplified model encompassing only the hysteretic mechanical subsystem. Regard then the hysteresis response curve Figure 12 and the quasilinear mechanical model Figure 8. The difference for the linear relationship between output x_1 and the state v_1, is $\delta_1 > 0$, and the same for x_2, v_2 and $\delta_2<0$, where $(x,v)\in\Theta\subset\mathbb{R}^2$ are members of the major hysteresis loop region. These values are absolutely bounded by the maximum value of saturation for the device major loop, and become smaller as the device approaches the anhysteretic response due to the "accommodation" [91] process. One can then write the equation:

$$\ddot{x}=-\alpha v+bu=-\alpha\left(x-\delta\right)+bu, \\ where: u=V_{in},\ b=\frac{K_{vf}^{0}}{m}>0,\ and\ \alpha=\frac{k_{eq}}{m}>0 \tag{3.18}$$

and δ is the nonlinear component in position.

This reduces the characterization of hysteresis to that necessary to compensate for it in a control context. Granted this definition does not enable one to predict the expected value of the output at some future time given an input profile, a valid use for a complex model, but it serves our purpose to compensate the nonlinear position quite elegantly.

The Active Disturbance Rejection Control paradigm [38] treats these nonlinearities no different than any unknown disturbance, estimating them and canceling their effect in real time in order to render the system as an apparent double integrator to the control force, $\ddot{x}\approx u_0$. The passive disturbance rejection paradigm implements Han's closed form discrete control [37,49], which applies minimal time optimal control to reach the disturbance equilibrium, $\delta = 0$. This is quite similar to and inspired by the "dithering" historically and effectively applied to hysteretic processes to drive them to their anhysteretic, minimum energy response, except that Han's control is not necessary to be maximum cycling "bang-bang" control.

CHAPTER 4

SIMULATION DEVELOPMENT

Experimental equipment to verify the performance of position controls at the nanometer scale is expensive to acquire and difficult to maintain. These are not available at Cleveland State University at the time of this writing. In their absence we have resorted to developing a simulation of the piezoceramic actuator similar to that process followed by earlier researchers. In fact, we have relied on the kindness of other researchers to share their hysteresis model data in order to assemble this simulation [23,80,82], and we are very grateful to them. We will succinctly review the simulation development, and those desiring details of the dynamics may consult the references. The simulation will adhere to the quasilinear mechanical model and utilize an inverse hysteresis operator simulation written as a Matlab m-file in C code. The code is in Appendix A: Hysteresis Simulation m-files.

4.1 The Linear Subsystem

The simulation system will be composed of a linear portion representing the piezo ceramic coupled stress/strain relationships, which result in the hyperbolic wave equations with multiple harmonics. We simulate this as the IEEE standard piezo ceramic model, a linear electrical equivalent. In series with and following the linear electrical equivalent harmonic subsystem will be the quasilinear mechanical subsystem incorporating the hysteresis operator. We will first establish the linear version of the mechanical subsystem for comparison, using the equivalent friction, b_{eq}, and spring, k_{eq}, coefficients as calculated using the stress/strain parameters.

4.1.1 Piezo Elastic Stress and Strain Simulation

The following model descriptions are based on "Piezoelectricity" by Walter G. Cady [14], "Piezoelectric Ceramics" by B. Jaffe, W. R. Cook and H. L. Jaffe [62] and "An Introduction to the Theory of Piezoelectricity" by Jiashi Yang [129]. The monolithic piezoceramic tube actuator is physically represented in Figure 13. The x axis is the tube axis, with tube length = l_x, radius r, and thickness h. The power source for the piezo tube actuator is the piezo voltage V_p impressed across the thickness of the tube.

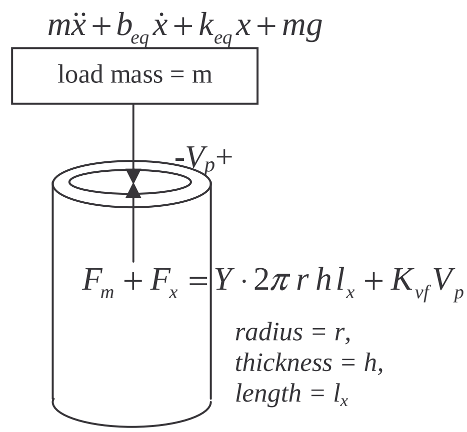

Figure 13 Monolithic Piezo Tube Actuator

Stress is a tensor force of extension, compression or shear as shown in Figure 14 with the definitions:

$$X_x = compression/extension\ stress\ along\ x\ axis$$
$$Y_y = compression/extension\ stress\ along\ y\ axis$$
$$Z_z = compression/extension\ stress\ along\ z\ axis$$
$$Y_z = shear\ stress\ parallel\ to\ y\ axis\ in\ plane\ normal\ to\ z\ axis$$
$$Z_x = shear\ stress\ parallel\ to\ z\ axis\ in\ plane\ normal\ to\ x\ axis$$
$$X_y = shear\ stress\ parallel\ to\ x\ axis\ in\ plane\ normal\ to\ y\ axis$$

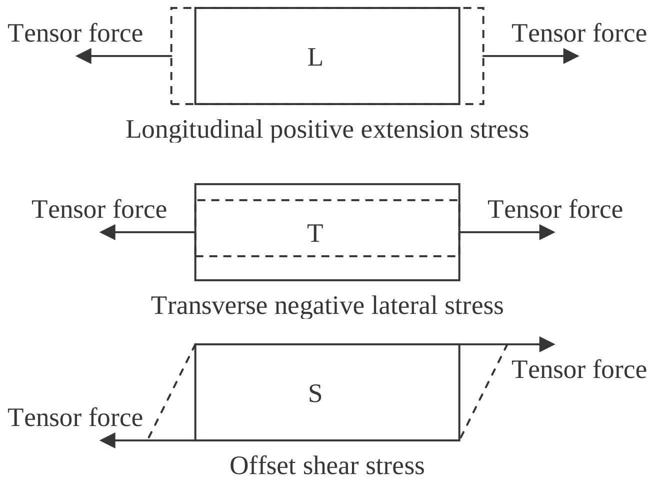

Figure 14 Elastic stress tensors

The axes used are shown in Figure 15.

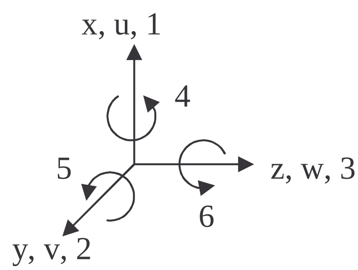

Figure 15 Axes definitions for piezo equations.

The variable "*u*" is an incremental displacement along x-axis in Figure 15, as is "*v*" to y-axis and "*w*" to z-axis. 1, 2 and 3 are alternative names for x, y and z linear vectors. 4, 5 and 6 are rotations about the x, y and z-axis respectively. Polarization is along z axis.

Strain is the deformation displacement along an axis caused by these stresses and defined by the equations:

$$
\begin{aligned}
&x_x = \frac{\partial u}{\partial x} \; and \; y_y = \frac{\partial v}{\partial y} \; and \; z_z = \frac{\partial w}{\partial z} \\
&y_z = \frac{\partial w}{\partial y} + \frac{\partial v}{\partial z} \; and \; z_x = \frac{\partial u}{\partial z} + \frac{\partial w}{\partial x} \; and \; x_y = \frac{\partial v}{\partial x} + \frac{\partial u}{\partial y}
\end{aligned}
\tag{4.1}
$$

The general relationships between stress and strain for all piezoelectric crystals are the elastic compliance ‘s’ and elastic stiffness ‘c’ matrices:

$$
\begin{bmatrix} x_x \\ y_y \\ z_z \\ y_z \\ z_x \\ x_y \end{bmatrix} = \begin{bmatrix} s_{11} & . & . & . & . & s_{16} \\ . & & & & & . \\ . & & & & & . \\ . & & & & & . \\ . & & & & & . \\ s_{61} & . & . & . & . & s_{66} \end{bmatrix} \begin{bmatrix} X_x \\ Y_y \\ Z_z \\ Y_z \\ Z_x \\ X_y \end{bmatrix} \tag{4.2}
$$

$$
\begin{bmatrix} X_x \\ Y_y \\ Z_z \\ Y_z \\ Z_x \\ X_y \end{bmatrix} = \begin{bmatrix} c_{11} & . & . & . & . & c_{16} \\ . & & & & & . \\ . & & & & & . \\ . & & & & & . \\ . & & & & & . \\ c_{61} & . & . & . & . & c_{66} \end{bmatrix} \begin{bmatrix} x_x \\ y_y \\ z_z \\ y_z \\ z_x \\ x_y \end{bmatrix} \tag{4.3}
$$

Fortunately, for Lead Zirconate Titanate (PZT) ceramics, the crystal structure is such that many elements of the matrices are zero value or duplicates of other values. This greatly simplifies, but does not eliminate, the mechanical coupling between axes.

$$\begin{bmatrix} x_x \\ y_y \\ z_z \\ y_z \\ z_x \\ x_y \end{bmatrix} = \begin{bmatrix} s_{11} & s_{12} & s_{13} & 0 & 0 & 0 \\ s_{12} & s_{11} & s_{13} & 0 & 0 & 0 \\ s_{13} & s_{13} & s_{33} & 0 & 0 & 0 \\ 0 & 0 & 0 & s_{44} & 0 & 0 \\ 0 & 0 & 0 & 0 & s_{44} & 0 \\ 0 & 0 & 0 & 0 & 0. & s_{66} \end{bmatrix} \begin{bmatrix} X_x \\ Y_y \\ Z_z \\ Y_z \\ Z_x \\ X_y \end{bmatrix} \tag{4.4}$$

$$\begin{bmatrix} X_x \\ Y_y \\ Z_z \\ Y_z \\ Z_x \\ X_y \end{bmatrix} = \begin{bmatrix} c_{11} & c_{12} & c_{13} & 0 & 0 & 0 \\ c_{12} & c_{11} & c_{13} & 0 & 0 & 0 \\ c_{13} & c_{13} & c_{33} & 0 & 0 & 0 \\ 0 & 0 & 0 & c_{44} & 0 & 0 \\ 0 & 0 & 0 & 0 & c_{44} & 0 \\ 0 & 0 & 0 & 0 & 0. & c_{66} \end{bmatrix} \begin{bmatrix} x_x \\ y_y \\ z_z \\ y_z \\ z_x \\ x_y \end{bmatrix} \tag{4.5}$$

There are also piezoelectric relationships between the electric fields and voltages along axes and the stress and strain. We will define only those needed for our purposes.

$$\begin{bmatrix} x_x \\ y_y \\ z_z \\ y_z \\ z_x \\ x_y \end{bmatrix} = \begin{bmatrix} \partial u / \partial x \\ \partial v / \partial y \\ \partial w / \partial z \\ \partial w / \partial y + \partial v / \partial z \\ \partial u / \partial z + \partial w / \partial x \\ \partial v / \partial x + \partial u / \partial y \end{bmatrix} = \begin{bmatrix} 0 & 0 & d_{31} \\ 0 & 0 & d_{31} \\ 0 & 0 & d_{33} \\ 0 & d_{15} & 0 \\ d_{15} & 0 & 0 \\ 0 & 0 & 0 \end{bmatrix} \cdot \begin{bmatrix} E_x \\ E_y \\ E_z \end{bmatrix} \tag{4.6}$$

$$\begin{bmatrix} x_x \\ y_y \\ z_z \\ y_z \\ z_x \\ x_y \end{bmatrix} = \begin{bmatrix} 0 & 0 & d_{31} \\ 0 & 0 & d_{31} \\ 0 & 0 & d_{33} \\ 0 & d_{15} & 0 \\ d_{15} & 0 & 0 \\ 0 & 0 & 0 \end{bmatrix} \cdot \begin{bmatrix} \partial V_x / \partial x \\ \partial V_y / \partial y \\ \partial V_z / \partial z \end{bmatrix} \tag{4.7}$$

The scalars d_{15} , d_{31} and d_{33} are piezoelectric strain coefficients.

The x-axial strain can be expressed as:

$$\begin{aligned}&\frac{\partial u}{\partial x}=d_{31}\frac{\partial V_z}{\partial z}\Rightarrow\frac{\partial u}{\partial x}dz=d_{31}\frac{\partial V_z}{\partial z}dz\\&\Rightarrow\int_0^h\frac{\partial u}{\partial x}dz=d_{31}\int_0^{Vp}\partial V_z\\&\Rightarrow\frac{\partial u}{\partial x}=\frac{d_{31}}{h}V_p\end{aligned}\tag{4.9}$$

and:

$$\begin{aligned}&\frac{\partial u}{\partial x}=\frac{d_{31}}{h}V_p\Rightarrow\frac{\partial u}{\partial x}dx=\frac{d_{31}}{h}V_p dx\Rightarrow\int_0^{\Delta x}\partial u=\frac{d_{31}}{h}V_p\int_0^{lx}dx\\&\Rightarrow\Delta x=\frac{d_{31}l_x}{h}V_p\Rightarrow V_p=\frac{h}{d_{31}l_x}\Delta x\end{aligned}\tag{4.10}$$

The x-axial stress (where c_{11}, c_{12}, c_{13}, are “elastic stiffness coefficients”, d_{31}, d_{33}, are are piezoelectric strain coefficients) is expressed as:

$$\begin{aligned}&X_x=c_{11}\frac{\partial u}{\partial x}+c_{12}\frac{\partial v}{\partial y}+c_{13}\frac{\partial w}{\partial z}\\&=c_{11}d_{31}E_z+c_{12}d_{31}E_z+c_{13}d_{33}E_z\\&=(c_{11}d_{31}+c_{12}d_{31}+c_{13}d_{33})\frac{\partial V_z}{\partial z}\end{aligned}\tag{4.11}$$

$$\begin{aligned}&X_x dz=(c_{11}d_{31}+c_{12}d_{31}+c_{13}d_{33})\frac{\partial V_z}{\partial z}dz\\&\Rightarrow\int_0^h X_x dz=(c_{11}d_{31}+c_{12}d_{31}+c_{13}d_{33})\int_0^{Vp}\partial V_z\\&\Rightarrow X_x=\frac{(c_{11}d_{31}+c_{12}d_{31}+c_{13}d_{33})}{h}V_p\end{aligned}\tag{4.12}$$

The x-axial force is the integral of stress across the normal surface area, which determines the voltage to force gain, dF_x/dV :

$$\begin{aligned}
F_x &= AX_x = 2\pi rhX_x \\
&= 2\pi r(c_{11}d_{31} + c_{12}d_{31} + c_{13}d_{33})V_p \\
&= \frac{dF_x}{dV}V_p \\
&= K_{vf}V_p \\
&\Rightarrow K_{vf} = 2\pi r(c_{11}d_{31} + c_{12}d_{31} + c_{13}d_{33})
\end{aligned} \tag{4.13}$$

consequently one determines the "piezoelectric spring constant", k_{eq} :

$$\begin{aligned}
F_x &= 2\pi r(c_{11}d_{31} + c_{12}d_{31} + c_{13}d_{33})V_p \\
&= \frac{2\pi rh}{d_{31}l_x}(c_{11}d_{31} + c_{12}d_{31} + c_{13}d_{33})\Delta x \\
&= k_{eq}\Delta x \\
&\Rightarrow k_{eq} = \frac{2\pi rh}{d_{31}l_x}(c_{11}d_{31} + c_{12}d_{31} + c_{13}d_{33})
\end{aligned} \tag{4.14}$$

The equivalent viscous damping coefficient is given as a function of the driving force frequency ω, the wave velocity, c, the resultant wavelength, λ, the damping factor, Q, the material density ρ, and Young's elastic modulus Y:

$$b_{eq} = \frac{\rho c\lambda}{2\pi Q} = \frac{\rho\sqrt{\frac{Y}{\rho}}\frac{2\pi c}{\omega}}{2\pi Q} = \frac{Y}{Q\omega} \tag{4.15}$$

(Remark: the measurement units for b_{eq}, *[Kg/(m*sec)]*, are a function of strain, related to driving force amplitude *[m]* and so are different than for simple bulk viscous damping, which is *[Kg/sec]*, and is not a constant) so that one now has a dynamic system motion equation with a load:

$$m\ddot{x} + b_{eq}\dot{x} + k_{eq}x = F_x = K_{vf}V_p \tag{4.16}$$

and the static equilibrium of gravity and elastic spring:

$$F_m = Y \cdot 2\pi\, r\, h\, l_x = mg \tag{4.17}$$

and the state equation in controllable canonical form is:

$$\begin{aligned} \dot{\chi} &= \begin{bmatrix} 0 & 1 \\ -k_{eq}/m & -b_{eq}/m \end{bmatrix}\chi + \begin{bmatrix} 0 \\ 1 \end{bmatrix} V_p \\ x &= \begin{bmatrix} K_{vf}/m & 0 \end{bmatrix}\chi, \quad \chi_1 = (m/K_{vf})x,\ \chi_2 = \dot{\chi}_1 \end{aligned} \tag{4.18}$$

and as $k_{eq}/m > 0$ and $b_{eq}/m > 0$ this A matrix is Hurwitz and the linear mechanical subsystem is BIBO stable.

Typical piezo tube dimensions from Morgan ElectroCeramics™ [5], capable of nanometer scale accuracy positioning, would be l_x = 25 mm, *OD* = 25mm, *ID* = 19mm, Y = 65x10^9 N/m^2 and ρ = 7.75x10^3 kg/m^3. The A matrix eigenvalues of the mechanical subsystem for the piezo tube used in simulation are:

-3.975e-5 +1.333e+5i and *-3.975e-5 -1.333e+5i*.

These eigenvalues illustrate the extremely low dissipation, even when using "equivalent hysteresis damping", and the high elasticity of the material. The qualitative comments from many authors regarding their experimental results confirm these results.

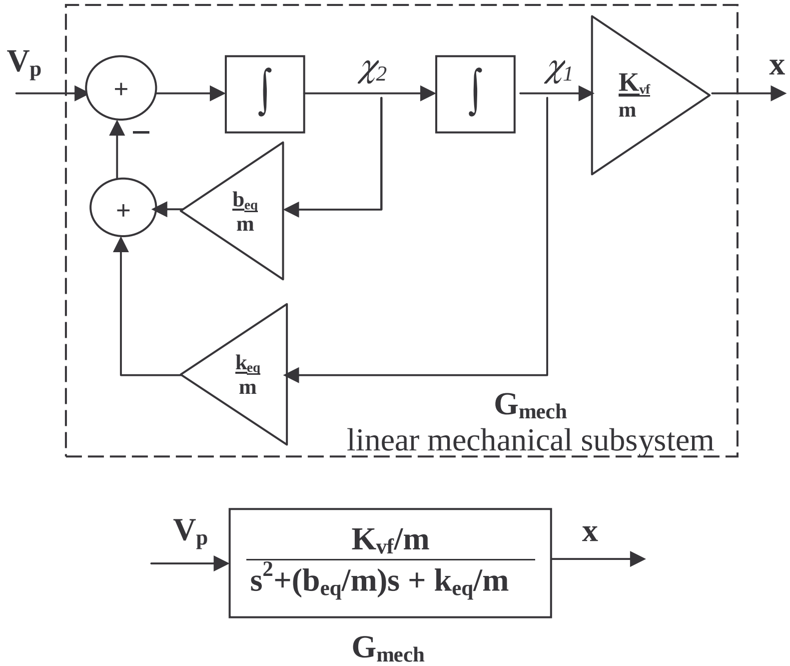

Figure 16 The Piezo actuator linear mechanical subsystem.

4.1.2 Piezo Harmonic Electric Simulation

The presently accepted electrical model for piezo devices, shown in Figure 17, IEEE Std.176-1987, is derived from W.G. Cady's original work. Cady addressed the issues of dynamics at resonance by referencing Young's analytic work in elastics and then defining an equivalent electric model for the combined unforced and unloaded piezo electric/elastic/plastic displacement equations.

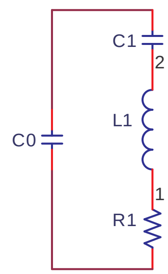

Figure 17 IEEE Std.176-1987

The more detailed electrical model in Figure 18 shows the relation from the physical power source voltage V_{in} through a source impedence R_0 to the impressed piezo voltage V_p, which will exhibit multiple harmonics.

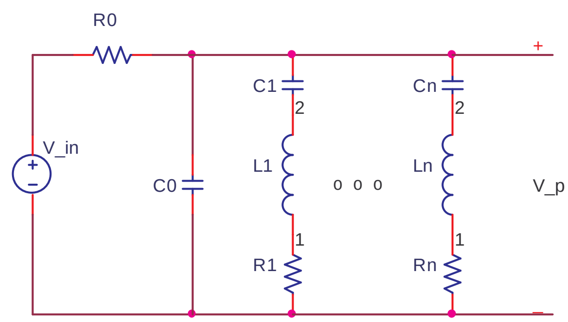

Figure 18 Piezo electrical subsystem schematic.

$$I_p = \frac{V_{in} - V_p}{R_0} = I_0 + I_1 + \ldots + I_n \tag{4.19}$$

Complex Impedance for each parallel path:

$$z_0 = \frac{1}{C_0 s} \quad \text{and} \quad z_n = \frac{(L_n C_n s^2 + R_n C_n s + 1)}{C_n s} \tag{4.20}$$

Implies:

$$V_{in} = V_p R_0 \left(\frac{1}{z_0} + \frac{1}{z_1} + \ldots \frac{1}{z_n} \right) + V_p \tag{4.21}$$

The "n" harmonics are determined by the bar/tube physical dimensions and natural frequencies of mechanical oscillations and exhibit themselves as harmonics of the impressed voltage V_p.

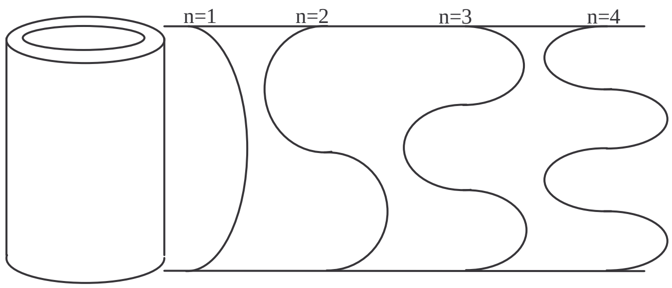

Figure 19 Piezo Harmonics

The wavelength of n^{th} harmonic is

$$\lambda_n = \frac{2l_x}{n} \tag{4.22}$$

and the wave velocity

$$c_n = f_n \lambda_n = \sqrt{Y/\rho} \tag{4.23}$$

where Y is Young's modulus and ρ is the piezo density. Thus:

$$f_n = nth\ harmonic\ \ frequency = \frac{n}{2l_x}\sqrt{Y/\rho} \tag{4.24}$$

The mechanical quality factor for each harmonic described by $s^2 + 2\zeta_n \omega_n s + \omega_n^2$ is

$Q_n = \zeta_n/2$, and we shall use one other parameter in our model:

$$\alpha_n = \pi \cdot f_n/Q_n = \left(\pi \cdot n/2l_x Q_n\right)\sqrt{Y/\rho} \tag{4.25}$$

These mechanical harmonics are then modeled as electrical parameters so that they can be matched to the electrical drivers. The piezo tube can be modeled as a simple capacitor at low frequencies:

$$C_0 = \varepsilon \cdot \frac{2\pi r l_x}{h} \tag{4.26}$$

where ε is the dielectric permittivity of the piezo tube. The piezo tube model must include the effect of harmonics, and recalling the coupled piezoelectric strain coefficient d_{31} one can calculate the n^{th} harmonic parameters:

$$C_n = \left(\frac{1}{n^2}\right)\left(\frac{8}{\pi^2}\right) d_{31}^2 Y \left(\frac{2\pi r l_x}{h}\right) \tag{4.27}$$

$$R_n = \left(\frac{\rho}{4}\right)\left(\frac{1}{d_{31}^2 Y^2}\right)\left(\frac{l_x h}{2\pi r}\right)\alpha_n = \left(\frac{\rho}{4}\right)\left(\frac{1}{d_{31}^2 Y^2}\right)\left(\frac{l_x h}{2\pi r}\right)\left(\pi \cdot n \big/ 2 l_x Q_n\right)\sqrt{Y / \rho} \tag{4.28}$$

$$L = \left(\frac{\rho}{8}\right)\left(\frac{1}{d_{31}^2 Y^2}\right)\left(\frac{l_x h}{2\pi r}\right) \text{ is a constant.} \tag{4.29}$$

so more specifically for first harmonic:

$$\begin{aligned} \frac{V_p(s)}{V_{in}(s)} &= G_1(s) = \frac{N_1(s)}{D_1(s)} \\ &= \frac{\frac{1}{R_0 C_0} s^2 + \frac{R_1}{R_0 C_0 L} s + \frac{1}{R_0 C_0 L C_1}}{s^3 + \frac{(L C_1 + R_0 C_0 R_1 C_1)}{R_0 C_0 L C_1} s^2 + \frac{(R_1 C_1 + R_0 C_1 + R_0 C_0)}{R_0 C_0 L C_1} s + \frac{1}{R_0 C_0 L C_1}} \end{aligned} \tag{4.30}$$

and more generally:

$$G_n(s) = \frac{N_n(s)}{D_n(s)} = \frac{b_{2n} s^{2n} + \ldots + b_1 s + b_0}{s^{2n+1} + a_{2n} s^{2n} + \ldots + a_1 s + a_0} \tag{4.31}$$

such that the state equations in controllable canonical form:

$$\dot{\chi} = \begin{bmatrix} 0 & 1 & 0 & \cdots & 0 \\ 0 & 0 & 1 & \cdots & 0 \\ 0 & 0 & 0 & \ddots & \vdots \\ \vdots & \vdots & \vdots & \ddots & 1 \\ -a_0 & -a_1 & -a_2 & \cdots & -a_{2n} \end{bmatrix} \chi + \begin{bmatrix} 0 \\ 0 \\ 0 \\ 0 \\ 1 \end{bmatrix} V_{in}$$

$$V_p = \begin{bmatrix} b_0 & b_1 & b_2 & \cdots & b_{2n} \end{bmatrix} \chi, \quad n = number\ of\ harmonics \tag{4.32}$$

where $a_0, a_1 ... a_{2n}$ *and* $b_0, b_1 ... b_{2n}$ are all positive scalars so that the *A* matrix is Hurwitz and therefore the harmonic electrical subsystem is BIBO stable.

This leads to our model in Figure 20. Typical piezo tube dimensions from Morgan ElectroCeramics™ [5] for a tube capable of nanometer scale motion would be l_x = 25 mm, *OD* = 25mm, *ID* = 19mm, *Y* = 65x10^9 N/m^2 and ρ = 7.75x10^3 kg/m^3 which yields:

f_1 = 58010 Hz, C_0 = 8.66 nF, C_1 = 890 pF, R_1 = 41.1 Ω and *L* = 8.46 mH. Different length tubes, or different configurations, would yield higher or lower bandwidths. Assuming one would operate below this primary harmonic frequency, the linear electrical model for the piezo tube is a third order system. The A matrix eigenvalues of the electrical subsystem for the piezo tube used for simulation are:

-1.154e+8, -2.489e+3 +3.645e+5i, and -2.489e+3 -3.645e+5i.

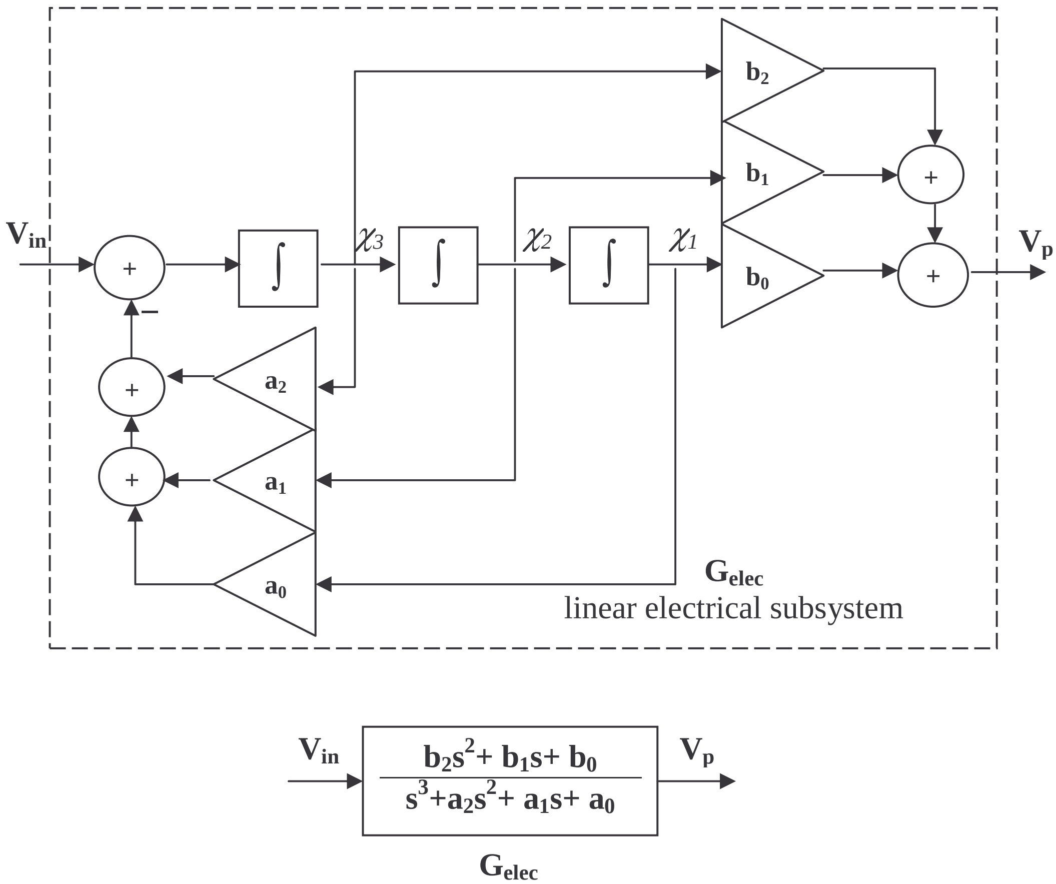

Figure 20 The Piezo actuator linear electrical subsystem.

A typical response of this electrical model (for a similar device) would resemble that of Figure 21, with *n* pole-zero pairs corresponding to resonant and anti-resonant peaks. One would normally choose to operate at a frequency below the primary harmonic frequency when using a linear control law.

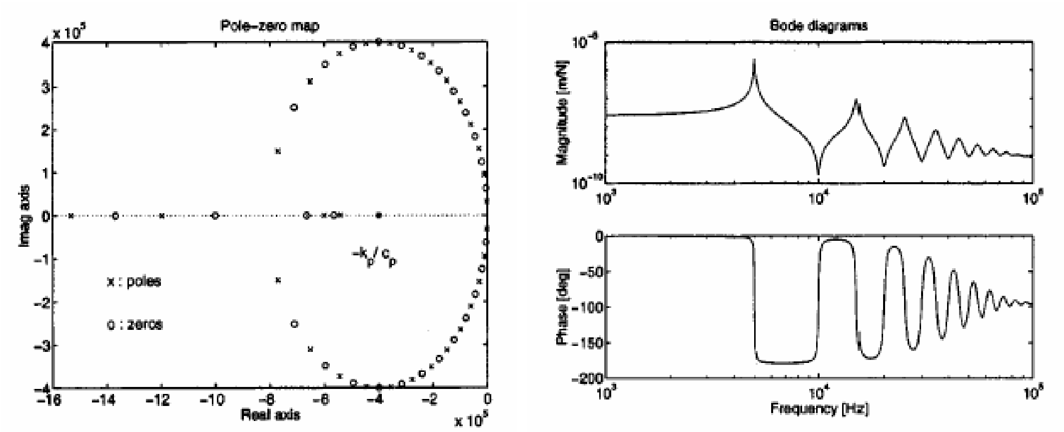

Figure 21   Root locus and Bode plots example of piezo harmonics [1].

It may prove advantageous to use singular perturbation method to decouple this electrical subsystem into two parallel additive paths, as we are most interested in the stability of the fast subsystem for our analysis, expecting the slow subsystem will remain stable as well. The singular perturbation methodology applied to the open loop electrical plant then is represented as:

$$\begin{bmatrix} \dot{\chi} \\ \varepsilon\dot{\zeta} \end{bmatrix} = \begin{bmatrix} A_{11} & A_{12} \\ A_{21} & A_{22} \end{bmatrix} \begin{bmatrix} \chi \\ \zeta \end{bmatrix} + \begin{bmatrix} B_1 \\ B_2 \end{bmatrix} V_{in}$$

$$V_p = C_1\chi + C_2\zeta \tag{4.33}$$

where:

$$A_{11} = \begin{bmatrix} 0 & 1 & 0 & \cdots & 0 \\ 0 & 0 & 1 & \ddots & \vdots \\ 0 & 0 & 0 & \ddots & 0 \\ \vdots & \vdots & \vdots & \ddots & 1 \\ 0 & 0 & 0 & \cdots & 0 \end{bmatrix} \tag{4.34}$$

$$A_{12} = \begin{bmatrix} 0 \\ 0 \\ \vdots \\ 0 \\ 1 \end{bmatrix} \tag{4.35}$$

$$A_{21} = \varepsilon\begin{bmatrix} -a_0 & -a_1 & -a_2 & \cdots & -a_{2n-1} \end{bmatrix} \tag{4.36}$$

$$A_{22} = -\varepsilon a_{2n} \tag{4.37}$$

and:

$$B_1 = \begin{bmatrix} 0 \\ 0 \\ 0 \\ \vdots \\ 0 \end{bmatrix} \tag{4.38}$$

$$B_2 = [\varepsilon] \tag{4.39}$$

$$C_1 = \begin{bmatrix} b_0 & b_1 & \cdots & b_{2n-1} \end{bmatrix} \tag{4.40}$$

$$C_2 = [b_{2n}] \tag{4.41}$$

so by defining $\zeta = \chi_{2n+1}$ and $\varepsilon = R_0C_0$ *(which is Order* 10^{-8}*)* one redefines the system in the Standard Singular Perturbation Model.

One determines that the electrical subsystem may be completely decoupled for any choice of harmonic model order *n*. For the first order harmonic the fast subsystem transient must approach the stable slow response within a time boundary $\varepsilon < \varepsilon^* = 1.88e\text{-}12$ seconds. Using the previous dimensions of the piezo the max value of the control signal input impedance, R_0 to achieve this fast response is *.00021 Ω* or an equivalent 12 gauge copper wire length ~ *40mm*. This is a realistic value and would guarantee stability of both the completely separated 'fast' and 'slow' subsystem approximate models, when separated using singular perturbation method, and for any bounded input for all t > 0.

For harmonics above first order one finds the transient must settle much faster to assure complete separation. For the second harmonic, as an example, the transient time boundary is $\varepsilon < \varepsilon^* = 3.54e\text{-}24$ seconds, $R_0 < 4e\text{-}16\ \Omega$ and a wire length $< 7.5e\text{-}14\ m$. This is not realistic, indicating one cannot make a separation assumption if one wishes to apply control input signals to this system above the first harmonic. We have thus not made a separation assumption for analysis of the ADRC control law. The simulations have assumed first order harmonics, so we have limited input signals below these frequencies.

4.1.3 The Complete Piezo Linear Model

The complete piezo linear state equation (assuming input below the first harmonic) in controllable canonical form:

$$\dot{\chi} = \begin{bmatrix} 0 & 1 & 0 & 0 & 0 \\ -k_{eq}/m & -b_{eq}/m & b_0 & b_1 & b_2 \\ 0 & 0 & 0 & 1 & 0 \\ 0 & 0 & 0 & 0 & 1 \\ 0 & 0 & -a_0 & -a_1 & -a_2 \end{bmatrix} \chi + \begin{bmatrix} 0 \\ 0 \\ 0 \\ 0 \\ 1 \end{bmatrix} V_{in}$$

$$x = \begin{bmatrix} K_{vf}/m & 0 & 0 & 0 & 0 \end{bmatrix} \chi \tag{4.42}$$

The characteristic polynomial is more space efficient to show the BIBO stability of the open loop linear system than the much longer eigenvalue calculation:

$$s^5 + \left(a_2 + \frac{b_{eq}}{m}\right)s^4 + \left(a_1 + \frac{a_2 b_{eq}}{m} + \frac{k_{eq}}{m}\right)s^3 + \left(a_0 + \frac{a_1 b_{eq}}{m} + \frac{a_2 k_{eq}}{m}\right)s^2 + \left(\frac{a_0 b_{eq}}{m} + \frac{a_1 k_{eq}}{m}\right)s + \frac{a_0 k_{eq}}{m}$$

so that the expected positive values of all scalar parameters indicate the A matrix is Hurwitz and all eigenvalues have negative real components as is the specific case for our simulation model. Where, in the general case, $V_{in}(t) \in C^n$ is assumed to be an n differentiable function of t and $a_i, b_j, m, b_{eq}, k_{eq}, K_{vf} \in \mathbb{R}_+$.

The complete linear equation of motion is represented in Figure 22.

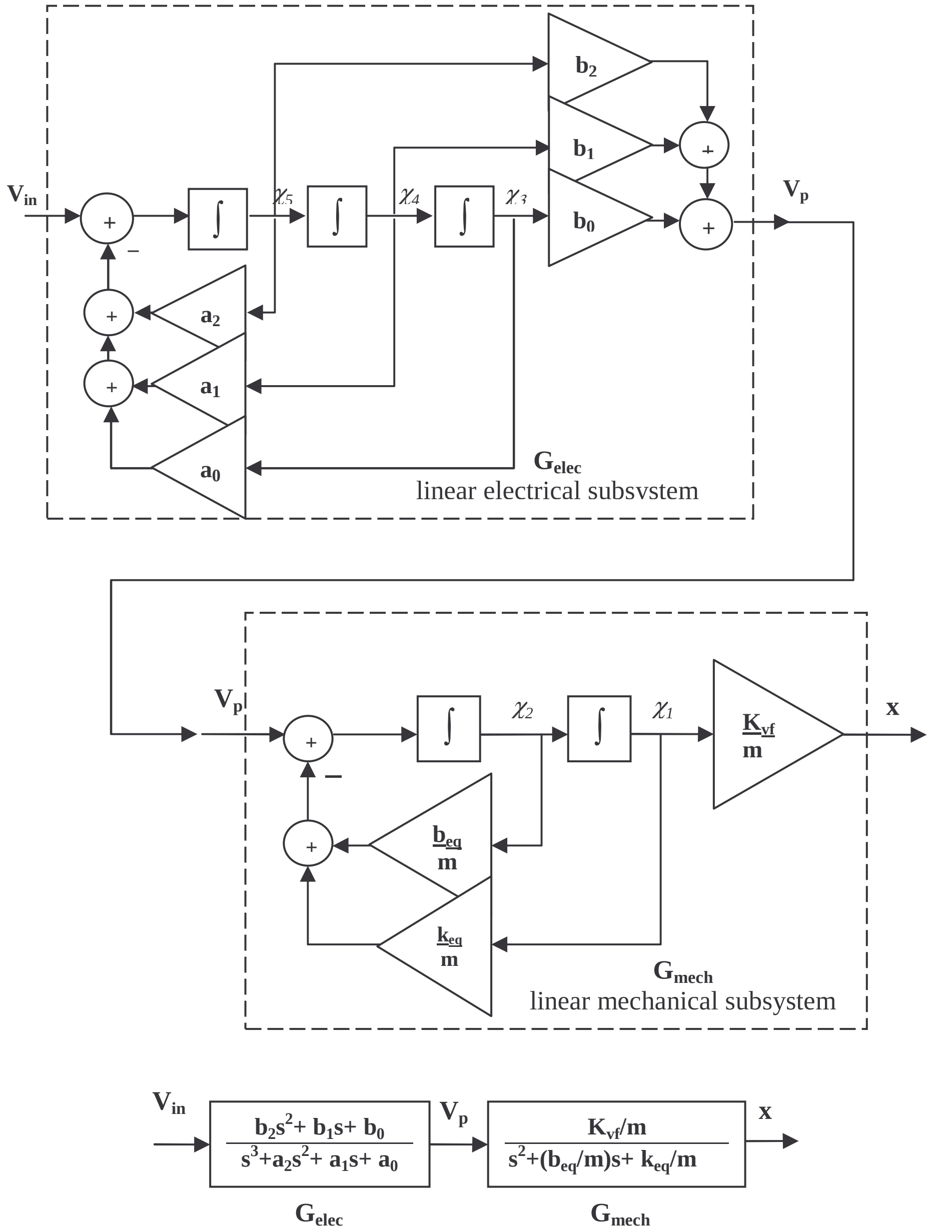

Figure 22 The Piezo actuator complete linear subsystem.

4.2 Simulation of Nonlinearities of Piezo Tube Actuators

Thermal nonlinearities are the most pronounced in piezo devices. Voltage "creep" and other elastic/plastic nonlinearities are found in piezo devices. These two nonlinearities are very slow responding compared to the hysteresis nonlinearity of piezo devices. Thermal drift and voltage creep can be and usually are modeled and controlled as slowly time varying parameters and a voltage offset drift in the motion equations.

$$F_x(V,t) = K_{vf}(t) \cdot V_p(t)(1 + t \cdot f_{creep}(V)) \qquad (4.43)$$

We will follow that same practice here in order to concentrate our control attention on the more difficult hysteresis phenomenon. In what follows we will resort to a definition of seminorms unless otherwise specifically called out as L^2 *or* L^∞ *norm*:

$$\begin{aligned} &C^0 \text{ is the space of continuous functions } f : [0,\infty[\to \mathbb{R}, \text{ with seminorm :} \\ &\|f\|_{[0,t]} := \max_{0 \le s \le t} |f(s)| \text{ for } f \in C^0 \text{ and } t \ge 0. \end{aligned} \qquad (4.44)$$

4.2.1 Thermal Drift: Simulation as a Slow Ramp Force Multiplier

As was evident in Figure 1, the thermal drift of many piezo ceramic materials can be several percent over even small changes in temperature, and does not present any obvious path to mathematic representation.

$$F_x = K_{vf} V_p \text{ where } K_{vf} = 2\pi r(c_{11}d_{31} + c_{12}d_{31} + c_{13}d_{33}) \qquad (4.45)$$

Though K_{vf} is a continuous function of the slowly changing temperature dependent coefficients c_{11}, c_{12}, c_{13}, d_{31} *and* d_{33}, these are measurable bounded values:

$$\left\|K_{vf}\right\|_{[0,T]} := \max_{0\le s\le T}\left|K_{vf}(s)\right| \le K_{vf\,\max} \in \mathbb{R}_+,\ \ for\ \ K_{vf} \in C^0\ \ and\ \ T \ge 0 \qquad (4.46)$$

and for our purpose herein we shall then assume K_{vf} as a continuous function of time:

$$K_{vf}(t) \in C^n(0,\infty) \qquad (4.47)$$

and is the un-modeled dynamic bounded difference attributed to thermal drift. Simulation of thermal drift will be accomplished with relatively slow ramp and/or sinusoid multiplier to the scalar K_{vf}^0 .

4.2.2 Voltage Creep: Simulation as a Saturated Slow Ramp Input Offset

Application of a DC bias, such as the “engage” offset voltage, to a piezo tube scanner causes an initial and abrupt change in deflection, but the subsequent “creep” to a final position is slow as in Figure 2.

Richter et al, in 2001 [104] had modeled and confirmed creep as a function of impressed voltage on the input to the mechanical subsystem, reinforcing Vieira’s earlier experimental results [125].

$$F_x(V,t) = K_{vf}(t)\cdot V_{in}(t)(1+t\cdot f_{creep}(V)) \qquad (4.48)$$

This representation is somewhat misleading, in that the value might appear unbounded, this is not the case, as f_{creep} is assumed bounded continuous function of voltage:

$$\begin{aligned} &V_{sat} \in \mathbb{R}_+ \ \ and \ \lim_{V\to V_{sat}} f_{creep}(V) = 0 \\ &so\ that\ \left\|V_{in}(t)\right\| := \max_{0\le r<t}\left|V_{in}(r)\right| \le V_{sat}. \end{aligned} \qquad (4.49)$$

so we will assume:

$$V_{in}(t)(1+t\cdot f_{creep}(V)) := V_{in}(t)+V_{creep}(t) \tag{4.50}$$

where $V_{creep}(t)\in C^{n}(0,\infty)$ is the dynamic un-modeled bounded difference attributed to voltage creep.

To repeat, the control system will necessarily need to be tolerant of slowly varying position, velocity and acceleration errors *resembling measurement uncertainty* in classic control scenarios. Simulation of position creep will also be accomplished with relatively slow ramp offsets to inputs.

4.2.3 Hysteresis: The quasilinear model choice for simulation.

One has several choices how to model the piezo actuator system, the most common method to model the piezo actuator is to separate the linear and nonlinear components of the model as in Figure 23 and Figure 24, and model the hysteresis as a series operator acting on either the input or the output of the linear subsystem. Then most researchers to date have resorted to an inverse hysteresis operator to linearize the system such that various linear control laws may be applied.

The contribution of hysteretic energy dissipation is not manifest in the commonly applied semilinear series configuration. In Chapter 3 we discussed the reasons for our preference of the quasilinear mechanical model in Figure 25.

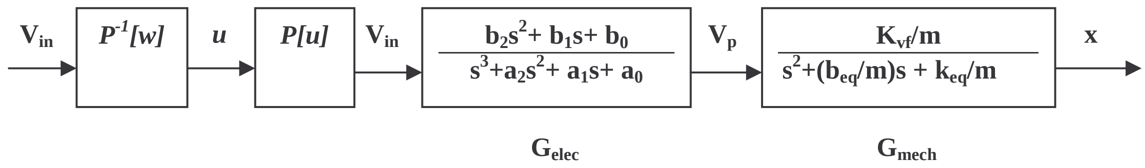

Figure 23 Semilinear piezo model with inverse hysteresis compensation.

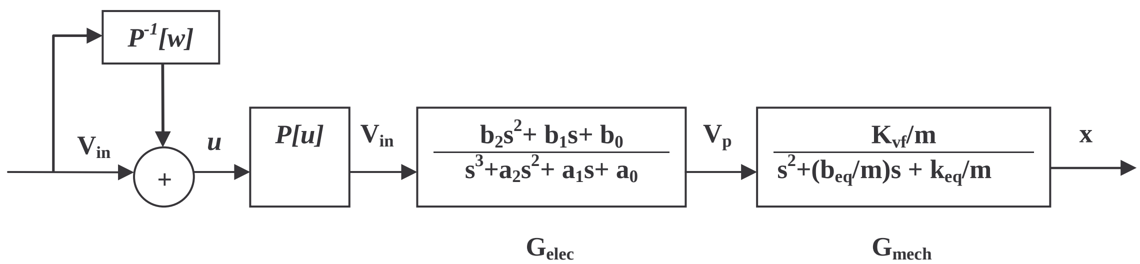

Figure 24 Semilinear piezo model with feed forward hysteresis compensation.

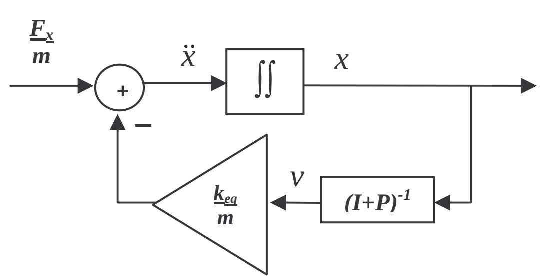

Figure 25 Quasilinear piezo mechanical model with hysteresis energy dissipation.

Our open loop piezo system model then becomes as in Figure 26.

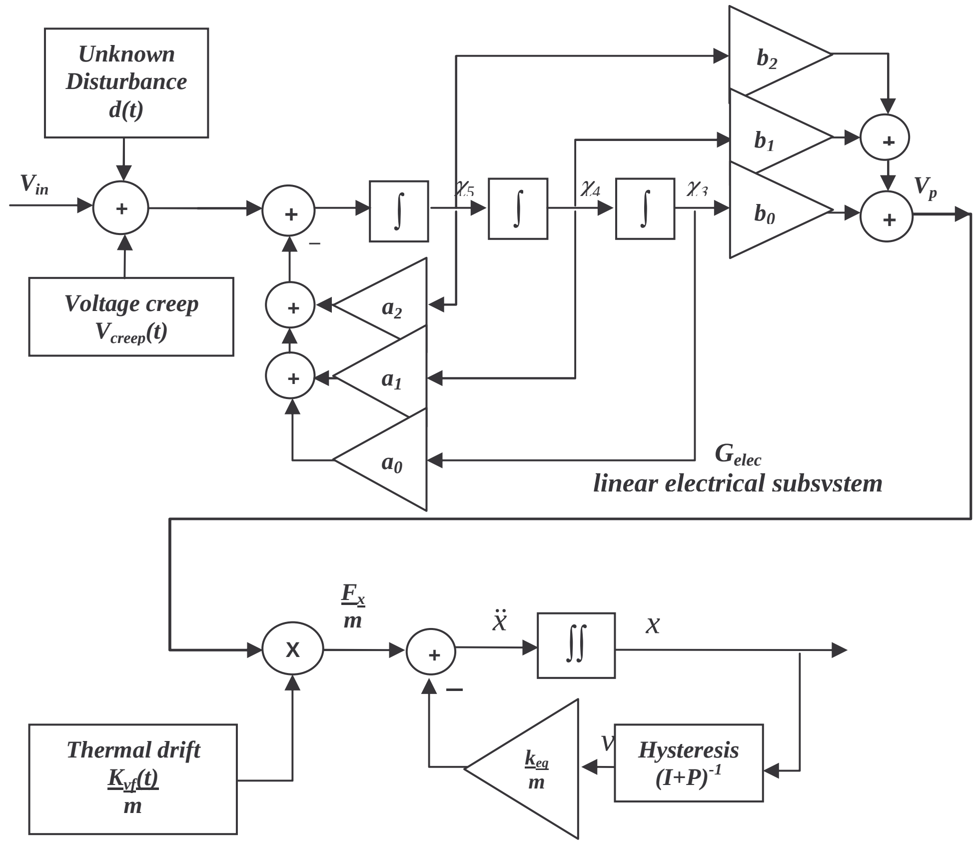

Figure 26 Complete piezo quasilinear model with hysteresis energy dissipation.

$$\begin{aligned}
\ddot{x}(t) &= \frac{F_x(t)}{m} - \frac{k_{eq}}{m} v(t) \\
&= \frac{K_{vf}(t)}{m} V_p(t) - \frac{k_{eq}}{m} (I+P)^{-1}[x](t) \\
&= f(x, (I+P)^{-1}, K_{vf}, f_{creep}, d, \ddot{V}_{in}, \dot{V}_{in}, t) + \frac{K_{vf}^0}{m} V_{in}(t)
\end{aligned} \tag{4.51}$$

4.2.4 Semilinear vs Quasilinear: Results Validate the Preference

A Comparison of the open loop simulation results for a linear system model, a semilinear model and a quasilinear model vividly illustrate the reasons for choosing the quasilinear model for the equations of motion. Simulation results are in Figure 27 and

Figure 28. The sinusoidal input (blue-solid line) is near the mechanical subsystem eigenvalue frequency and includes DC offsets and drift.

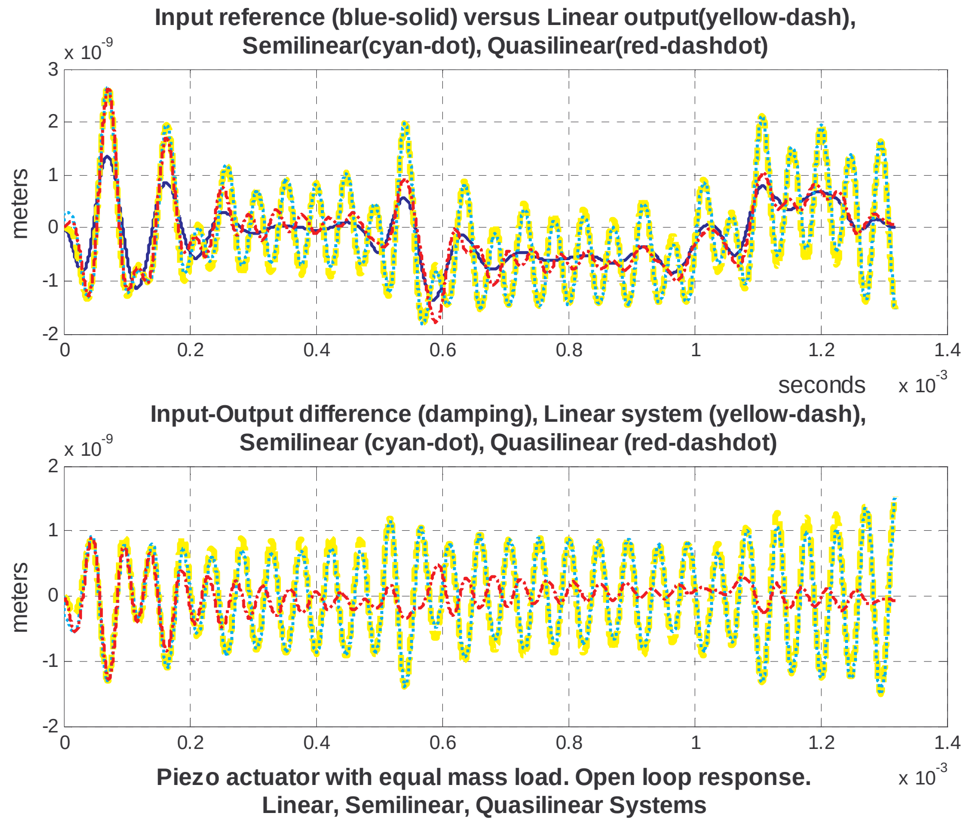

Figure 27 Open loop piezo model energy dissipation response.

The upper graphic in Figure 27 overlays the output of the three open loop models on top of the input reference signal. The lower graphic in Figure 27 overlays the difference of the three open loop models, compared to the input reference signal. The linear model and the semilinear model with a series hysteresis operator have negligible energy dissipation, dependent solely on the “equivalent hysteresis damping” coefficient, b_{eq}, and it is remarkable the series hysteresis accounts for little additional energy dissipation. The energy dissipation evident in the quasilinear model is apparent, and proportional to displacement, not rate. The values for the "equivalent hysteresis damping", b_{eq}, and "equivalent elastic coefficient", k_{eq}, were the same in the three models. It should also be noted the load mass matched the piezo actuator mass in this simulation, a large mismatch of mass would exacerbate these differences, as in other methods of actuation.

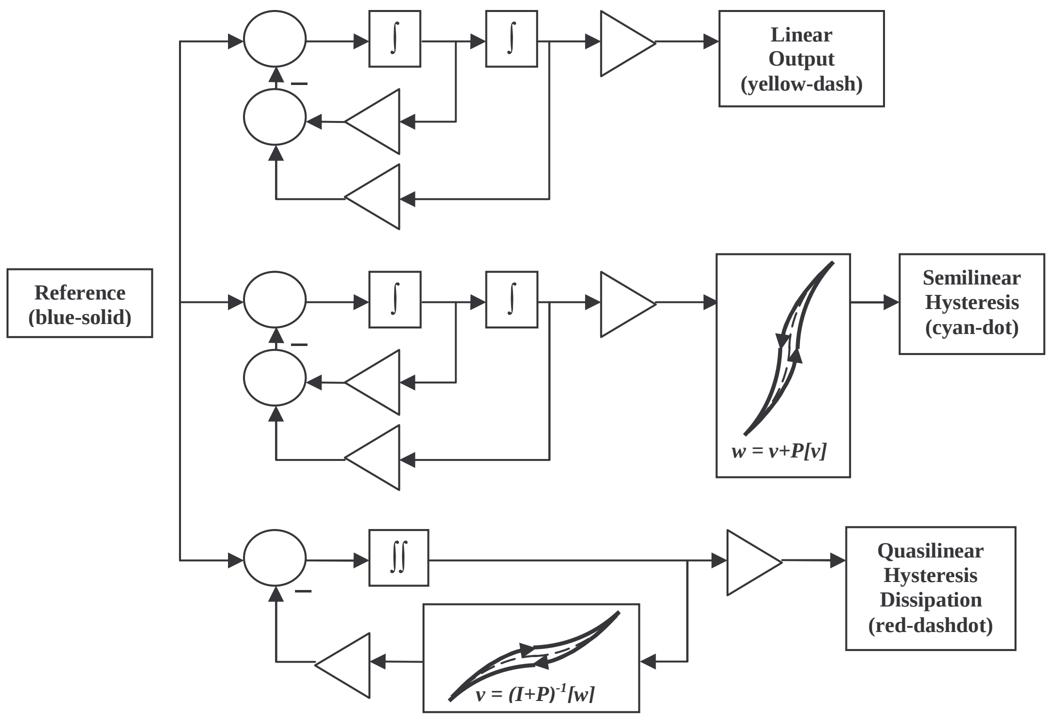

Figure 28 Open loop piezo model Simulation diagrams.

In conclusion, the difference in fidelity to experimental results between the semilinear model and the quasilinear model could not be more stark, as shown in Figure 27. The energy dissipation is well accounted and consistent with rate independent hysteresis. Thus the quasilinear mechanical model will be utilized. As for the linear electrical subsystem model, singular perturbation analysis reveals a simulation with input frequency up to the first harmonic would be validly decoupled from the mechanical subsystem, and practically achievable. The slow reacting thermal parameter drift and voltage creep are modeled as a slow time varying ramp multiplier for the voltage control variable. The unknown disturbance is modeled as either a brief square pulse equal to 50% if the max control signal during the sinusoid input period, and then followed by a 50% step offset during the 0VDC regulation period of the simulation. Thermal noise on the input reference is simulated by a white noise source equal to 1μV superimposed on the reference signal. Electrical sensor noise is also simulated by a white noise source equal to 1μV superimposed on the feedback signal.

Therefore, we will use a simulation verification model as in Figure 26 in order to validate our control design strategies. Our reference input is a 1nm sinusoid at the mechanical resonant frequency of a common piezo ceramic actuator, 21kHz. This reference is modulated by a trapezoid offset during the first 5 cycles, and then followed by 5 cycle periods of 0VDC reference input.

CHAPTER 5

CONTROL STRATEGIES IN THE DISTURBANCE REJECTION PARADIGM

Three disturbance rejection strategies, one active, one passive, and one hybrid, are considered. All three strategies are novel in their own, and certainly novel for this application to a hysteretic process. The author's thesis is that these strategies are particularly well suited for many difficult hysteretic applications, not just this application. The results demonstrate all three strategies achieve performance superior to that reported previously. Performance in this regard is the ability to compensate for the hysteresis nonlinearity, rendering the apparent system essentially linear. The LADRC has been demonstrated before to compensate for unknown disturbances and nonlinear behavior by canceling these effects and presenting an equivalent linear double integrator plant to the position controller, $\ddot{y} \approx u_0$. A similar effect can be achieved if one can find an aggressive inner velocity loop which can successfully present an equivalent single integrator plant to the position controller, $\dot{y} \approx u_0$.

Linear plants and linear controls using cascaded loops would likely be attempted here by the uninitiated, but are unsuccessful because the device energy dissipation is so low, the energy stored is so high, and the hysteresis adds additional unknown phase lag.

Variations of PID control were investigated as confirmation, in both single position loop and cascaded velocity and position configurations, with feed forward and feedback. The stable bandwidth for these controls was not acceptable, given the very low damping for the system, even without the hysteresis lag. The results are available but not part of this document, due to length. The use of a velocity reference command for an inner velocity control loop is still valid and a key component of this aggressive disturbance rejection strategy, given the appropriate reactive controls.

The active disturbance rejection strategy compensates for hysteresis disturbance by estimating and canceling its effects in real time. The passive disturbance rejection strategy compensates for hysteresis by generating a control sequence to drive the device to $\delta = 0$, the zero disturbance equilibrium, the anhysteretic behavior. The third strategy is a hybrid which combines positive attributes from both active and passive solutions. What significantly differentiates these strategies from past recorded efforts are the minimal knowledge required of the process, particularly they do not use any complex and unique inverse model of hysteresis. Hysteresis is a tedious and difficult phenomenon to characterize, and cannot be done while the process is on line, so this alone is a major positive contribution in the search for a practical solution to this application problem.

We consider control strategies which can be implemented with minimal process knowledge and tuned using a heuristic as superior to other choices, assuming they meet the performance and stability criteria, because they are more likely to be implemented and maintained. We have followed that guide herein, the controls were designed with the minimum data book knowledge and tuned using a heuristic explained in the text. Afterward we analyze the empirically designed and tuned control against our simulation model to determine how stable it might be. This analysis is noted in Appendix B: Simulation Tuning Analysis. In most cases the heuristic approached the desired response very closely.

The results for our passive disturbance rejection strategy are quite remarkable for such an elegantly simple implementation. The knowledge of the process required for these results is minimal and the margin in choosing the design and tuning parameters is relatively broad. Even more encouraging for our passive strategy alternative is that the design parameters are related to the controller hardware and software rather than the plant limitations. These are desirable choices.

The same criteria apply to our proposed active disturbance rejection strategy. One desires exceptional accuracy for tracking during transitions as well as steady state, as well as minimal reaction time to disturbances for regulation. Additionally, one should not only compensate for the nonlinear and/or un-modeled dynamics of the device, heretofore the concentration of hysteresis modeling strategies, but also compensate for the unaccountable and inevitable system disturbances. Our active control strategy should also minimize, if not completely obviate, the need for a process model, and for any process knowledge that must be used the margin of error in the estimation should be as large as possible.

5.1 The Limitations of Model-Based Control in the context of Hysteretic Dynamics

The hysteresis control problem is a definitive study in the limit of model-based control. There is still today significant debate among the engineers and applied mathematicians on the best model to use for the control of hysteretic phenomena. What is lost in the discussion is any question of the need for any model. These phenomenological models require copious data to characterize hysteresis to an acceptable level of accuracy, and even afterward the model is unique to each device controlled. The model is so computationally intense as not to be readily applied in some processes, even though computational power grows exponentially. These factors clarify and amplify the limitations of model-based control strategies for some applications.

We have therefore made a conscious choice herein to not investigate model-based control strategies. These would include state feedback controls with or without observers, H_∞ controls, loop shaping controls based on frequency domain models, etc. These have been demonstrated in prior research.

5.2 The Disturbance Rejection Paradigm provides the Necessary Capabilities

Model-based controls would not meet our “practicality” criteria, while error based linear control variations cannot be made sufficiently aggressive to compensate the hysteresis and emulate a linear plant for the outer position controller, without becoming unstable. Aggressive disturbance rejection provides the necessary capabilities.

“Aggressiveness” is a key component of our control strategy. We will shortly introduce the “Han Function”. Though one may call the Han Function “passive” because it reacts to disturbance rather than actively cancel disturbance, it is by no means passive in its reaction. Aggressive rejection of disturbance from external sources and aggressive compensation for the hysteresis disturbance is necessary for meeting the goals. This was confirmed early in our testing, a single Han Function in the position loop was difficult to apply successfully. The challenge of compensating for the natural phase lag of the device and the low dissipation and large energy storage of the device, plus the phase lag introduced by the hysteresis, put a single position loop solution “on the edge”. The introduction of an external disturbance would trigger the control to saturate to maintain performance, or the detuning to prevent control saturation would not meet performance.

Conversely, by aggressively reducing the delay in reaction to disturbance with an inner velocity loop one is able to achieve remarkable results using only the Han_1 Function. The disturbance reaction time reduction proves critical for this passive strategy as well as the active strategy. A quick reacting and aggressive inner velocity loop has a similar effect as the active disturbance rejection paradigm, the outer position control loop observes an approximate system $\dot{y} \approx u_0$.

5.3 Passive Disturbance Rejection Control: The “Han Function”

Experimental evidence has demonstrated the hysteretic response will converge to an analytic function referred to as the “anhysteretic” curve [127]. Control signal “dithering”, a technique studied [2,81,115,127] and successfully used during 1960 and 1970 decades, was demonstrated to accelerate this convergence, and was the inspiration for investigating time optimal control as the passive strategy. Dithering injects a continuous and open loop “bang-bang” disturbance into the device in order to force the device to more quickly approach the “anhysteretic” curve response. This technique is effective, but very energy inefficient. Our passive control thesis is that a nonlinear, first order, closed form discrete time optimal control introduced by Han in 1999 and further developed by Gao [37], when used as an inner velocity loop, can serve a similar purpose in a closed loop and controlled fashion, compensating for the hysteresis disturbance by driving it to equilibrium quickly and with less energy. (We shall refer to this as the “Han Function” from here forward.) This inner loop velocity control, combined with various choices of outer position loops, both linear and nonlinear, would provide an elegant solution. The choice of Han’s closed form direct discrete implementation also benefits from the fact it is a proportional control, not “bang-bang”, a weakness of “dithering”.

It will be demonstrated that the simplest 1^{st} order Han_1 Function inner velocity loop is sufficient to compensate for the +20% hysteresis nonlinearity, such that many linear control choices are available to address the fine position. We have chosen a most direct linear Proportional + Integral outer loop position controller for illustration. An additional benefit of the Han Function is its ability to passively yet effectively reject external disturbance other than hysteresis, this is also demonstrated in simulation.

We also consider a nonlinear, second order Han_2 Function outer position controller, used in concert with the simple inner loop first order Han_1 Function. These choices all work well under nominal conditions, but have different disturbance and noise rejection capabilities. It is necessary in this strategy to provide a reference velocity command, whether separately pre-computed or somehow derived from the position reference command. The accuracy of resulting position is therefore also related to the method chosen to generate the velocity reference.

The velocity of the piezo device is not assumed to be directly measurable, so we have used a simple differentiator of measured position as one means of determination for velocity feedback, this gives a less reliable measure in our simulation, which is purposeful. One may choose state estimation as done herein for the active control, or a tracking differentiator (TD) [50,51,84] for more accurate estimation. Accuracy and immunity to noise in the position measurement and/or the position reference, both of which we have simulated, are factors for this choice.

5.3.1 Description of the Han Function

Time optimal control study dates to the decades of 1950 and 1960s. It gained much attention and spawned much research leading to the optimal control theory [4] of the 1960's best associated with the Pontryagin [99] minimum principle. The well known 2nd order Continuous Time Optimal Control (CTOC) for a double integral LTI plant $\ddot{x} = u$ adheres to a sign function usually switched, (in that seldom are the conditions $x_1 + \frac{x_2 |x_2|}{2r} = 0,\ x_1 = 0$ actually met), according to the relationship of the state to the quadratic switching curve:

$$u = -r\, sign(s),\ \ s = x_1 + \frac{x_2 |x_2|}{2r} \tag{5.1}$$

Likewise the minimum time optimum control for a single integral plant $\dot{x} = u$ is:

$$u = -r\, sign(s),\;\; s = x \tag{5.2}$$

The benefits of this control law are the maximum accuracy to reference command and minimum reaction time to disturbance, with the negative cost of frequent switching of the control ("bang-bang") between its maximum values, particularly near the equilibrium state. Two most common suboptimal modifications to these control laws are the substitution of a dead zone or a linear switching region in the vicinity of the equilibrium. Another choice is replacing the *sign(s)* function with:

$$sat(s,\delta) = \begin{cases} sign(s), & s > \delta \\ \dfrac{s}{\delta}, & |s| \le \delta \end{cases} \tag{5.3}$$

In most all applications these continuous control laws must be implemented digitally, commonly being susceptible to noise and unwanted cycling. Han addressed discrete control for discrete time plants directly in 1999, developing a closed form 2nd order time optimal control law for the discrete time system, not a sampled continuous system. Han's solution benefited from the fact it is not "bang-bang" control but possesses an "Isochronic Region" (IR) wherein the control is proportional to the error and not extreme. We will summarize that development here, but not in a rigorous fashion. The results are fully explained by Gao [37] and the reader is invited to reference his detailed development.

Consider the discrete time double integrator plant:

$$x(k+1) = Ax(k) + Bu(k),\ |u(k)| \le r$$
$$where\ A = \begin{bmatrix} 1 & h \\ 0 & 1 \end{bmatrix} and\ B = \begin{bmatrix} 0 \\ h \end{bmatrix} \tag{5.4}$$

In this system *r* is the maximum control signal to be applied and *h* is the sample rate for the controller (Usually different, and slower than, the sample period for measurement system and the hardware itself). The problem definition is then to drive the state from the initial value *x(0)*, back to the equilibrium state $x(k) = [0 \quad 0]^T$ in the minimum steps with $|u(k)| \le r$.

$$find\ u^*(k),\ |u(k)| \le r,\ s.t.\ k^* = \min\left\{k \mid x(k) = [0 \quad 0]^T\right\} \tag{5.5}$$

The methodology for developing a control law is quite subtle, one treats each state *x(kh)* as the initial condition *x(0)* and calculates *u(0)* accordingly at each sampling instant, repeating until $x(k) = [0 \quad 0]^T$. A key feature of the control law is the Isochronic Region (IR), G(k), within which there is at least one $x(0) \in G(k)$ with a control sequence $u(0), u(1), \ldots u(k)$ which results in $x(k) = [0 \quad 0]^T$. Let us first determine a few of the early states for the system:

$$\begin{aligned} &x(1) = Ax(0) + Bu(0) \\ &x(2) = Ax(1) + Bu(1) = A^2x(0) + ABu(0) + Bu(1) \\ &\ldots \\ &x(k) = A^k x(0) + A^{k-1}Bu(0) + A^{k-2}Bu(1) + \ldots + ABu(k-2) + Bu(k-1) \end{aligned} \tag{5.6}$$

so that if one sets $x(k) = [0 \quad 0]^T$ one has:

$$x(0) = -A^{-1}Bu(0) - A^{-2}Bu(1) - \ldots - A^{1-k}Bu(k-2) - A^{-k}Bu(k-1) \tag{5.7}$$

and with $A^k = \begin{bmatrix} 1 & kh \\ 0 & 1 \end{bmatrix}$, *and* $A^{-k} = \begin{bmatrix} 1 & -kh \\ 0 & 1 \end{bmatrix}$ one has:

$$x(0) = \sum_{i=1}^{k} \begin{bmatrix} ih^2 \\ -h \end{bmatrix} u(i-1), \text{ and thus } G(k) = \left\{ \sum_{i=1}^{k} \begin{bmatrix} ih^2 \\ -h \end{bmatrix} u(i-1), |u(i)| \le r \right\} \qquad (5.8)$$

For the sake of brevity an explanation of the control law sequence using a graphical representation of the Isochronic Region superimposed on the x_1, x_2 phase plane is most instructive. The details can again be referenced [37] as desired by the reader.

The control sequence is dependent upon the initial state *x(0)* location in the phase plane relative to the IR. Figure 29 illustrates the first two regions, *G(1)*, the line on which an initial state *x(0)* reaches equilibrium in one step, and *G(2)*, the parallelogram within which an initial state *x(0)* reaches equilibrium in 2 steps. The additional regions G(3)…G(k) are developed accordingly to determine the Isochronic Region shown in Figure 30, highlighting the regions *G(1)* and *G(2)*. The boundaries Γ+ and Γ- mark the transition between full saturated control $|u| = r$ and the linearly scaled control region. Any state *x(0)* outside these boundaries will command a control $|u| = r$ until reaching one of the boundaries, at which time the control continues as $|u| = r$ while the state follows the boundary to reach the region *G(1)*, at which time a control signal $|u| < r$ is commanded to reach the equilibrium. A state *x(0)* within these bounds will first command a control signal $|u| < r$ which will drive the state *x(1)* onto the boundary, from which the state will again follow the boundary until region *G(1)*, and then to the equilibrium. The IR example herein assumes particular values of *r* and *h*, but the general shape is consistent for different parameter values, any differences consist of dilation and shear.

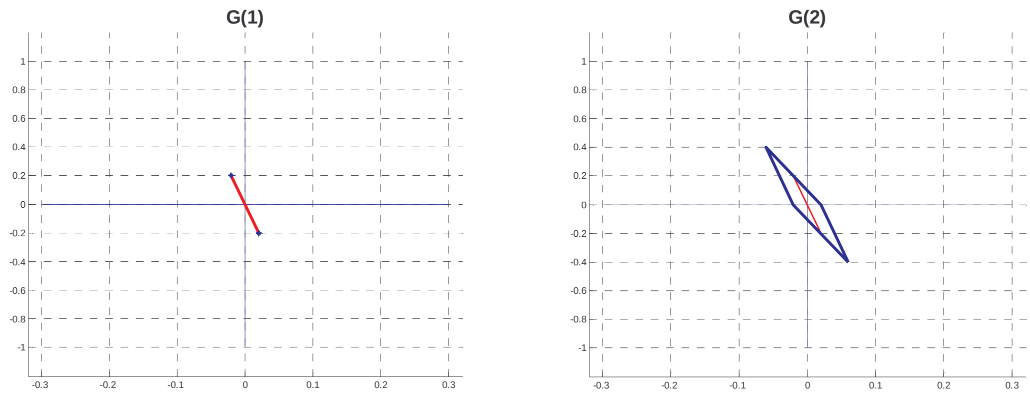

Figure 29   Regions G(1) and G(2) for the Han$_2$ Function construction

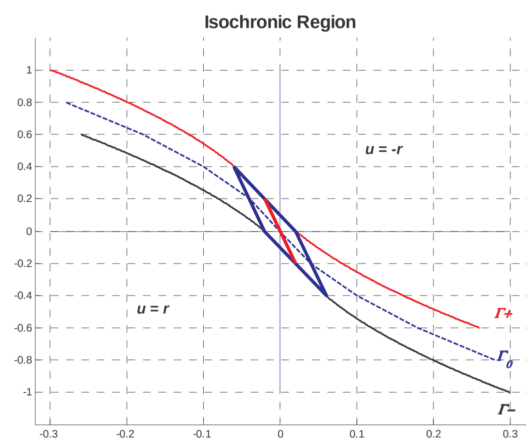

Figure 30   Han$_2$ Function Isochronic Region

The full 2nd order discrete time optimal control (Han$_2$ Function) is written as Equation (81). It is interesting to compare the switching curves for the minimum continuous Time Optimal Control with that of the Han$_2$ Function shown in Figure 31.

$$
\begin{aligned}
&u = han_2(x_1, x_2, r, h) \\
&d = rh;\ d_0 = hd \\
&y = x_1 + hx_2 \\
&a_0 = \sqrt{d^2 + 8r|y|} \\
&a = \begin{cases} x_2 + \dfrac{a_0 - d}{2} sign(y), & |y| > d_0 \\ x_2 + \dfrac{y}{h}, & |y| \le d_0 \end{cases} \\
&han_2 = -\begin{cases} r\, sign(a), & |a| > d \\ r\dfrac{a}{d}, & |a| \le d \end{cases}
\end{aligned}
\tag{5.9}
$$

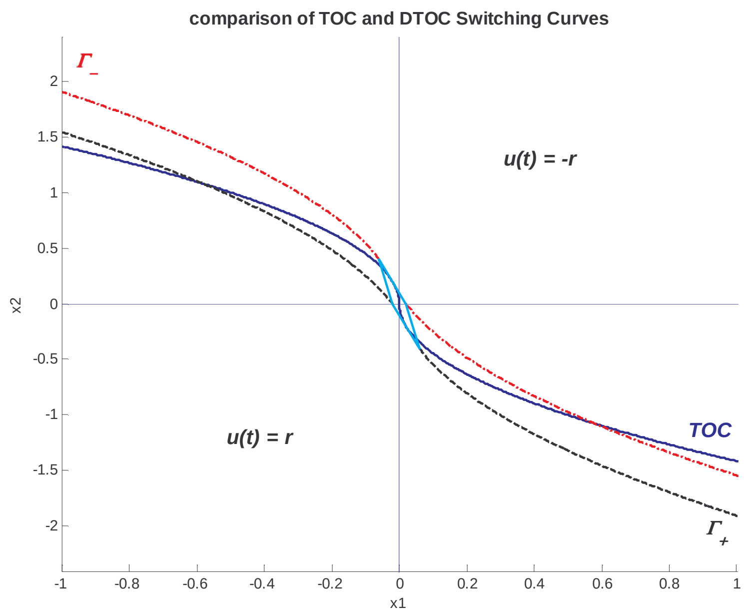

Figure 31 Han$_2$ Function versus continuous TOC switching curves

The 1st order Han$_1$ Function law for $x(k+1) = x(k) + hu(k)$, analogous to collapsing the linear switching zone for the 2nd order system down to that section of the x axis lying between $-rh$ and $+rh$, is:

$$
\begin{aligned}
&u = han_1(x, r, h) \\
&d = rh \qquad\qquad\qquad\qquad\qquad\qquad\qquad\qquad\qquad\qquad\qquad\qquad\qquad\qquad (5.10)\\
&han_1 = -\begin{cases} r\,sign(x), & |x| > d \\ r\dfrac{x}{d}, & |x| \le d \end{cases}
\end{aligned}
$$

An example of the 1st order Han_1 Function control sequence for two different initial values of *x(0)* are illustrated in Figure 32, which is the G(1) line extended infinitely. Full control available, |*u*| = *r*, is commanded until the state |*x(k-1)*| < *rh*, at which time a linearly scaled control |*u(k)*| < *r* is applied to reach the equilibrium *x(k)=0*.

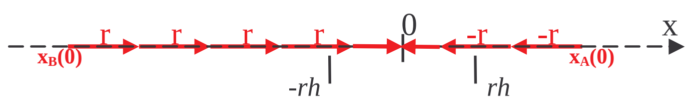

Figure 32 1st order Han_1 Function paths to equilibrium

We will demonstrate both 1st and 2nd order Han Function in simulation, as they provide the benefits of TOC while alleviating the costs of digitizing a continuous TOC.

5.3.2 Design and Tuning considerations for the Han Function

The Han Function design parameters are the maximum control value, *r*, a limit of the power source, and the step size, *h*, can be chosen as some multiple of the sampling period, T_s. The value of *r* is first, and obviously, bounded by the physical maximum control value available, so in practice one normalizes the gain *r*, after the Han Function block. For the piezo actuator used herein, which has an electromechanical "gain" $dx/dV \approx -1e^{-9}$ one need begin with a value $r > 1e^{9}$ in order to approach the physical control limit set for our simulation, $\pm 1V$. One can rapidly arrive at a usable solution using the following heuristic. The choice of "gain", r, determines most the accuracy and disturbance rejection time for the Han Function. Find that value of r to achieve desired response, usually with continuous control cycling. The value for step size, h, then serves to modify the width of the Isochronic region between Γ^- and Γ^+. This adjustment relieves the control from rapid switching "chatter", and also serves to raise the tolerance of the system to noise. Indeed, in a noisy environment this is the parameter to alter.

5.3.3 Velocity Loop with Han_1 Function

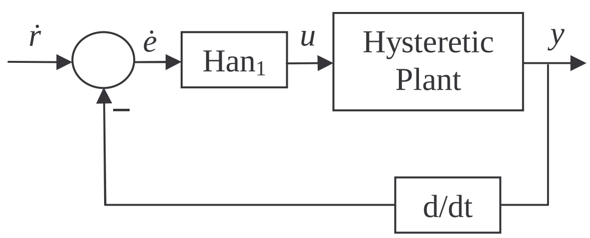

Figure 33 System Diagram, Han_1 Function in velocity loop

One must immediately remark this most simple 1st order Han_1 Function Controller, velocity only, has significantly compensated for the hysteresis nonlinearity WITHOUT a MODEL incorporated in the controller. The hysteresis we have modeled in the simulated plant has almost 20% nonlinearity. Figure 34a is the plot of the signal transform through the inverse hysteresis operator in the mechanical force feedback, indicating the nonlinear strain. Figure 34b is the position transform for the closed loop velocity controlled piezo, from reference to output. The piezo now appears essentially linear, the input is a velocity reference, $\dot{r}$, and the output is the position y. The velocity loop Han$_1$ Function has made the plant appear as $\dot{y} \approx u_0$ for any outer loop position control.

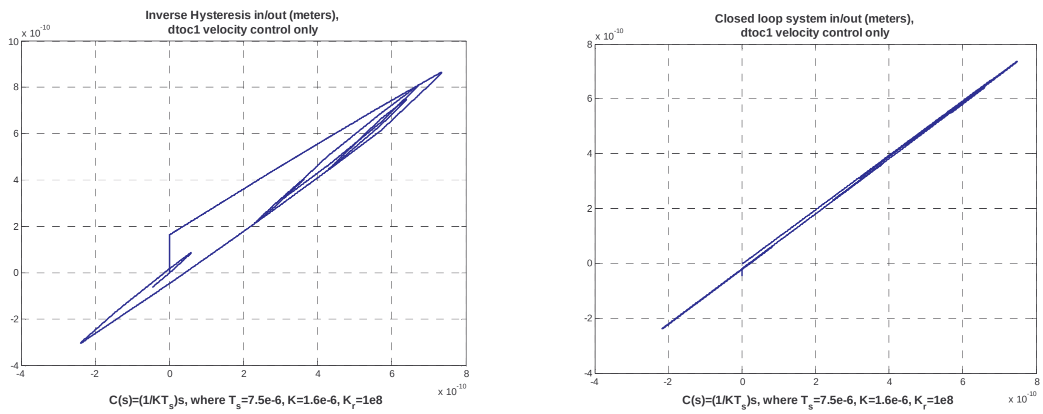

Figure 34 Hysteresis before and after Compensation, Han$_1$ Function velocity control

This configuration establishes a baseline for other comparisons. The controller is easy to implement in hardware using an amplifier with saturation in the velocity loop. The control appears as a negative gain (the piezo is a negative divisor) derivative control for small errors and signals within the Isochronic Region, and is tuned accordingly. The velocity reference must be fed forward to the velocity feedback loop, with the suggestions made earlier regarding the generation of this reference. The accuracy results in Figure 35 with this elegantly simple standard component configuration are remarkable, particularly the fact the hysteresis nonlinearity is almost totally compensated by the velocity loop, allowing the outer fine position loop to better manage the accuracy performance requirements. What is also remarkable is the ability of the 1st order Han$_1$ Function velocity control to resolve disturbances before the position loop, and the low level of control effort applied to achieve the result, due in no small part to the Han Function minimal time response. It is a noteworthy reminder here, as is true for all the simulations, that the input reference is a sinusoid at the natural frequency of the mechanical subsystem, which has minimal natural damping. This is a system normally to be avoided by the classic “bang-bang” continuous TOC control law.

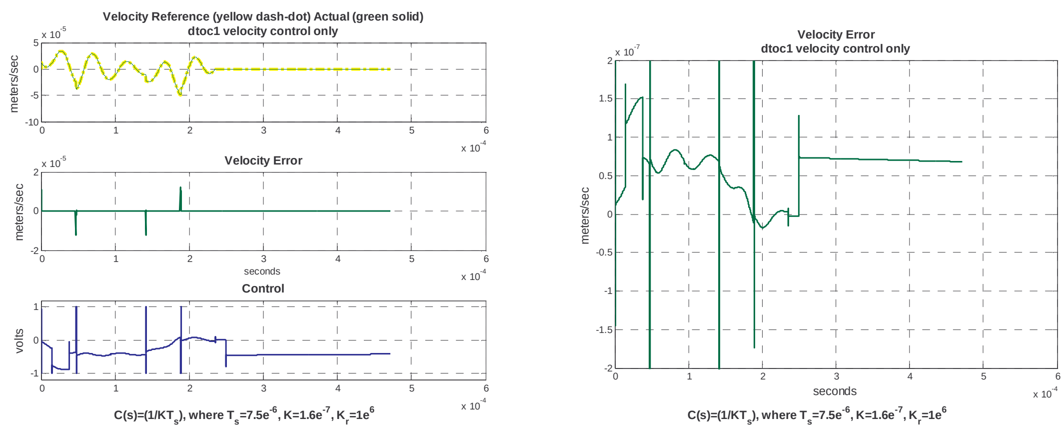

Figure 35 Velocity, Error and Control results for Han_1 Function velocity control

The velocity tracking error in this case is $<2e^{-7}/8e^{-5} = 0.25\%$. Notice also the single sample period tracking error transients are triggered by the abrupt velocity changes due the triangle and square pulse modulation in the reference inputs, and not by the disturbances to the system. This would indicate an appropriate reference input filter would alleviate this issue, separate from the controller. This will be seen consistently in all simulation results, to a greater or lesser degree. It must also be brought to attention the simulated 50% max load disturbances are also effectively quelled by the 1st order Han_1 Function. And not least, the control signal is well bounded less than the ±1V saturation constraint. This also emphasizes the benefit of the time optimal response.

The simulation reference signal is a 1 nanometer peak to peak sine wave modulated by a triangle signal and offset by DC bias at various intervals for ~235µsec, to test tracking, eventually returning to zero and holding zero for another 235 µsec in order to test steady state regulation and disturbance rejection. This period, to be precise, corresponds to 5+5=10 cycles at the primary frequency of the mechanical system (21kHz). One will note the large pulses in the error and control due to the transitions of triangle modulation and DC offset periods. The system experiences a 25 μsec wide pulse disturbance equal to 50% of peak force beginning at 10 μsec, and another 50% of peak force step disturbance beginning at 250 μsec.

For our simulations we have chosen to normalize based on our knowing the model parameters: $\bar{u} = 1$ (*max control force*), $T_s = \dfrac{1}{\omega_r} = \dfrac{1}{133k}$ (*sampling period*) so that we can stress the simulation by driving input at the resonant frequency and limiting the control to ±1V.

5.3.4 Cascade Control: Han$_1$ Function velocity loop with PI position loop

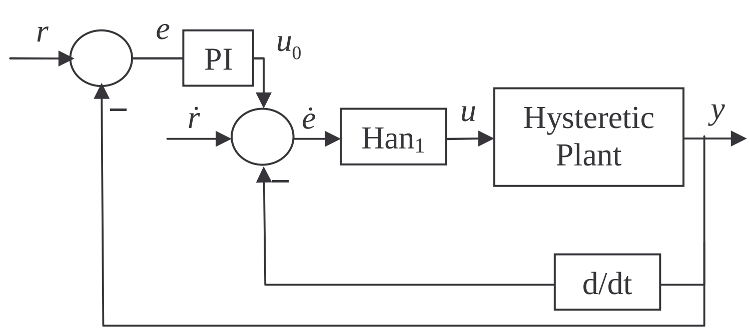

Figure 36 System Diagram, Cascade Han$_1$ Function velocity loop with a PI position loop

It should be obvious, given the results from the velocity inner loop controlled with the 1st order Han$_1$ Function, that a linear PI control as the outer position loop would yield good results. The hysteresis compensation in Figure 37 and the tracking accuracy and control effort in Figure 38 illustrate these results.

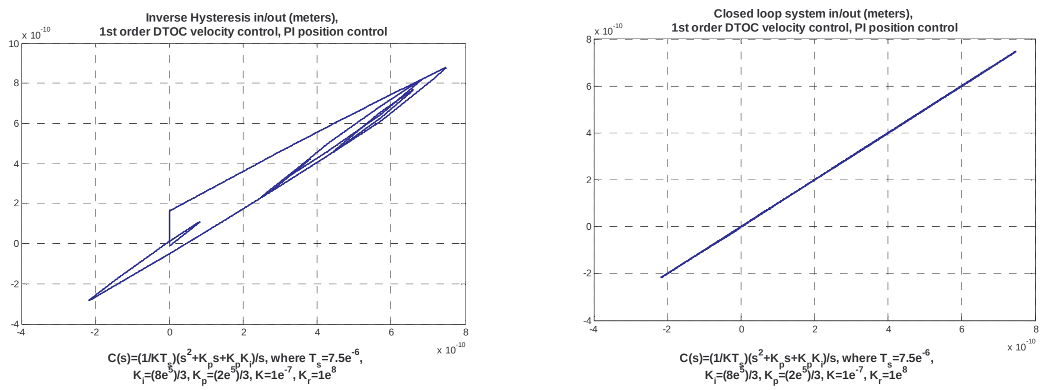

Figure 37 Hysteresis response before and after Compensation, Han_1 Function velocity with PI position control

One observes immediately the control is well behaved, as the Han_1 Function velocity control is tuned independently, and then the PI position control is connected. The controller does cycle in the presence of noise, and this can be adjusted with the width of the Isochronic Region, if desired. (This was purposely not done here for illustration) The max error during discontinuous inputs is $<6e^{-12}/1e^{-9} = .6\%$, which can be addressed by careful input profiling. The noise error is $<11e^{-13}/1e^{-9} = .1\%$, and better still is stable damped rather than oscillatory. The 50% disturbance rejection is quite good, with error $<5e^{-13}/1e^{-9} = .05\%$.

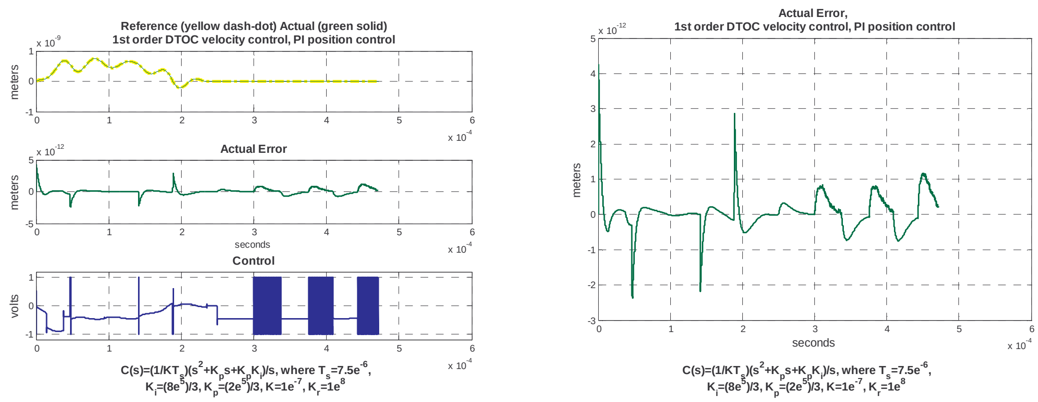

Figure 38 Position, Error and Control Signals, Han_1 velocity with PI position control

The simulated system additionally experiences zero mean random noise injection of ±1uV at the reference input for ~25 µsec beginning at ~300 µsec, ±1uV at the output feedback for ~25 µsec beginning at ~350 µsec, and both sources simultaneously for ~25 µsec beginning at ~400 µsec, each random source has a different kernel. This noise level is consistent with radiated noise entering via the feedback measurement, and thermal noise and/or electrical noise in the reference input.

5.3.5 Parallel Control: Han_2 Function position and Han_1 velocity control

One designs this system as one would design most cascaded loop systems, adjust the velocity loop to achieve the best following, which was done as part of the single 1st order Han_1 Function control, and then tune the 2nd order Han_2 Function position loop to fine tune error.

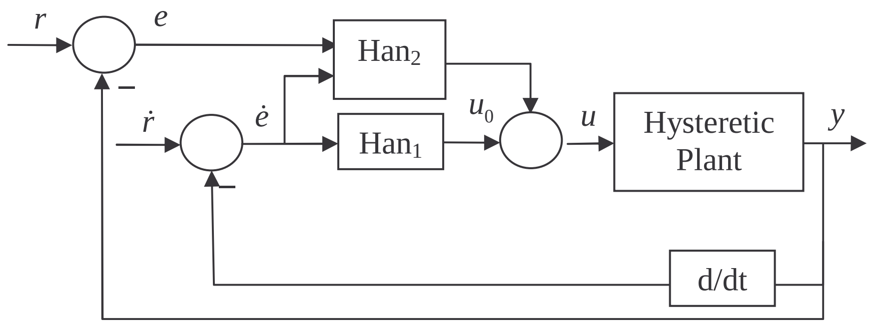

Figure 39 System Diagram, Parallel Han_2 Position and Han_1 Velocity loops

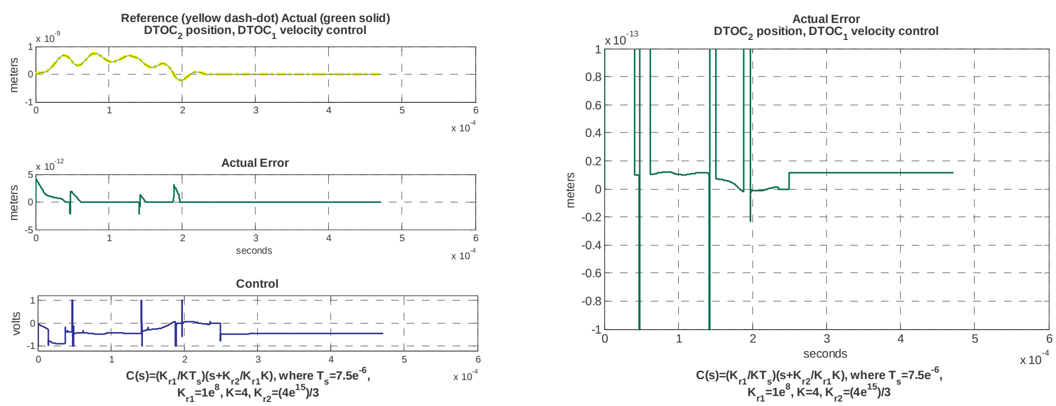

Figure 40 Han_2 Function position, Han_1 velocity: Position Error and Control results

The 2nd order Han_2 Function has small signal steady state error bounded by choice of rh^2, this may be preferable to the dynamics that accompany linear controls. The max tracking error in Figure 40 is larger than the steady state error, tracking error $<5e^{-12}/1e^{-9} = 0.5\%$ while steady state error $<2e^{-14}/1e^{-9} = 0.002\%$. Even so, $<0.5\%$ error is significantly lower than some of the inverse model-based systems studied. Notice also the max tracking error is triggered by the abrupt velocity reference changes and not by the disturbances to the system, this would indicate an appropriate reference input filter would alleviate this problem, separate from the controller, leaving one with a *.002%* disturbance rejection controller for this Han Function pair.

5.4 Active Disturbance Rejection Control

For the active compensation strategy we have chosen a novel concept known as Active Disturbance Rejection Control (ADRC) using an Extended State Observer (ESO). The ESO is normally executed as a linear full state observer, with an augmented state estimating the contribution of nonlinearities and poorly modeled dynamics to the measured position output. The ESO and ADRC strategy has been demonstrated exceptionally capable [35-40,43,48,49,58,59] to control macro and micro scale processes, this will be a first effort to control at the nanometer scale. The objective for ADRC using ESO is simplicity itself, to estimate the effect of any unknown phenomena and compensate in real time via the augmented state in the ESO. What differentiates this from other augmented state observers is that a model for the process is not required to assemble the observer. An ESO using a linear Proportional + Derivative (PD) control strategy will be demonstrated, referred to as Linear ADRC (LADRC) or ADRC(PD). The results are extraordinarily effective, demonstrating the ESO ability to estimate and compensate for the hysteresis, in real time, without benefit or complexity of an inverse hysteresis model.

5.4.1 The ADRC Paradigm

The functional relationship between the input force and acceleration is:

$$\ddot{x} = f(\dot{x}, x, w, u) \tag{5.11}$$

where x is our position output, u is our force input, and w accounts for un-modeled dynamics in the system state and input, as well as unknown disturbances, including hysteresis. Let r represent the reference trajectory for a tracking application such that $e = r - x \; and \; \dot{e} = \dot{r} - \dot{x}$ so the goal for tracking and regulation control is to drive their error to zero. One may also choose to be one step less abstract in the description of the process:

$$\ddot{x} = f(\dot{x}, x, w) + bu, \; b \in \mathbb{R} \tag{5.12}$$

where all the nonlinearities and forces not traceable to the linear application of u is enveloped by the function $f(\dot{x}, x, w)$. Therefore, if the desired response of the system is that of a simple linear double integrator:

$$\ddot{x} = u_0 \tag{5.13}$$

then our necessary control is obviously:

$$u = \frac{u_0 - f(\dot{x}, x, w)}{b} \tag{5.14}$$

Granted, this is an ideal configuration, yet the philosophy of ESO and ADRC is to asymptotically approach this ideal. The control challenge then becomes how accurately one can estimate the value of $f(\dot{x}, x, w)$ in real time, so that now one designs a simple control u_0 rather than a complex u. In fact, the robust Han_1 Function is a prime candidate for u_0. This is the essence of the ADRC, whereby the real, poorly modeled, disturbed process is made to appear to the controller as a well behaved and trivial linear system. There is nothing novel to estimate disturbances and compensate for them, as this has been a practice of Disturbance Observers (DOB) for some years, but the method of estimation using the ESO is new.

The design of the ESO is thus the determining component for a successful implementation of ADRC. The ESO was proposed by Han [48,49] but significantly simplified and made practical by Gao [38-40]. The ESO is an augmentation of a full order state observer where $x_1 = x,\ x_2 = \dot{x}, and\ x_3 = f$ so can be described as a linear system with all nonlinear behavior being represented by f and $h = \dot{f}$. The linear representation of the state matrix A is also consistent with the boundary conditions of the hysteretic device and the quasilinear representation for the hysteresis. The hysteresis contribution enters via the internal dynamics of the device and not through the input force. The integral relations between acceleration, velocity and position at the device boundary hold.

$$\begin{aligned} \dot{x} &= Ax + Bu + Eh \\ y &= Cx \end{aligned} \tag{5.15}$$

with $A = \begin{bmatrix} 0 & 1 & 0 \\ 0 & 0 & 1 \\ 0 & 0 & 0 \end{bmatrix},\ B = \begin{bmatrix} 0 \\ b \\ 0 \end{bmatrix},\ C = \begin{bmatrix} 1 & 0 & 0 \end{bmatrix},\ E = \begin{bmatrix} 0 \\ 0 \\ 1 \end{bmatrix}$ and a state observer:

$$\begin{aligned} \dot{z} &= Az + Bu + L(y - \hat{y}) \\ \hat{y} &= Cz \end{aligned} \tag{5.16}$$

may be designed with observer gains $L = [\beta_1 \quad \beta_2 \quad \beta_3]^T$. Han [48,49] proposed a generic nonlinear observer gain vector, Gao [38-40] proposed a more practical Linear ESO

(LESO) whereby the observer eigenvalues are parameterized and repeated at a single frequency so that ω_o is the single design parameter required for the observer:

$$\begin{aligned}&\lambda_o(s) = s^3 + \beta_1 s^2 + \beta_2 s + \beta_3 = (s+\omega_o)^3 \\ &\Rightarrow \beta_1 = 3\omega_o,\ \beta_2 = 3\omega_o^2,\ \beta_3 = \omega_o^3\end{aligned} \tag{5.17}$$

The resulting values of $z_1 = \hat{x},\ z_2 = \hat{\dot{x}},\ z_3 = \hat{f}$ and the control law:

$$u = \frac{u_0 - z_3}{b} \tag{5.18}$$

will reduce the plant to:

$$\ddot{x} = (f - z_3) + u_0 \approx u_0 \tag{5.19}$$

so that we have achieved our design goal and may choose among many controls appropriate for our double integrator equivalent plant.

5.4.2 The ADRC with PD control (LADRC)

A double integrator system is easily controlled by a proportional + derivative controller:

$$u_0 = K_p(r - x) - K_d \dot{x} \tag{5.20}$$

where one may choose to use measured values for $x \text{ and } \dot{x}$ or use their estimated values $z_1 \text{ and } z_2$ respectively, from the LESO. One may simplify the choice of the gains K_p and K_d by placing both poles for the closed loop equivalent system at the same critically damped location:

$$G_{cl}(s) = \frac{\omega_c^2}{s^2 + 2\omega_c s + \omega_c^2} = \frac{K_p}{s^2 + K_d s + K_p}$$
$$\Rightarrow K_d = 2\omega_c,\; K_p = \omega_c^2 \tag{5.21}$$

so that one may only concern oneself with tuning the controller bandwidth, ω_c. This implementation is very practical and effective. It is referred to as the Linear ADRC (LADRC) implementation because of the linear gains.

The tuning heuristic for the LADRC is followed herein, and that is to begin with an observer frequency $\omega_o \approx 10x$ the max frequency at which one desires to operate, and then use a scaled controller frequency $\omega_c = \omega_o/3$. In our stressful simulation case that desired operating frequency is the natural resonant frequency of the mechanical subsystem, $4e^5/3$ *rad/sec*, which implies an initial $\omega_o = 4e^6/3$, $\omega_c = 4e^6/9$.

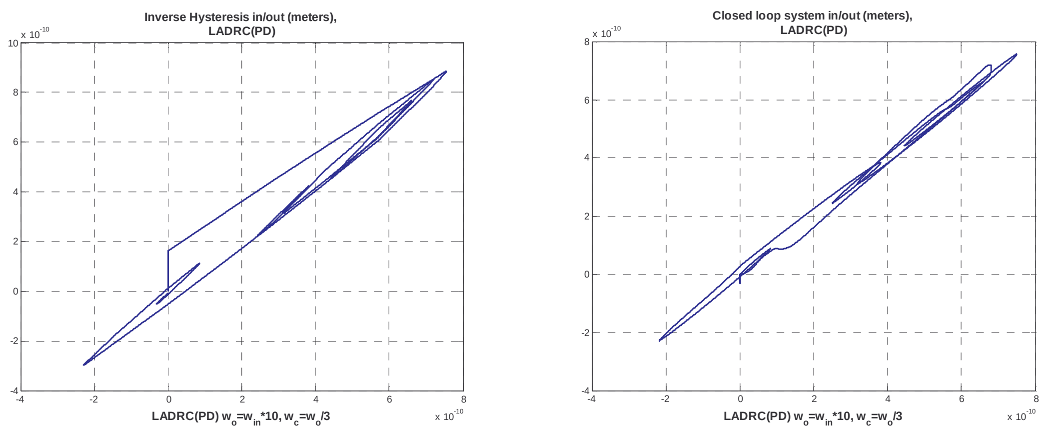

Figure 41 Hysteresis before and after Compensation, LADRC(PD) Minimum Observer Bandwidth

(LADRC with PD position control, observer frequency $\omega_o = 10\omega_{in}, \omega_c = 3\omega_o$*)*

The insufficient effect on hysteresis compensation is obvious in Figure 41, and this is the most serious limitation for our thesis. This result illustrates the author's preference using the LADRC to resolve disturbance rejection issues, with low control effort, has involved dominantly linear systems. This system is dominantly nonlinear, and this puts our heuristic bias to an enlightening test. Subsequent results will reinforce the bias for the LADRC but with an altered design heuristic.

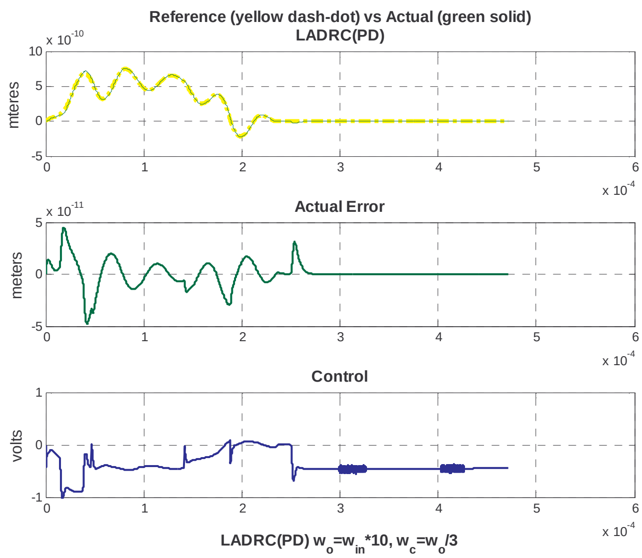

Figure 42 Position, Error and Control, LADRC(PD) Minimum Observer Bandwidth

(LADRC with PD position control, observer frequency $\omega_o = 10\omega_{in}, \omega_c = 3\omega_o$*)*

One can observe in Figure 42 the disturbances at 0, 50, 140 and 190 μsec due to the mismatch of the modulating triangle and square wave signals which introduce discontinuities (bounded) into the velocity (derivative) reference of the main sinusoid position reference signal. This error is $\sim 1e^{-11}/1e^{-9} = 1\%$ for this control and serves to emphasize the issue of discontinuities in the reference input for ANY control choice. One will observe this error in all control systems, to a greater or lesser degree, as it is caused by the sample time delay to respond to the changing reference signal. The lesson for any application engineer is the attention which should be given to supplying “smooth” reference signals. Controls are designed to NOT reject reference signals.

The trade between noise immunity versus accuracy and disturbance rejection is well illustrated in Figure 43. The reference noise error is *~1e*$^{-14}$*m=0.001%* because the observer frequency is low and practically zero measurement noise is injected into the system. Unfortunately, the accuracy and disturbance rejection is an unacceptable level, *~4e*$^{-11}$*/1e*$^{-9}$ *= 4%*, with this observer and controller frequency.

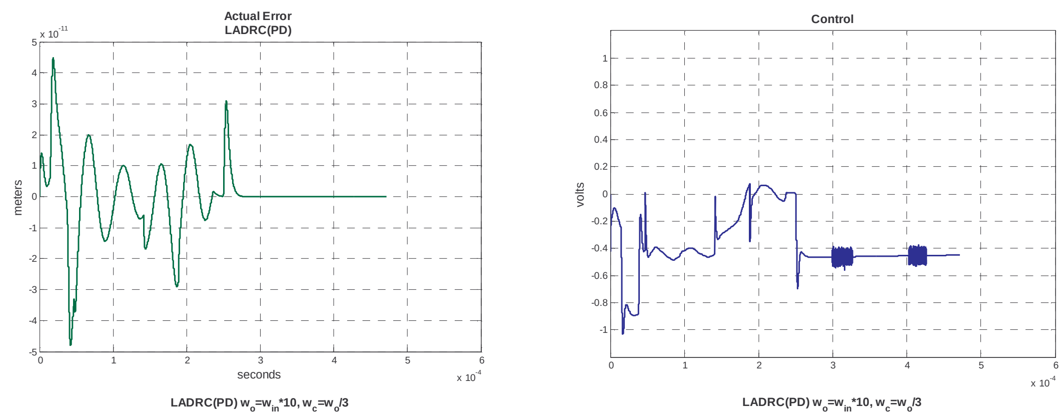

Figure 43 Position Error and Control details, LADRC(PD) Minimum Observer Bandwidth

(LADRC with PD position control, observer frequency $\omega_o = 10\,\omega_{in},\, \omega_c = 3\,\omega_o$*)*

Given the unacceptable response using the “normal” design heuristic one would next raise the observer frequency a factor of 10, and accordingly the controller frequency. This increases DC gain *100 fold* and the bandwidth *10x* while remaining stable. The result in Figure 44 and Figure 45 now provides the support for our thesis that the LADRC can easily compensate for the hysteresis nonlinearity.

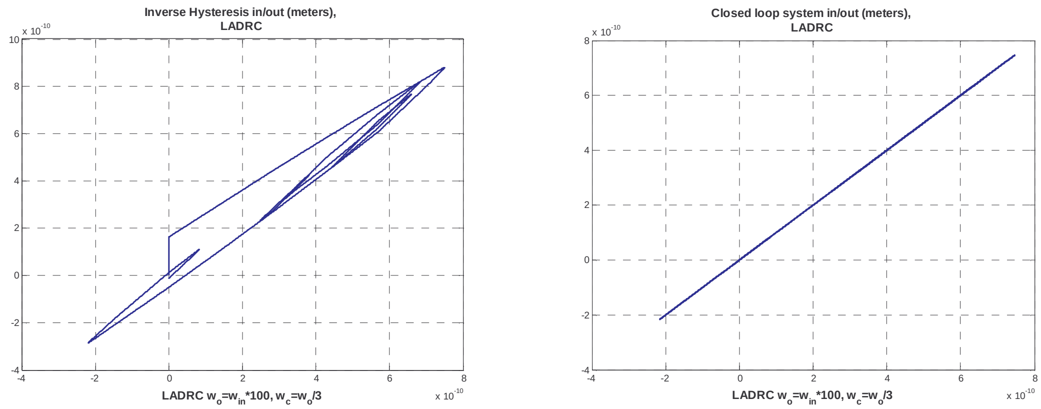

Figure 44 Hysteresis before and after Compensation, LADRC(PD), Recommended Observer Bandwidth

(LADRC with PD position control, observer frequency $\omega_o = 100\omega_{in}, \omega_c = 3\omega_o$)

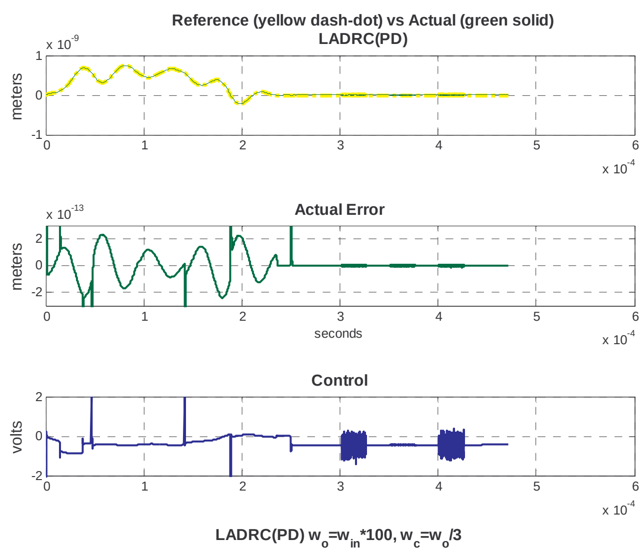

Figure 45 Position, Error and Control Signal, LADRC(PD), Recommended Observer Bandwidth

(LADRC with PD position control, observer frequency $\omega_o = 100\omega_{in}, \omega_c = 3\omega_o$)

One can now more easily observe in Figure 46 and Figure 47 the disturbances at 0, 50, 140 and 190 μsec due to the mismatch of the modulating triangle and square wave signals mentioned earlier. This error is now $\sim 1e^{-12}/1e^{-9} = .1\%$ (which is good, by the way) due to the more aggressive control. The peak control signal (±4V), Figure 47, necessary to achieve this response is well below the limits of the piezo device, and is proportional to the accuracy or disturbance rejection desired, as comparing Figure 43 and Figure 46 illustrate.

The trade between noise immunity versus accuracy and disturbance rejection in Figure 46 and Figure 47 is now better shown. The noise error $\sim 1e^{-14}m$, which is now discernable, but the control effort is now greater to achieve the measurement noise suppression, because the observer frequency is higher and more measurement noise is injected into the system. The reference noise impact is unchanged. Fortunately, the accuracy and disturbance rejection is affected directly by the change in observer and controller frequency. The max error for the system is now $\sim 2e^{-12}/1e^{-9} = 0.2\%$, for only a sample period and during the input discontinuities which have been mentioned previously. Most encouraging, the nominal error is $\sim 2.3e^{-13}/1e^{-9} = .023\%$ *and* $<3e^{-13}/1e^{-9} = .03\%$ disturbance error, which is outstanding, an order of magnitude better than those controls previously reported in the literature.

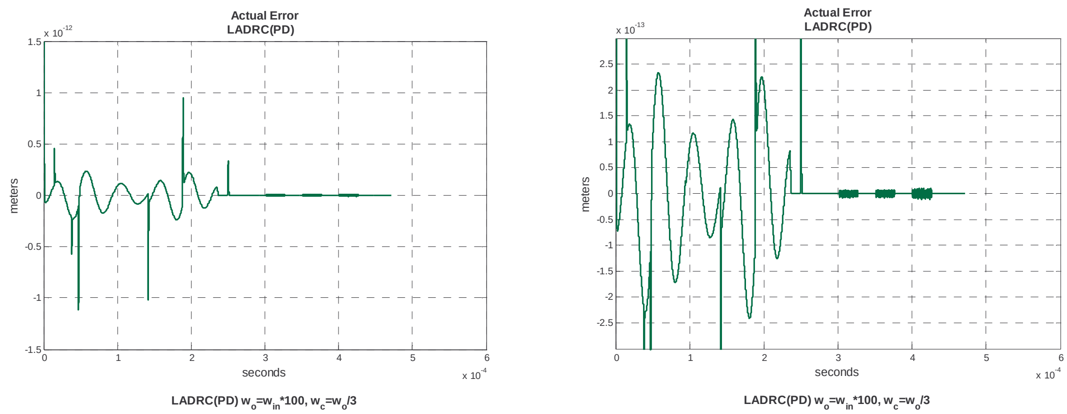

Figure 46 Position Error details, LADRC(PD), Recommended Observer Bandwidth

(LADRC with PD position control, observer frequency $\omega_o = 100\,\omega_{in,}\, \omega_c = 3\omega_o$*)*

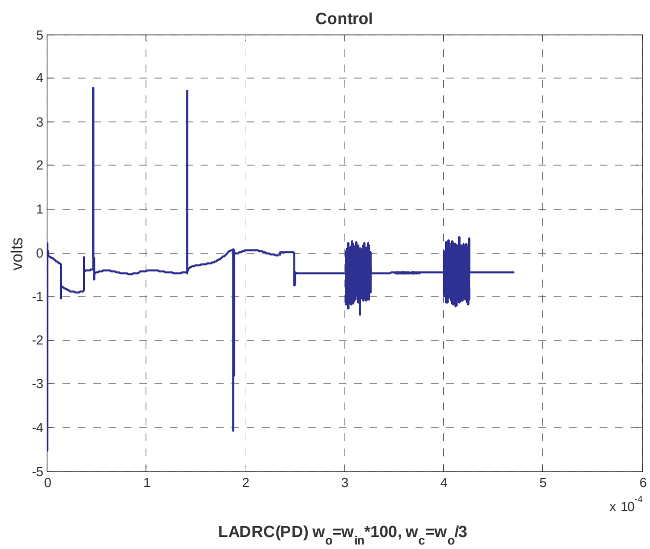

Figure 47 Control details, LADRC(PD), Recommended Observer Bandwidth

(LADRC with PD position control, observer frequency $\omega_o = 100\,\omega_{in,}\, \omega_c = 3\omega_o$*)*

The most obvious question that now arises is what benefits and costs accrue should one continue to increase the observer and controller bandwidth. The natural progression is another 10x increase:

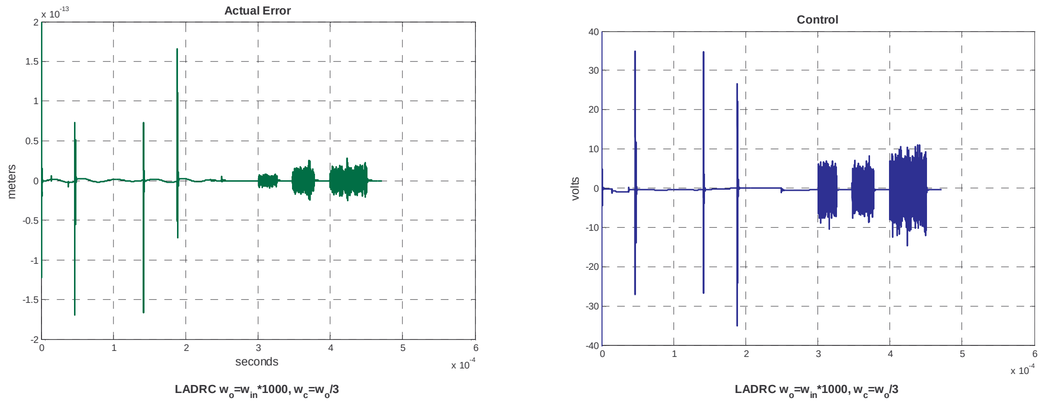

Figure 48   Error and Control detail, LADRC(PD), High Observer Bandwidth

(LADRC with PD position control, observer frequency $\omega_o = 1000\,\omega_{in}$)

The disturbance error at 0, 50, 140 and 190 μsec mentioned earlier is now even less in Figure 48, $\sim 2.3e^{-13}/1e^{-9} = .023\%$, which is excellent, due to the aggressive control. It is a concern the peak control signal (±35V) necessary to achieve this response is uncomfortably near the limits of the piezo device (±100V).

The nominal tracking error is $\sim 1e^{-14}/1e^{-9} = .001\%$. The error due to a 50% force disturbance during tracking or steady state is also $\sim 1e^{-14}m$. The response to input reference noise at 300 μsec, output measurement noise at 350 μsec and both at 400 μsec are notable as one raises the observer gain, as is obvious in comparison to the controller signal and error response for lower ω_o frequencies. The error from the input reference noise remains $\sim 1e^{-14}m$ in all observer frequency scenarios, which is to be expected. One will note immediately in these figures the tradeoff one must make for added accuracy and disturbance rejection versus measurement noise immunity and control.

5.5 A Hybrid Disturbance Rejection Strategy

The hybrid strategy builds on the ability of the ESO to accurately estimate the hysteresis nonlinearity in real time, and then the Han Function advantage to control the device to its natural anhysteretic response in minimal time with less peak drive energy. We shall refer to this as ADRC(Han). We will also simulate a reduced order LESO to estimate the unknown disturbances from a measurement of the output velocity rather than position, demonstrating the general nature of the solution to lower or higher order systems, and also how it may be utilized when direct measurement of an attribute might not be available or computation bandwidth is an issue.

5.5.1 ADRC with Han_1 velocity and Proportional position control

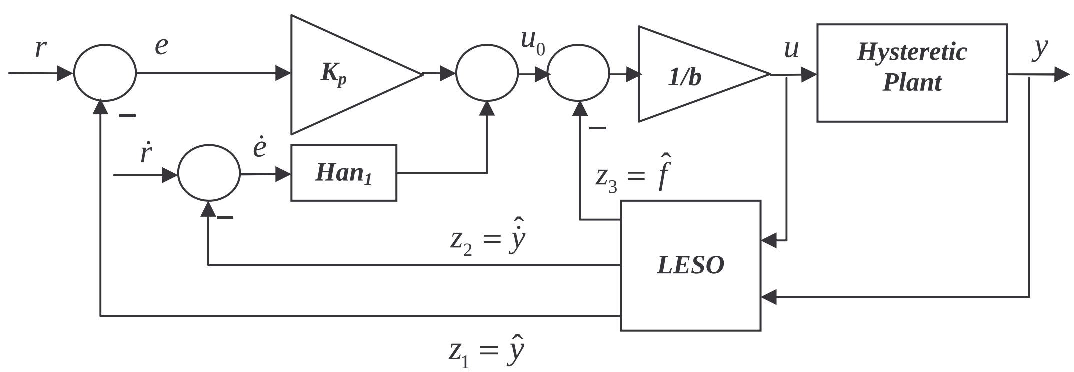

Figure 49 System Diagram, ADRC with Han_1 velocity and Proportional position control

The Han_1 Function for small signals in the Isochronic Region is a simple proportional gain. Therefore, when used in the velocity loop, appears as a linear derivative position control. Thus, a Han_1 Function velocity controller, in parallel with a proportional position control, appears as a PD position control. This is well understood to easily control the equivalent double integral plant from the LESO. The Han_1 Function, by its aggressive nature, will respond to error outside the IR faster than other control laws. One may tune the Han_1 with $K_h = 1e\text{-}7$, and set the proportional gain to $K_p = 1e^7$ to give an equivalent small signal PD control: $C(s) = -\dfrac{4e^{12}}{3}\left(s + 7.5e^{-6}\right)$.

The compensation for hysteresis nonlinearity in Figure 50 is as good as that for the LADRC with PD control. And all the while the control signal is less than that of other controls, due in great part to the aggressive response.

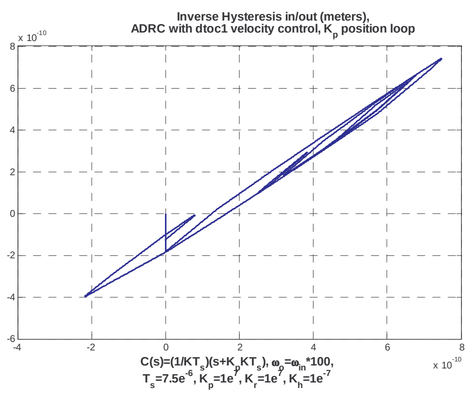

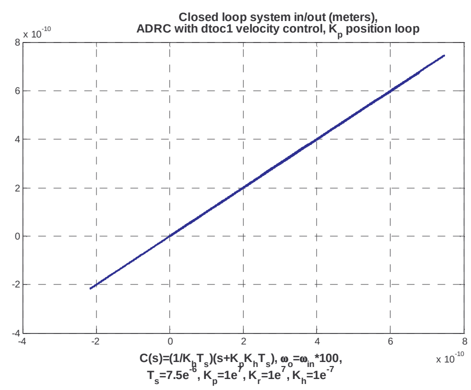

Figure 50 Hysteresis Disturbance before and after Compensation, ADRC + Han_1

(ADRC with Han_1 velocity control and proportional position control, observer frequency $\omega_o = 100\,\omega_{in}$)

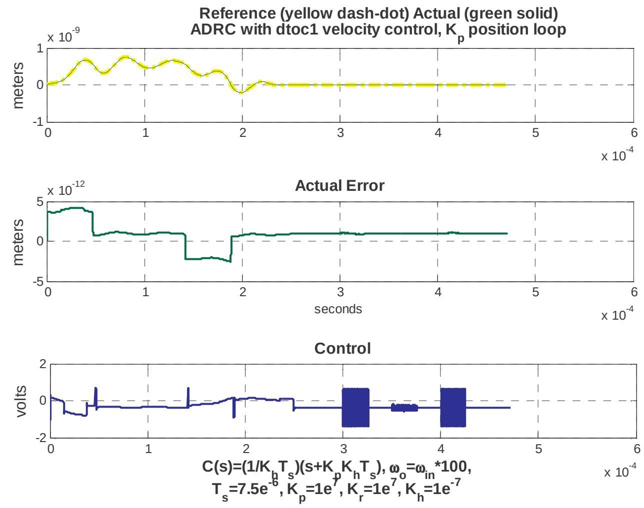

Figure 51 Position Error and Control, ADRC + Han_1

(ADRC with Han_1 velocity control and proportional position control, observer frequency $\omega_o = 100\omega_{in}$)

What one discovers from this tuning setting is that if one decreases gain K_h and/or reduces K_r one immediately observes the control will begin to leave the Isochronic Region for the Han_1 Function, and start cycling for short periods, the same results as for the Han_1 Function alone. The max error in Figure 51 during discontinuous inputs is $<4e^{-12}/1e^{-9} = .4\%$, which, to repeat, can be addressed by careful input profiling, but is still better than many other controllers reported in the literature. The tracking error is outstanding, $<4e^{-13}/1e^{-9} = .04\%$ and with input at the resonant frequency! The 50% disturbance rejection is also phenomenal, with error $<2.5e^{-13}/1e^{-9} = .025\%$. The noise error is excellent, with error from input noise $<3e^{-13}/1e^{-9} = .03\%$ and measurement noise error $<1e^{-14}/1e^{-9} = .001\%$. The most apparent error factor is the offset error $<1e^{-12}/1e^{-9} = .1\%$, which is a consequence of the size of the Han_1 Function Isochronic Region. The accuracy and disturbance rejection, not shown here, is proportional to the observer bandwidth, the same as for the Linear ADRC.

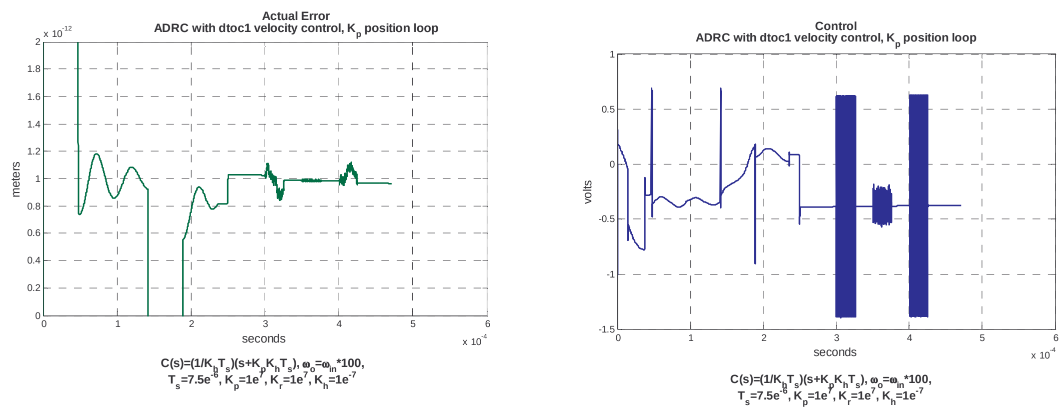

Figure 52 Error & Control Signal Details, ADRC + Han_1

(ADRC with Han_1 velocity control and proportional position control, observer frequency $\omega_o = 100\omega_{in}$)

5.5.2 The ADRC with Han_1 Function and reduced order LESO

This control is constructed as the previous, with the same design parameters, except the Linear Extended State Observer is not a 3rd order state observer with z_1 and z_2 for position and velocity respectively and the augmented state z_3 for the disturbance estimate, it is now a reduced 2nd order state observer for the velocity z_1, with the augmented disturbance estimate now z_2. This is possible because the hysteresis nonlinearity is internal to the device, and the integral relations between position and velocity and acceleration boundary conditions still hold. Thus the estimate of the disturbance and poorly modeled dynamics may be made via position OR velocity measures. The reduced state observer provides the same performance as that of the full state observer, all the measurements in Figure 53 and Figure 54 are equivalent, and the compensation for hysteresis is also excellent.

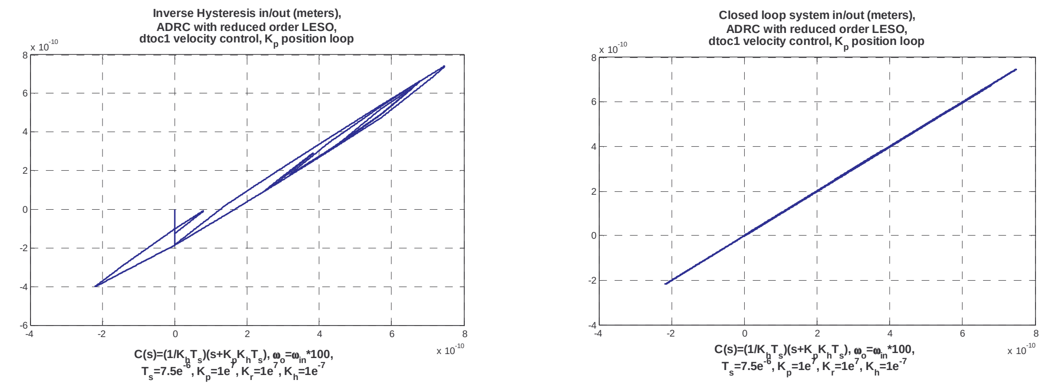

Figure 53 Hysteresis Disturbance before and after Compensation, Reduced order LESO

(ADRC with Han$_1$ velocity control and proportional position control, using a reduced order LESO to estimate hysteresis disturbance, observer frequency $\omega_o = 100\omega_{in}$)

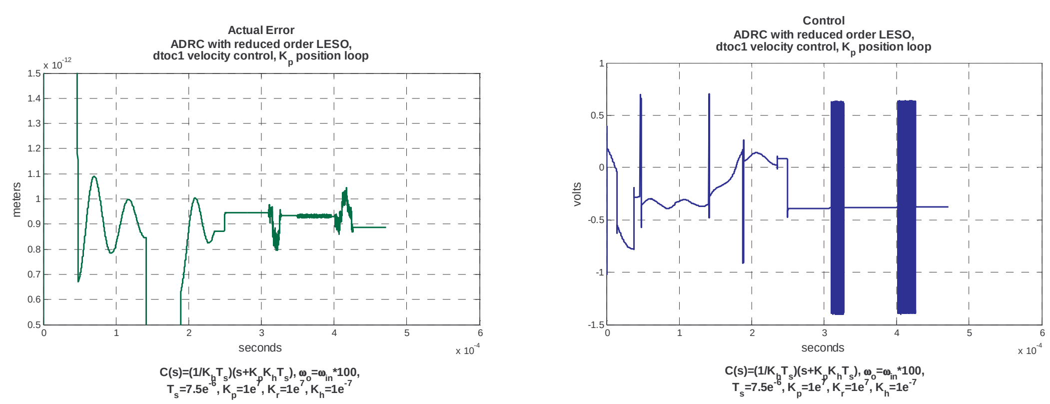

Figure 54 Error & Control Signal Details, Reduced order LESO

(ADRC with Han$_1$ velocity control and proportional position control, using a reduced order LESO to estimate hysteresis disturbance, observer frequency $\omega_o = 100\omega_{in}$)

5.6 Observations and Summary Regarding the Disturbance Rejection Paradigm

The performance of the disturbance rejection controls in the compensation of hysteresis is an order of magnitude superior to that previously reported in the literature. The bandwidth is wider, allowing operation to the mechanical limit of the device, and the accuracy during both tracking and regulation are superior. It is especially noteworthy the hysteresis nonlinearity, when treated as a disturbance, can be almost entirely compensated, without knowing anything about the character of that hysteresis. These results validate the efficacy of error based control and the advantages of measurement/estimation bandwidth versus modeling accuracy. The knowledge necessary to implement these controls are minimal, the steady state linear gain of the device is used for the LADRC design, along with some estimate of the natural bandwidth of the device as an initial tuning value, both readily gathered from data book information without any complexity or calibration. The Han Function control uses the saturation value for the control power signal and the sampling period of the hardware as initial tuning setting, which together can be easily parameterized. In both the control cases the tuning heuristic is easier to apply even than that of the popular PID control. This is a major advantage.

The rapid reaction of an inner velocity control loop combined with the aggressive Han_1 Function yielded performance that was particularly satisfying, as this is a wonderfully elegant solution using passive control technology. The inner velocity loop effectively compensated the hysteresis independent of any position control, delivering almost linear position response even when the position loop was left open, truly phenomenal and better than any other of the open loop model-based controls. This enabled one to choose any number of outer position loops for fine tuning the performance and aggressively rejecting external disturbance. The simple PI control was a natural choice and yielded excellent results an order of magnitude better than the best reported adaptive H_∞ control applied using a complex statistical based model. Even more gratifying is the fact all these Han Function controls were constrained to ±1V control signal and still delivered this performance, another testament to speed minimizing power requirements. Another advantage is the ability, even after compensating hysteresis, to reject external disturbances of 50% full load at < 0.03% error! If there is a caveat using the Han Function it would be the noise susceptibility, but since there was no noise rejection data from other published results there is little to compare, except to the LADRC, which was significantly better in this regard.

The performance result for the active disturbance rejection LADRC was best, as was expected from the beginning. The LADRC was easy to apply and the results improve proportional to the increase in the observer bandwidth. The limitation for the LADRC is the control signal magnitude one wishes to constrain. For our simulations we chose to go no further than ±4V, even though the power available was ±100V before saturating the device, it was simply not necessary to prove more. The accuracy of the LADRC is an order of magnitude better than the best model-based control even at these low signal levels. The strength of both types of disturbance rejection controls is the low energy and stress on equipment one achieves while still achieving better performance.

The hybrid combination of ADRC and Han_1 Function achieved results almost as good as the LADRC, and it is important to note the control energy was constrained. One would expect the performance is equal with equal power, but that was unfortunately not tested.

Another gratifying result is that for the reduced order ESO used to estimate and compensate for the hysteresis uncertainty, which may be useful for systems where the final position is unavailable. This result was expected as the hysteresis is internal to the device and the integral relationships between acceleration, velocity and position are maintained at the device boundary.

	Hysteresis Compensation	Disturbance Rejection	Tracking Error	Control Signal	Noise Error
LADRC	0.023%	0.03%	0.023%	±4V	0.001%
ADRC+Han_1+Prop	0.04%	0.025%	0.04%	±1V	0.001%
ADRC+Han_1+Prop reduced order ESO	0.04%	0.025%	0.04%	±1V	0.001%
Han_1+PI	0.05%	0.025%	0.05%	±1V	0.1%
Han_2+Han_1	0.5%	0.002%	0.5%	±1V	0.1%
Han_1Velocity Only	0.25%	0.15%	0.25%	±1V	

Figure 55 Performance Summary for Disturbance Rejection Control Strategies

CHAPTER 6

STABILITY ANALYSIS OF LADRC FOR A HYSTERETIC SYSTEM

The previous chapter exhibited the excellent and encouraging simulation results for LADRC control of a hysteretic system, this chapter considers the stability characteristics of LADRC for a hysteretic system. The BIBO stability of the LADRC for unknown bounded nonlinear function $\dot{f}$, in the system $\ddot{y} = f + bu$ has been previously demonstrated by Gao [38-40]. We will establish here that the piezo actuator system with hysteresis may be represented as such a system and will satisfy the assumptions given by Gao, thus showing stability for the hysteretic system.

We will establish in this chapter that for the hysteretic system $\ddot{y} = f + bu, where\ f = w - \frac{k_{eq}}{m}(I + P)^{-1}[y]$ in Equation (6.19) the sufficient conditions for BIBO stability of the LADRC closed loop solution are as follows:

- *The quasilinear model accurately describes the mechanical subsystem.*
- *The electrical dynamics are much faster than the mechanical dynamics.*
- *Functions of Preisach or Prandtl-Ishlinskii type are accurate Hysteresis models.*

- *The associated weighting function $\mu(r,s)$ or $\rho(r)$, and their derivative, for the hysteresis function model must be bounded.*
- *The reference input command r and $\dot{r}$ must be bounded.*
- *The input voltage creep has a scalar saturation limit V_{sat} and the function $\dot{V}_{creep}(t)$ is piecewise continuous bounded.*
- *The thermal drift coefficient functions $K_{vf}(t)$ and $\dot{K}_{vf}(t)$ are piecewise continuous bounded.*
- *Any external unknown disturbance $\dot{d}(t)$ is bounded.*

6.1 The BIBO Stability of LADRC

The general stability demonstration for the LADRC from Gao [38] will be included here for those unfamiliar. The LADRC strategy treats nonlinearities no different than any unknown disturbance. One can write the system equation:

$$\ddot{y} = f + bu \tag{6.1}$$

where *f* represents the total of one or more complex nonlinear, time varying processes and *bu* is the linear approximation for the plant. The central idea of LADRC is to let $\hat{f}$ be the estimate of *f* at time *t* and use the control law

$$u = \frac{u_0 - \hat{f}}{b} \tag{6.2}$$

to actively reject the general disturbance f and yield a plant which responds as $\ddot{y} \approx u_0$. This equivalent linear plant is easy to control.

The augmented state equation for (6.1) is:

$$\begin{aligned}
&\dot{x} = Ax + Bu + Eh \\
&y = Cx \\
&where\, x_1 = y,\ x_2 = \dot{y},\ x_3 = f,\ h = \dot{f}, \\
&A = \begin{bmatrix} 0 & 1 & 0 \\ 0 & 0 & 1 \\ 0 & 0 & 0 \end{bmatrix},\ B = \begin{bmatrix} 0 \\ b \\ 0 \end{bmatrix},\ C = \begin{bmatrix} 1 & 0 & 0 \end{bmatrix},\ E = \begin{bmatrix} 0 \\ 0 \\ 1 \end{bmatrix}
\end{aligned} \tag{6.3}$$

and the LESO is:

$$\begin{aligned}
&\dot{z} = Az + Bu + L(y - \hat{y}) \\
&\hat{y} = Cz \\
&where\, z_1 = \hat{y},\ z_2 = \hat{\dot{y}},\ z_3 = \hat{f},\ L = [\beta_1 \quad \beta_2 \quad \beta_3]^T
\end{aligned} \tag{6.4}$$

For the LADRC then the tracking error for the LESO observer, $\tilde{x} = x - z$, leads one to write the error equation as:

$$\begin{aligned}
&\dot{\tilde{x}} = \tilde{A}\tilde{x} + w,\ with \\
&\tilde{A} = A - LC = \begin{bmatrix} -\beta_1 & 1 & 0 \\ -\beta_2 & 0 & 1 \\ -\beta_3 & 0 & 0 \end{bmatrix},\ and\ w = Eh
\end{aligned} \tag{6.5}$$

where matrices *A, L, C,* and *E* are as in equations (6.3) and (6.4).

The first question presents itself, is the observer error, $\tilde{x}$, bounded?

<u>*Lemma 6.1: (Boundedness of the LESO error)*</u>

For any bounded h, assuming the observer gains $L = [\beta_1 \quad \beta_2 \quad \beta_3]^T$ *are chosen such that* $\tilde{A}$ *is Hurwit, the observer error,* $\tilde{x}$ *,is bounded.*

Proof: Let V be a Lyapunov function defined as

$$V = \tilde{x}^T P \tilde{x} \tag{6.6}$$

where P is the unique solution to the Lyapunov equation

$$\tilde{A}^T P + P\tilde{A} = -I \tag{6.7}$$

Then, per Lyapunov's first method,

$$\begin{aligned} \dot{V} &= -\tilde{x}^T \tilde{x} + 2w^T P\tilde{x} \\ &= -\left(\tilde{x}^T - w^T P\right)\left(\tilde{x}^T - w^T P\right)^T + \left(w^T P\right)\left(w^T P\right)^T \end{aligned} \tag{6.8}$$

Since

$$\left\|\tilde{x}^T - w^T P\right\|_2 > \left\|w^T P\right\|_2 \Rightarrow \left\|\tilde{x}^T\right\|_2 > 2\left\|w^T P\right\|_2 \Rightarrow \left\|\tilde{x}\right\|_2 > 2\left\|Pw\right\|_2 \tag{6.9}$$

Therefore $\dot{V} < 0$ *if* $\|\tilde{x}\|_2 > 2\|Pw\|_2$. *On the other hand, if h is bounded then w = Eh is bounded, and then* $\tilde{x}$ *is bounded as well since* $\dot{V} < 0$. ■

Lemma 6.1 can be generalized to a more general system:

$$\dot{\chi} = M\chi + \eta(\chi), \;\; M \in \mathbb{R}^{nxn}, \; \chi \in \mathbb{R}^n \tag{6.10}$$

which yields Lemma 6.2.

<u>Lemma 6.2:</u>

The state χ *in (6.10) is bounded if M is Hurwitz and* $\eta(\chi)$ *is bounded.* ■

Recalling (5.18) and (5.20) the goal for LADRC is such that $\ddot{y} \approx u_0$ which implies:

$$u = \frac{u_0 - z_3}{b} \tag{6.11}$$

$$u_0 = K_p(r - z_1) - K_d z_2 \tag{6.12}$$

Now we have the following Theorem.

Theorem 6.3: (BIBO stability of the LADRC)

The LADRC control law (6.11) utilizing the LESO (6.4) and the PD controller (6.12) yields a BIBO stable closed loop system if the LESO and the state feedback PD control are stable individually.

Proof: The observer error is bounded as proved in Lemma 6.1, so it remains to prove $\bar{x} = \begin{bmatrix} y \\ \dot{y} \end{bmatrix}$ *is bounded.*

$$\dot{\bar{x}} = \begin{bmatrix} 0 & 1 \\ -K_p & -K_d \end{bmatrix} \bar{x} + \begin{bmatrix} 0 & 0 & 0 & 0 \\ K_p & K_p & K_d & 1 \end{bmatrix} \begin{bmatrix} r \\ \tilde{x}_1 \\ \tilde{x}_2 \\ \tilde{x}_3 \end{bmatrix} = \bar{A}\bar{x} + \bar{B} \begin{bmatrix} r \\ \tilde{x} \end{bmatrix} \tag{6.13}$$

with a bounded reference r, as well as $\tilde{x}$ *bounded per Lemma 6.1, then choosing* K_p *and* K_d *such that* $\bar{A}$ *is Hurwitz assures BIBO stability per Lemma 6.2, which concludes the proof.* ■

6.2 The System Equation and Necessary Assumptions

We refer back to Figure 26 repeated here as Figure 56.

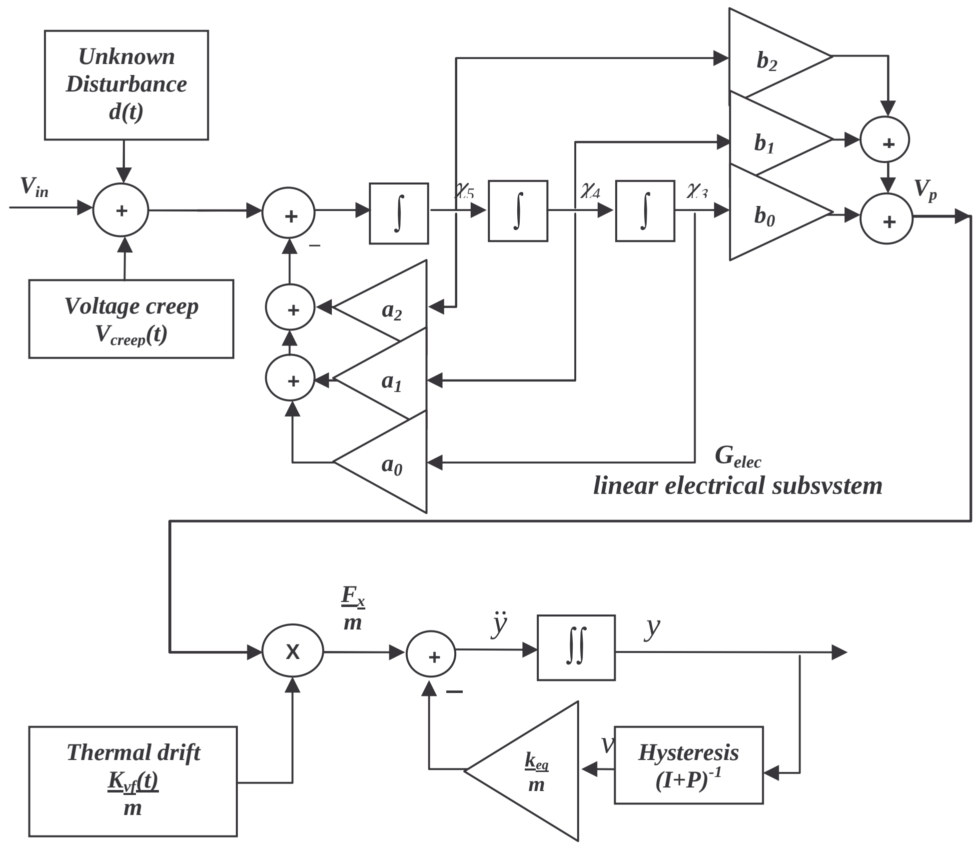

Figure 56 Complete piezo quasilinear model with hysteresis energy dissipation.

Some reasonable assumptions are necessary to make regarding the unknown disturbances and dynamics of this system in order to demonstrate BIBO stability for this system when controlled by LADRC. We will first analyze the thermal drift, voltage creep, the linear electrical subsystem and the external disturbance, and then the assumptions one must make to assure their bounded conditions. This allows one to illustrate a simplified model for the system which adheres to that used in Gao's LADRC stability proof. After this we can progress to an analysis of the conditions for bounded hysteretic behavior.

6.2.1 Assumptions for Bounded Thermal Drift

We assume $K_{vf}(t)$ and $\dot{K}_{vf}(t)$ are piecewise continuous bounded functions, so that the elements of $K_{vf}(t)$ and $\dot{K}_{vf}(t)$ are bounded. Hence $\left\|K_{vf}(t)\right\| \le k_1$ and $\left\|\dot{K}_{vf}(t)\right\| \le k_2$. Then

$$\begin{aligned}
&\left\|K_{vf}(t)(V_{p1}-V_{p2})\right\| \le \left\|K_{vf}(t)\right\|\left\|(V_{p1}-V_{p2})\right\| \le k_1\left\|(V_{p1}-V_{p2})\right\| \\
&\textit{and } \left\|\dot{K}_{vf}(t)(V_{p1}-V_{p2})\right\| \le \left\|\dot{K}_{vf}(t)\right\|\left\|(V_{p1}-V_{p2})\right\| \le k_2\left\|(V_{p1}-V_{p2})\right\| \\
&\textit{for any induced norms}
\end{aligned} \tag{6.14}$$

6.2.2 Assumptions for Bounded Voltage Creep

We review the definition of V_{creep} from Equation (4.49) and (4.50):

$$\begin{aligned}
&V_{sat} \in \mathbb{R}_+ \textit{ and } \lim_{V \to V_{sat}} f_{creep}(V) = 0 \\
&\textit{so that } \left\|V_{in}(t)\right\| := \max_{0 \le r < t}\left|V_{in}(r)\right| \le V_{sat}.
\end{aligned} \tag{6.15}$$

$$V_{creep}(t) := V_{in}(t)\, f_{creep}(V) \cdot t \tag{6.16}$$

What is sufficient for the BIBO stability of the LADRC is that the derivative of the voltage creep, $\dot{V}_{creep}(t)$, is bounded.

6.2.3 Assumption for Bounded Unknown Disturbance d(t)

The contribution of the unknown disturbance $d(t)$ and derivative $\dot{d}(t)$ are additive components of the acceleration force and is assumed bounded for our system.

6.2.4 Assumption for BIBO Stability and Separation of the Linear Electrical Subsystem

We review the Equation (4.32) for the electric subsystem

$$\dot{\chi} = \begin{bmatrix} 0 & 1 & 0 \\ 0 & 0 & 1 \\ -a_0 & -a_1 & -a_2 \end{bmatrix} \chi + \begin{bmatrix} 0 \\ 0 \\ 1 \end{bmatrix} V_{in}$$
$$V_p = \begin{bmatrix} b_0 & b_1 & b_2 \end{bmatrix} \chi \tag{6.17}$$

where a_0, a_1, a_2 *and* b_0, b_1, b_2 are positive numbers and A is Hurwitz. Consequently the electrical subsystem is itself asymptotically stable. Considering that all inputs to this asymptotically stable system are bounded, and that $\dot{V}_p$ is a linear combination of its internal states, then both V_p and $\dot{V}_p$ are bounded. We further assume the dynamics of the electrical subsystem are much faster than the mechanical subsystem and are subsequently disregarded in the analysis.

6.2.5 A Simplified Model for the Hysteretic System

Equation (4.51) is repeated here as Equation (6.18). (We have changed axis variable name from *x* to *y* in order to avoid confusion.)

$$\begin{aligned} \ddot{y} &= \frac{F_x}{m} - \frac{k_{eq}}{m}(I+P)^{-1}[y] \\ &= (w+bu) - \frac{k_{eq}}{m}(I+P)^{-1}[y] \\ &= f(y, w, (I+P)^{-1}) + bu \end{aligned} \tag{6.18}$$

where $b = K_{vf}^{0} / m$ and $u = V_{in}$ and w encompasses the unknown dynamics and disturbances. *Our task then is to demonstrate the function* $\dot{f}$ *for this hysteretic system is bounded.*

Based on the assumptions in 6.2.1-6.2.4, $\dot{w}$ can be readily shown to be bounded. What remains is to show that the hysteretic component of $\dot{f}$ is bounded.

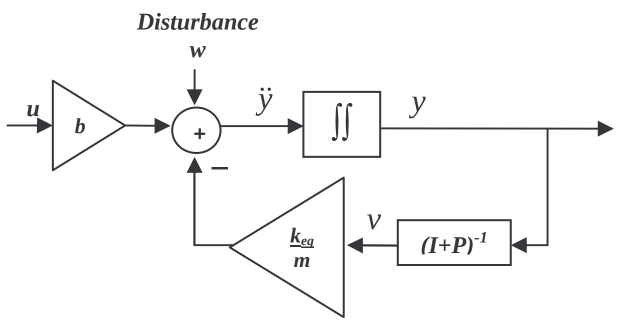

Figure 57 Simplified Piezo model with hysteresis.

$$\ddot{y} = f + bu, where\ f = w - \frac{k_{eq}}{m}(I+P)^{-1}[y] \tag{6.19}$$

6.3 Assumptions for Bounded Hysteresis Function $(I+P)^{-1}[y](t)$

One discerns in these nonlinear model equations the contribution of the hysteretic function $(I+P)^{-1}[y](t)$ in the complete motion equation function f, is *additive* to the other components of f. Therefore, due to the equivalence of function norms and the triangle inequality for norms, if one demonstrates the boundedness of $(I+P)^{-1}[y](t)$ *and* *its derivative*, then the motion function f and $\dot{f}$ are also bounded and Gao's BIBO stability analysis applies.

One can begin this process with an intuitive understanding for the outcome. The reader is referred to the hysteresis response curve Figure 58 and the signal v in the quasilinear mechanical model Figure 25 The difference for the linear relationship between output y_1 and the state v_1, is $\delta_1 > 0$, and the same for y_2, v_2 and $\delta_2 < 0$, where $(y,v) \in \Theta \subset \mathbb{R}^2$ are members of the major hysteresis loop region. These values are absolutely bounded by the maximum value of saturation for the device major loop, as shown by the solid diagonal lines, and become smaller as the device approaches the anhysteretic response. Thus one may understand the physical result of the energy dissipation and the accounting for it as the area encompassed by each hysteresis loop, as well as the bounded physical limitations of the response.

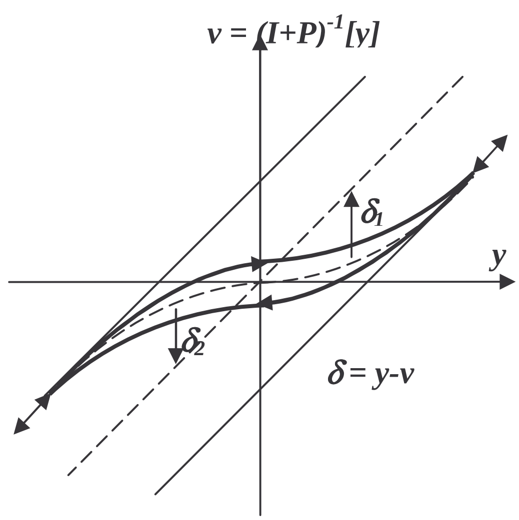

Figure 58 Inverse Hysteresis Function as a Disturbance from the Linear Response.

The stability analysis of conditions for a bounded hysteresis function used herein can be attributed to Brokate & Sprekels [10]. Similar analysis are available in Krejci [7677] and Visintin [127]. The minimal analysis, which is still lengthy, is included as Appendix C: Stability of Hysteresis and its Derivative, which includes Lemmas C1-C6 and Propositions C7-C8.

Lemma C.1-C.5 concern the Lipschitz continuity and assumptions for bounded behavior of the constituent "play" and "stop" basis operators. *Lemma C.6* then extends these conditions to the memory curve for the hysteresis function, and finally *Proposition C.7 and C.8* extend these properties to the Preisach and Prandtl-Ishlinskii hysteresis functions and derivatives, and delineate additional assumptions which must be made to show bounded behavior for the complete functions.

Lemmas C1-C6 and Propositions C7-C8 in Appendix C identify the conditions for a bounded hysteresis function *and their derivatives.* The conditions for bounded output for the hysteresis functions of Preisach $P[y](t)$ and Prandtl-Ishlinskii type $(I+P)^{-1}[y](t)$, *and their derivatives,* are that the input to the hysteresis function (*in our case the system output,* $y = \iint (f + bu)dt + y(0)$) be a piecewise continuous monotonic function. An additional requirement is that the associated weight functions, $\mu(r,s)$ and $\rho(r)$ used in the hysteresis function definition, *and their derivative*, must also be bounded. The piecewise continuous monotonic y output condition is consistent with the bounded condition on f and u , while the conditions on the hysteresis weights are new additions to our previous conditions.

Practically speaking, this is not an issue for the physical devices themselves, their "weighting" response will not be discontinuous as one operates throughout the range of the hysteretic device. Thus, as noted, the character of the weight functions in Equation (3.4) and (3.5) are an important enabling condition, and these bounded conditions have now been demonstrated to lead to bounded conditions for the hysteresis functions themselves. (This does place a continuity constraint on the method of weighting function interpolation for model-based discrete controller implementations, *a limitation we do not need to worry over*.)

6.4 Stability Conditions for the Hysteretic System with LADRC

The BIBO stability of the LADRC solution for the system $\ddot{y} = f + bu$ with unknown but bounded nonlinear functions $\dot{f}$ has been previously demonstrated by Gao [38]. In this chapter we analyzed and listed the assumptions needed to assure bounded behavior of $\dot{f}$ in our hysteretic system of Figure 25 The assumptions concern any unknown disturbances, voltage creep, thermal drift, and the hysteresis which constitute the functions $\dot{f}$.

For the hysteretic system $\ddot{y} = f + bu$ in Equation (6.19) the sufficient conditions for BIBO stability of the LADRC closed loop solution are as follows:

- *The quasilinear model accurately describes the mechanical subsystem.*
- *The electrical dynamics are much faster than the mechanical dynamics.*

- *Functions of Preisach or Prandtl-Ishlinskii type are accurate Hysteresis models.*
- *The associated weighting function $\mu(r,s)$ or $\rho(r)$, and their derivative, for the hysteresis function model must be bounded.*
- *The reference input command r and $\dot{r}$ must be bounded.*
- *The input voltage creep has a scalar saturation limit V_{sat} and the function $\dot{V}_{creep}(t)$ is piecewise continuous bounded.*
- *The thermal drift coefficient functions $K_{vf}(t)$ and $\dot{K}_{vf}(t)$ are piecewise continuous bounded.*
- *Any external unknown disturbance $\dot{d}(t)$ is bounded.*

A physically realizable system will usually possess these physical features assumed here. The assumptions regarding the models used are reasonable as they are proven representative of the experimental evidence, the Preisach and Prandtl-Ishlinskii models for hysteresis have been shown of high fidelity to actual experiment. Our experimentation is a component of the research which we emphasize in our recommendations for future work in the next chapter.

CHAPTER 7

SUMMARY, CONCLUSIONS AND FUTURE WORK

The challenge of nanometer scale positioning is a challenge in compensating for hysteresis. Positioning solutions at nanometer scale to this date have almost exclusively relied on a model-based control paradigm. Given the nature of hysteresis, and our purpose being compensating for the hysteresis rather than characterizing it, we hypothesized one could treat hysteresis as a disturbance to the desired linear response, much as one treats other unknown and unwanted disturbance. One could then compensate for hysteresis in a manner consistent with aggressive disturbance rejection, by either canceling its effect or aggressively driving the disturbance error to zero. The historical success using “dithering” as a hysteresis control method gave credence to this thesis. We therefore reformulated hysteresis compensation as a disturbance rejection problem and recomposed the system in an error-based disturbance rejection paradigm rather than the model-based paradigm.

Three hysteresis compensation strategies have been developed and validated using this disturbance rejection paradigm. A first strategy uses an active disturbance rejection control which estimates the disturbance in real time and cancels the error to the desired reference. A second passive disturbance rejection strategy utilizes the Han Function, a most aggressive closed form discrete time optimal control, to drive the disturbance error to its equilibrium zero state as quickly as possible. A third strategy combines the best features of both active and passive controls.

As nanometer scale systems are very expensive we have relied on a precise simulation of hysteretic devices to validate our proposed solutions. This has required the development of simulation models for these devices and construction of Matlab software modules. The control strategies have been tested and their superior performance confirmed using these simulations, thus validating the strategy.

Lastly, but quite important for future development, the LADRC, which demonstrated the best performance, has been proven BIBO stable for compensating hysteretic systems. The proof is general for hysteretic processes with some mild assumptions, but is not constrained to the specific piezo ceramic device used in our study, nor constrained to second order mechanical motion application. So it may be easily extended.

Future Work

The most compelling future effort would be a laboratory experimental validation for these results. Nanometer scale processes are not required as the most interesting outcome regards hysteresis compensation at any scale. In fact, a most exciting aspect of our result is the broad potential applicability in many fields. Ferromagnetics are constrained by hysteresis, as are phase change processes, chemical reactions, etc.

This breadth of this issue emphasizes the immediate application advantages to be realized by rapidly moving these strategies into common use.

One very intriguing idea came to mind during the research in hysteresis models. The models most used today are infinite sums and/or integrals of basis functions. It would be interesting to determine if a wavelet would provide advantages as a basis function for the hysteresis model, particularly if characterization was an issue as important as compensation.

REFERENCES

1. Adriaens, Han J. M. T. A., de Koning, Willem L., and Banning, Reinder, “Modeling Piezoelectric Actuator,” IEEE/ASME TRANSACTIONS ON MECHATRONICS, vol. 5, no. 4, DECEMBER 2000 pp331-341

2. Alexandrovitz, A. and Rootenberg, J., "Dithering as a factor in hysteresis elimination in rotating amplifiers," IEEE Trans. Automat. Contr., vol. 13, pp. 170 - 173, April 1968.

3. Ang W., Riviere C., and Khosla P., “Modeling Rate-dependent Hysteresis in Piezoelectric Actuator,” Proceedings of the 2003 IEEE/RSJ International Conference on Intelligent Robots and Systems, pp1975-1980, 2003.

4. Athans, M. and Falb, P., Optimal Control, McGraw-Hill Book Company, New York, 1966.

5. Berlincourt D. and Krueger H. H. A., revised by Near C., “Properties of Piezoelectricity Ceramics,” Morgan Electro Ceramics, Inc. Bedford, Ohio, USA, Technical Publication TP-226.

6. Binnig G., Quate C. F., Gerber Ch., “Atomic Force Microscope,” Phys. Rev. Lett. B 56(9), p930, 1986.

7. Binnig G., Rohrer H., Gerber C., Weibel E., “Scanning Tunneling Microscopy,” Helv. Phys. Acta 55, p726, 1982.

8. Binnig Gerd and Smith D. P. E., “Single-tube three-dimensional scanner for scanning tunneling microscopy,“ Rev. Sci. Instrum. 57(8), p1688, 1986.

9. Brokate, M., Pokrovskii, A. V., “Asymptotically stable oscillations in systems with hysteresis nonlinearities,” J. Differential Equations 150, pp98-123, 1998.

10. Brokate, M., Sprekels, J. “Hysteresis and phase transitions.” Appl. Math. Sci. Vol. 121. Springer-Verlag, New York, 1996.

11. Brokate, Martin and Krejci, Pavel, “Wellposedness of Kinematic Hardening Models in Elastoplasticity,” Mathematical Modeling and Numerical Analysis, Vol.32, No.2, pp177-209, 1998.

12. Bukofsky S. J., Selberg S. A., Grober R. D., Trautman J. K., “Application of near-field optics to critical dimension metrology,” Appl. Phys. Lett. 70 (18), p2368, 5 May 1997.

13. Butt Hans Jurgen, Jaschke Manfred, “Calculation of thermal noise in atomic force microscopy,” Nanotechnology 6, pp1, 1995.

14. Cady Walter Guyton, “Piezoelectricity,” McGraw Hill, NY, 1946.

15. Chang Timothy and Sun Xuemei, “Analysis and Control of Monolithic Piezoelectric Nano-Actuator,” IEEE Transactions on Control Systems Technology, 9(1), p69, January 2001.

16. Chen Ben M., Lee Tong H., Hang Chang-Chieh, Guo Yi, and Weerasooriya Siri, “An Almost Disturbance Decoupling Robust Controller Design for a Piezoelectric Bimorph Actuator with Hysteresis,” IEEE Transactions on Control Systems Technology, 7(2), p160, March 1999.

17. Chen C. Julian, “Electromechanical deflections of piezoelectric tubes with quartered electrodes,” Appl. Phys. Lett. 60 (I), p132, 6 January 1992

18. Chen C. Julian, “Introduction to Scanning Tunneling Microscopy,” Oxford University Press, NY, 1993

19. Choi S. B., Han S. S. and Lee Y. S., “Fine motion control of a moving stage using a piezoactuator associated with a displacement amplifier,” Smart Mater. Struct. 14(1), pp222–230, 2005.

20. Chu Larry L. and Gianchandani Yogesh B., “A micromachined 2D positioner with electrothermal actuation and sub-nanometer capacitive sensing,” J. Micromech. Microeng. 13, pp279–285, 2003.

21. Coleman, B. D., & Hodgdon, M. L., “A constitutive relation for rate-independent hysteresis in ferromagnetically soft materials,” International Journal of Engineering Science, 24 (6), pp897-919, 1986

22. Croft D., Shedd D., Devasia S., “Creep, Hysteresis, and Vibration Compensation for Piezoactuators: Atomic Force Microscopy Application,” Proc. Amer. Control Conf. 2000, p2123.

23. Cruz-Hernández Juan Manuel, and Hayward Vincent, “Phase Control Approach to Hysteresis Reduction,” IEEE Transactions on Control Systems Technology, 9(1), p17, January 2001.

24. Cummings Jeremy Ronald (Dr. Richard Superfine, advisor), “Development and Applications of Magneto-Optical Scanning Probe Microscopy,” Doctoral Dissertation, University of North Carolina at Chapel Hill, 2001.

25. Curie J., J. Phys. 8, p149, Paris, 1889.

26. Daniele A., Salapaka S., Salapaka M.V., and Dahleh M., “Piezoelectric Scanners for Atomic Force Microscopes: Design of Lateral Sensors, Identification and Control,” Proceedings of the American Control Conference, pp253, l June 1999.

27. Della Torre, E. “Effect of interaction on the magnetization of single-domain particles,” I.E.E.E. Trans. on Audio. Vol.14, pp86-93, 1966.

28. Desch, W., “Local Lipschitz continuity of the stop operator,” Appl. Math. Vol. 43, pp461–477, 1998

29. Desch, Wolfgang and Turi, Janos, “The Stop Operator Related to a Convex Polyhedron,” Journal of Differential Equations vol.157, pp329-347, 1999.

30. Duhem, P., “Die dauernden Anderungen und die Thermodynamik I-IX,” Z. Phys. Chemie. vol 22 pp 543-589, vol 23 pp 193-266, vol 23 pp 497-541, vol 28 pp 577-618, vol 33 pp 641-697, vol 34 pp 312-377, vol 34 pp 683-700, vol 37 pp 91-99, vol 43 pp 695-700, 1897-1903.

31. Egawa A., Chiba N., Homma K., Chinone K. & Muramatsu H., “High-speed scanning by dual feedback control in SNOM/AFM,” Journal of Microscopy, Vol. 194, Pt 2/3, pp325-328, May/June 1999.

32. Fukuma Takeshi, Kimura Kenjiro, Kobayashi Kei, Matsushige Kazumi and Yamada Hirofumi, “Dynamic force microscopy at high cantilever resonance frequencies using heterodyne optical beam deflection method,” Appl. Phys. Lett. 85 (25), p6287, 20 December 2004.

33. Furutani Katsushi, Urushibata Mitsunori and Mohri Naotake, “Displacement control of piezoelectric element by feedback of induced charge,” Nanotechnology 9(2), pp93, 1998.

34. Furutani, Katsushi, Suzuki, Michio and Kudoh, Ryusei, “Nanometre-cutting machine using a Stewart-platform parallel mechanism,” Meas. Sci. Technol. 15, pp467–474, 2004.

35. Gao, Z., Huang, Y. and Han, J., “An Alternative Paradigm for Control System Design,” Proc. Of the 40th IEEE Conference on Decision and Control, Orlando, Florida USA, December 2001, pp: 4578-4585.

36. Gao, Z., Hu, S. and Jiang, F., “A Novel Motion Control Design Approach Based on Active Disturbance Rejection,” Proc. of the 40th IEEE Conference on Decision and Control, Dec 4-7, 2001, Orlando, Florida.

37. Gao, Zhiqiang, “On Discrete Time Optimal Control: A Closed-Form Solution,” Proc. of the 2004 American Control Conference, June 2004

38. Gao, Zhiqiang, “Active Disturbance Rejection Control: A Paradigm Shift in Feedback Control System Design,” Proceeding of the 2006 American Control Conference, June 2006, to be presented

39. Gao, Zhiqiang, “From Linear to Nonlinear Control Means: A Practical Progression,” ISA Transactions, vol.41, no.2 p. 177-89, April 2002.

40. Gao, Zhiqiang, “Scaling and Parameterization Based Controller Tuning,” Proc. of the 2003 American Control Conference, pp. 4989-4996, June 2003.

41. Ge P. and Jouaneh M., “Tracking control of a Piezoceramic actuator,” IEEE Trans. Contr. Syst. Technol., vol. 4, no. 3, pp. 209–216, May 1996.

42. Ge, P. and Jouaneh, M., "Modeling hysteresis in piezoceramic actuators," Precision Eng., vol 17, pp. 211-221, 1995.

43. Goforth, F. “On Motion Control Design and Tuning Techniques,” Proc. of the 2004 American Control Conference, Boston, June 30 to July 2, 2004.

44. Goldfarb Michael and Celanovic Nikola, “Modeling Piezoelectric Stack Actuators for Control of Micromanipulation,” Contr. Syst. Mag., vol. 17, p69, June 1997.

45. Gonda S., Doi T., Kurosawa T., Tanimura Y., Hisata N., Yamagishi T., Fujimoto H., Yukawa H., “Accurate topographic images using a measuring atomic force microscope,” Applied Surface Science 144–145, pp505–509, 1999.

46. Hadjiiski L., Munster S., Oesterschulze E., and Kassing R., “Neural network correction of nonlinearities in scanning probe microscope images,” J. Vac. Sci. Technol. B 14 (2), p1563, Mar/Apr 1996

47. Hall D. A., “Review, Nonlinearity in piezoelectric ceramics,” Journal of Materials Science 36 (19), p4575, 2001.

48. Han, J. “Auto-Disturbance Rejection Control and its Applications,” Control and Decision, Vol.13, No.1, 1998.(In Chinese)

49. Han, J. “Nonlinear Design Methods for Control Systems,” Proc. Of the 14th IFAC World Congress, Beijing, 1999.

50. Han, J. and Wang, W., “Nonlinear Tracking Differentiator,” Systems Sciences and Mathematical Sciences, vol.14, no.2, pp177-183, 1994. (In Chinese)

51. Han, J. and Yuan, L., “The Discrete Form of the Tracking Differentiator,” Systems Sciences and Mathematical Sciences, vol.19, no.3, pp268-273, 1999. (In Chinese)

52. Hansma P. K., Drake B., Grigg D., Prater C. B., Yashar F., Gurley G., Elings V., Feinstein S., Lal R., “A new, optical-lever based atomic force microscope,” J. Appl. Phys. 76 (2), pp796, 15 July 1994

53. Hatch Andrew G., Smith Ralph C. and De Tathagata, “Model Development and Control Design for High Speed Atomic Force Microscopy,” CRSC-TR04-17, April, 2004.

54. Heyde Markus, Heinz Sturm and Rademann Klaus, “ New Application for the Calibration of Scanning Probe Microscopy Piezos, “ Surf. Interface Anal. 27, pp291, 1999.

55. Hicks T. R. and Atherton P. D., “The NanoPostitioning Book,” Queensgate Instruments Ltd., Waterside Park, Berkshire, UK, 1997.

56. Holman A. E., Scholte P. M. L. 0., Heerens W. Chr., and Tuinstra F., “Analysis of piezo actuators in translation constructions,” Rev. Sci. Instrum. 66 (5), p3208, May 1995.

57. Hu, H., Mrad, R. Ben, “A discrete-time compensation algorithm for hysteresis in piezoceramic actuators,” Mechanical Systems and Signal Processing 18 (1), pp169–185, 2004.

58. Hu, S. “On High Performance Servo Control Solutions for Hard Disk Drive,” Doctoral Dissertation, Department of Electrical and Computer Engineering, Cleveland State University, April 27, 2001.

59. Huang, Y., Xu, K. and Han, J. “Flight Control Design Using Extended State Observer and Non-smooth Feedback,” Proc. of the 40th IEEE Conference on Decision and Control, Dec 4-7, 2001, Orlando, Florida.

60. Hwang Chih-Lyang, Chen Yung-Ming, Jan Chau, “Trajectory Tracking of Large-Displacement Piezoelectric Actuators Using a Nonlinear Observer-Based Variable Structure Control,” IEEE Transactions on Control Systems Technology, 13(1), p56, January 2005.

61. Ishlin’skii, A.Yu., “Some applications of statistical methods to describing deformations of bodies” (in Russian), Izv. Akad. Nauk SSSR, Tech. Ser. 9 (1944) 580–590.

62. Jaffe B., Cook W. R., Jaffe H. L., “Piezoelectric Ceramics,” Academic Press, New York, 1971.

63. Jung, Hewon, Shim, Jong Youp and Gweon, DaeGab, “Tracking control of piezoelectric actuators,” Nanotechnology 12 (1), pp14–20, 2000.

64. Kawakatsu H., Hoshi Y., Bleuler H., Kougami H., Bossardt M., Vezzin N. “Two-dimensional positioning of the scanning tunneling microscope stage using a crystal as a scale reference,” Appl. Phys. A 66(7), ppS853–S855, 1998.

65. Khalil Hassan K., “Nonlinear Systems, 3ed,” Prentice Hall, Upper Saddle River, NJ, 2002.

66. Klein, Olaf and Krejci, Pavel, “Outwards pointing hysteresis operators and asymptotic behaviour of evolution equations,” Nonlinear Analysis: Real World Applications vol.4 pp755-785, 2003.

67. Kokotovic Petar, Khalil Hassan K., and O’Reilly John, “Singular Perturbation Methods in Control, Analysis and Design,” Academic Press, London, 1986.

68. Koops K.R., Banning R., Scholte P.M.L.O., Heerens W. Chr., Adriaens J.M.T.A., de Koning W.L., “Design and construction of a high-resolution 3D translation stage for metrological applications,” Appl. Phys. A 66(7), ppS857–S860, 1998.

69. Koops K.R., Scholte P.M.L.O., de Koning W.L., “Observation of zero creep in piezoelectric actuators,” Appl. Phys. A 68, pp691–697, 1999.

70. Krasnosel’skii, M. A. and Pokrov’skii, A. V., “Systems with Hysteresis,” English translation: Springer 1989, Russian: Nauka, Moscow, 1983.

71. Krejci, P. “Global behaviour of solutions to the wave equation with hysteresis,” Adv. Math. Sci. Appl. vol.2, pp1-23, 1993.

72. Krejci, P. and Kuhnen, K., “Inverse control of systems with hysteresis and creep,” IEE Proc. Control Theory Applic. vol.148, pp185–192, 2001.

73. Krejci, P., “Hysteresis and periodic solutions of semilinear and quasilinear wave equations,” Math. Z. vol.193, pp247–264, 1986.

74. Krejcı, P., “Hysteresis in Singularly Perturbed Problems,” Singular Perturbation and Hysteresis, ed M. P. Mortell et al, SIAM, Philadelphia, 2005.

75. Krejci, Pavel, “Forced Oscillations in Preisach Systems,” Physica B, vol.275, pp81-86, 2000.

76. Krejci, Pavel, “Hysteresis, Convexity and Dissipation in Hyperbolic Equations,” Gakuto Int. Ser. Math. Sci. Appl., Vol 8. Gakkotosho, Tokyo, 1996.

77. Krejci, Pavel, “Resonance in Preisach Systems,” Applications of Mathematics, vol.45, no.6, pp439-468, 2000.

78. Ku Sang-Soon, Pinsopon Unnat, Cetinkunt Sabri, and Nakajima Shin-ichi, “Design, Fabrication, and Real-Time Neural Network Control of a Three-Degrees-of-Freedom Nanopositioner,” IEEE/ASME Transactions on Mechatronics, 5(3), p273, September 2000.

79. Kuhnen, K., Janocha, H., “Operator-based compensation of hysteresis, creep and force-dependence of piezoelectric actuators,” Proceedings of the 1st IFAC Conference on Mechatronic Systems, Darmstadt, pp.421–426, September 2000.

80. Leang, Kam K. and Devasia, Santosh, “Iterative Feedforward Compensation of Hysteresis in Piezo Positioners,” Proceedings of the 42nd IEEE Conference on Decision and Control, pp2626, 2003.

81. Lecoq, L. P. and Hopkin, A. M., "A functional analysis approach to $L\infty$ stability and its applications to systems with hysteresis," IEEE Trans. Automat. Contr., vol. 17, pp. 328 - 338, June 1972.

82. Li Chun-Tao and Tan Yong-Hong, “Adaptive Output Feedback Control of Systems Preceded by the Preisach-Type Hysteresis,” IEEE Transactions on Systems, Man, and Cybernetics—Part B: Cybernetics, 35(1), p130, February 2005.

83. Liu Hongzhong, Lu Bingheng, Ding Yucheng, Tang Yiping and Li Dichen, “A motor-piezo actuator for nano-scale positioning based on dual servo loop and nonlinearity compensation,” J. Micromech. Microeng. 13, pp 295–299, 2003.

84. Liu, Jing, “Comparative Study of Differentiation And Integration Techniques For Feedback Control Systems,” Masters Thesis, Cleveland State University, 2002, Zhiqiang Gao advisor

85. Locatelli M., Lamboley G., Michenaud J.P., Bayot V., “Easy Method to Characterize a Piezoelectric Ceramic Tube as a Displacer,” Rev. Sci. Instrum. 59(4), p661, 1988.

86. Mason W. P. and Jaffe H., “Methods for Measuring Piezoelectric, Elastic, and Dielectric Coefficients of Crystals and Ceramics,” Proceedings of the IRE, 42, pp921-930, 1954.

87. Mason Warren P., “Piezoelectric crystals and their application to Ultrasonics,” D. Van Nostrand, Princeton, NJ, 1950.

88. Maxwell J.C., “A treatise on electricity and magnetism,” Clarendon Press, Oxford, 1873.

89. Mayergoyz I. D., “Hysteresis models from the mathematical and control theory point of view,” J. Appl. Phys. 57 (1), p3803, 1985.

90. Mayergoyz I. D., “Vector Preisach hysteresis models (invited),” J. Appl. Phys. 63 (8), p2995, 1988.

91. Mayergoyz Isaak, “Mathematical Models of Hysteresis and their Applications,” Academic Press, New York, 2003.

92. Meli F. and Thalmann R., “Long-range AFM profiler used for accurate pitch measurements,” Meas. Sci. Technol. 9 pp1087–1092, 1998.

93. Meyer Gerhard and Amer Nabil M., “Novel optical approach to atomic force microscopy,” Appl. Phys. Lett. 53 (12), pp1045, 1988

94. Miklosovic, R. and Gao, Z. "A Dynamic Decoupling Method for Controlling High Performance Turbofan Engines", Proceedings of 2005 IFAC World Congress, Prague, July, 2005.

95. Minorsky, N., “Directional Stability and Automatically Steered Bodies,” J. Am. Soc. Nav. Eng., vol. 34, p.280, 1922.

96. Mittal Samir and Menq Chia-Hsiang, “Hysteresis Compensation in Electromagnetic Actuators Through Preisach Model Inversion,” IEEE/ASME Transactions on Mechatronics, 5 (4), p394, December 2000.

97. Mokaberi B. and Requicha A. A. G., “Towards Automatic Nanomanipulation: Drift Compensation in Scanning Probe Microscopes,” Proc. 2004 IEEE International Conference on Robotics and Automation, p416.

98. Picotto G. B. and Desogus S., Lanyi S., Nerino R. and Sosso A., “Scanning tunneling microscopy head having integrated capacitive sensors for calibration of scanner displacements,” J. Vac. Sci. Technol. B 14(2), pp897, Mar/Apr 1996.

99. Pontryagin, L.S., Boltyanskii, V.G., Gamkrelidze, R.V. and Mishchenko, E.F. “The Mathematical Theory of Optimal Processes,” Inter-Science Publishers, Inc. New York, 1962.

100. Prandtl Ludwig, “Ein Gedankenmodell zur kinetischen Theorie der festen Korper,” Z. Angew. Math. Mech. 8 , pp85-106, 1928.

101. Prandtl, Ludwig, “Spannungverteilung in plastischen Korpern,” Proc. 1st Intern. Congr. Appl. Mech., Delft, pp43-54, 1924.

102. Preisach, Ferenc, “Uber die magnetische Nachwirkung, Z. Physik, 94, pp277-302, 1935.

103. Requicha, A. A., Meltzer, G. S., Terán Arce, F. P., Makaliwe, J. H., Sikén, H., Hsieh, S., Lewis, D., Koel, B. E. and Thompson, M. E., “Manipulation of Nanoscale Components with the AFM: Principles and Applications,” 2003 Proceedings of IEEE Special Issue on Nanoelectronics, pp .

104. Richter, H., Misawa, E. A., Lucca, D. A. and Lu, H., “Modeling nonlinear behavior in a piezoelectric actuator,” Journal of the International Societies for Precision Engineering and Nanotechnology, 25 (1), pp128-137, 2001.

105. Rugar, D., Mamin, H. J., Guethner, P., “Improved fiber-optic interferometer for atomic force microscopy,” Appl. Phys. Lett. 55 (25), pp2588, 1989

106. Schaffer, Tilman E., “Calculation of thermal noise in an atomic force microscope with a finite optical spot size,” Nanotechnology 16, pp664–670, 2005.

107. Schitter, G. and Stemmer, A., “Eliminating mechanical perturbations in scanning probe microscopy,” Nanotechnology 13(5), pp663–665, 2002.

108. Schitter, G., Allgower, F. and Stemmer, A., “A new control strategy for high-speed atomic force microscopy,” Nanotechnology 15, pp108–114, 2004.

109. Schitter, G., Menold, P., Knapp, H. F., Allgower, F., Stemmer A., “High performance feedback for fast scanning atomic force microscopes,” Rev. Sci. Inst. 72(8), p3320, August 2001.

110. Schitter, G., Stark, R. W. and Stemmer, A., “Sensors for closed-loop piezo control: strain gauges versus optical sensors,” Meas. Sci. Technol. 13 ppN47–N48, 2002.

111. Schitter, G., Stark, R.W., Stemmer, A., “Fast contact-mode atomic force microscopy on biological specimen by model-based control,” Ultramicroscopy 100(3), pp253–257, 2004.

112. Schitter, G., Stemmer, A., “Model-based signal conditioning for high-speed atomic force and friction force microscopy,” Microelectronic Engineering 67, pp938–944, 2003.

113. Schitter, Georg and Stemmer, Andreas, “Fast closed loop control of piezoelectric transducers, “ J. Vac. Sci. Technol. B 20(1), p350, Jan’Feb 2002.

114. Schitter, Georg and Stemmer, Andreas, “Identification and Open-Loop Tracking Control of a Piezoelectric Tube Scanner for High-Speed Scanning-Probe Microscopy,” IEEE Transactions on Control Systems Technology, 12(3), p449, May 2004.

115. Shahruz, Shahram Mojaddad, Studies of multiple-time-scale phenomena in control systems,” Doctoral Dissertation, U. California at Berkeley, 1988, Charles Desoer advisor.

116. Smith, W. F. and Axelrod, B. W., “Measurements of the double piezoelectric effect,” Rev. Sci. Instrum. 71 (4), p1772, 4 APRIL 2000.

117. Stark, Robert W., “Optical lever detection in higher eigenmode dynamic atomic force microscopy,” Rev. Sci. Inst. 75 (11), p5053, November 2004.

118. Sun, Jian; and Hang, King-Ching, “Analysis and Synthesis of Time Optimal Control Systems,” Proc. Of the Second IFAC Congress, Basel, 1963.

119. Sun, Jian; Hang, King-Ching; and Tang, Zhiqiang, “Time Optimal Control Synthesis for Linear Time InvariantSystems with Discontinuities,” Proc. Of the Conference of Ordinary Differential Equations, Beijing, 1965.

120. Takacs, Jeno, “Mathematics of Hysteretic Phenomena, the T(x) Model for the Description of Hysteresis,” Wiley-VCH, Weinheim, 2003.

121. Tamer, Nabil, Dahleh, Mohammad, “Feedback Control of Piezoelectric Tube Scanners,” Proceedings of 33rd Conference on Decision and Control, p1826, 1994.

122. Tao, G. and Kokotovic, P. V., "Adaptive control of plants with unknown hysteresis," IEEE Trans. Automat. Contr., vol. 40, pp. 200 - 212, February 1995.

123. Tao, Gang and Kokotovic, Petar, “Adaptive Control of Systems with Actuator and Sensor Nonlinearities,” John Wiley & Sons, New York, 1996.

124. Timoshenko, S., Young, D. H. and Weaver, W. Jr., “Vibration Problems in Engineering, 4th ed.” John Wiley & Sons, New York, 1974.

125. Vieira, S., “The behavior and characterization of some piezoelectric ceramics used in the STM,” IBM J. Res. Dev. 30, p553 1986.

126. Visintin, Augusto, “Quasilinear Hyperbolic Equations with Hysteresis,” Ann. I. H. Poincaré – AN 19, no.4 pp451–476, 2002.

127. Visitin, Augusto, “Differential Models of Hysteresis,” Springer-Verlag, Berlin, 1994.

128. Weisenhorn, A. L., Hansma P. K., Albrecht T. R., Quate C. F., “Forces in atomic force microscopy in air and water,” Appl. Phys. Lett. 54 (26), pp2651, 1989

129. Yang, Jiashi, “An Introduction to the Theory of Piezoelectricity,” Springer Science, NY, 2005.

130. Ziegler, J.G. and Nichols, N.B., “Optimal Settings for Automatic Controllers”, Trans. ASME, vol 64, pp759-768, 1942.

131. Zou, Qingze and Devasia, Santosh, “Preview-Based Optimal Inversion for Output Tracking: Application to Scanning Tunneling Microscopy,” IEEE Transactions on Control Systems Technology, 12(3), p375, MAY 2004.

APPENDICES

APPENDIX A: HYSTERESIS SIMULATION M-FILES

Code listing for “norm_load_xx…” which contains the piezo first order transition curve data used in the hysteresis simulation and inverse simulation. This m-file is run before the simulations.

```
% Hysteresis simulation parameters:
% this implementation is based on the "classical" preisach model for
% hysteresis found in section 1.4 of "Mathematical Models of Hysteresis
% and Their Applications" 2ed, by Isaak D. Mayergoyz, Elsevier Science,
% Amsterdam, 2003

% the implementation is called "norm_preisach_xx..."
% and calls an interpolation function "norm_intp_xx..." which is
% linear in both alpha and beta directions and uses a set of normalized
% mesh values "norm_f" for the first order transition curves. "norm_f"
% may be loaded as part of "norm_intp_xx" or loaded in
% "norm_load_xx..."


% the inverse of the hysteresis is also a preisach operator calculated
% the same method only using a different set of first order reversal
% curves for the device which are clockwise. the implementation is
% called "norm_preisach_inv_xx..." and calls the same interpolation
% routine, but uses the "norm_f_inv" first order transition curve data.

global u_pre_hys num_alpha_hys num_beta_hys u_dir_be_hys ...
u_dir_temp_hys u_dir_cu_hys
global alpha_hys beta_hys alpha0_hys beta0_hys slope_hys ...
new_f_hys new_a_hys new_b_hys
global u_pre_hys_inv num_alpha_hys_inv num_beta_hys_inv ...
u_dir_be_hys_inv u_dir_temp_hys_inv u_dir_cu_hys_inv
global alpha_hys_inv beta_hys_inv alpha0_hys_inv beta0_hys_inv ...
slope_hys_inv new_f_hys_inv new_a_hys_inv new_b_hys_inv

% alpha0 and beta0 are the upper and lower limits of the half plane
% triangle "T" of book section 1.2. they are parameters for the
% function.
alpha0_hys =1; % 2.1; % this is the upper hysteresis limit
alpha0_hys_out =1; % 2.1; % this is the output at upper limit
beta0_hys =-1; % 0; % this is the lower hysteresis limit
beta0_hys_out =-1; % 0; % this is the output at lower limit
alpha0_hys_inv =1; % 2.1; % this is the upper hysteresis limit
alpha0_hys_out_inv =1; % 2.1; % this is the output at upper limit
beta0_hys_inv =-1; % 0; % this is the lower hysteresis limit
beta0_hys_out_inv =-1; % 0; % this is the output at lower limit

u_pre_hys=0; num_alpha_hys=0; num_beta_hys=0; u_dir_be_hys=0;
u_dir_temp_hys=0; u_dir_cu_hys=0; alpha_hys=0; beta_hys=0;

u_pre_hys_inv=0; num_alpha_hys_inv=0; num_beta_hys_inv=0;
u_dir_be_hys_inv=0; u_dir_temp_hys_inv=0; u_dir_cu_hys_inv=0;
alpha_hys_inv=0; beta_hys_inv=0;
```

```
%-------------------------------------------------------------------
    % norm_f, norm_a and norm_b are used as global
    % Based on a linear spline interpolation function, a displacement
    % value is computed with the information of alpha and beta.

norm_a=[1:-1/20:0]; norm_b=[0:1/20:1];
% norm_a and norm_b are the region of alpha and beta, respectively.
% norm_f shows displacement values with respect to alpha and beta axes.
% this norm_f is from piezo data and does not saturate at limits
norm_f = [
0, 0.074, 0.141, 0.206, 0.268, 0.329, 0.387, 0.444, 0.5, 0.553,...
0.605, 0.654, 0.7, 0.747, 0.79, 0.833, 0.873, 0.911, 0.946,...
0.979, 1;...
0, 0.073, 0.139, 0.203, 0.264, 0.324, 0.382, 0.438, 0.492, 0.545,...
0.595, 0.643, 0.69, 0.735, 0.777, 0.817, 0.855, 0.89, 0.923,...
0.947, 0;...
0, 0.072, 0.137, 0.199, 0.26, 0.318, 0.375, 0.431, 0.484, 0.534,...
0.584, 0.631, 0.676, 0.719, 0.76, 0.798, 0.833, 0.866, 0.889, 0, 0;...
0, 0.07, 0.134, 0.195, 0.255, 0.313, 0.369, 0.422, 0.473, 0.524,...
0.572, 0.617, 0.66, 0.702, 0.74, 0.776, 0.809, 0.832, 0, 0, 0;...
0, 0.069, 0.131, 0.191, 0.249, 0.306, 0.361, 0.414, 0.464, 0.512,...
0.558, 0.602, 0.643, 0.683, 0.719, 0.752, 0.775, 0, 0, 0, 0;...
0, 0.066, 0.127, 0.187, 0.244, 0.3, 0.353, 0.403, 0.452, 0.499,...
0.544, 0.586, 0.625, 0.662, 0.695, 0.718, 0, 0, 0, 0, 0;...
0, 0.065, 0.125, 0.183, 0.239, 0.292, 0.344, 0.394, 0.44, 0.485,...
0.528, 0.568, 0.605, 0.639, 0.66, 0, 0, 0, 0, 0, 0;...
0, 0.064, 0.122, 0.178, 0.232, 0.284, 0.334, 0.382, 0.427, 0.471,...
0.511, 0.548, 0.582, 0.605, 0, 0, 0, 0, 0, 0, 0;...
0, 0.061, 0.118, 0.174, 0.225, 0.277, 0.325, 0.371, 0.414, 0.455,...
0.492, 0.527, 0.549, 0, 0, 0, 0, 0, 0, 0, 0;...
0, 0.06, 0.114, 0.168, 0.219, 0.268, 0.314, 0.358, 0.399, 0.438,...
0.472, 0.495, 0, 0, 0, 0, 0, 0, 0, 0, 0;...
0, 0.057, 0.111, 0.163, 0.212, 0.259, 0.304, 0.345, 0.383, 0.418,...
0.442, 0, 0, 0, 0, 0, 0, 0, 0, 0, 0;...
0, 0.056, 0.107, 0.157, 0.204, 0.249, 0.29, 0.329, 0.365, 0.389,...
0, 0, 0, 0, 0, 0, 0, 0, 0, 0, 0;...
0, 0.053, 0.103, 0.151, 0.196, 0.239, 0.277, 0.313, 0.338, 0, 0,...
0, 0, 0, 0, 0, 0, 0, 0, 0, 0;...
0, 0.05, 0.098, 0.145, 0.187, 0.225, 0.263, 0.29, 0, 0, 0, 0, 0,...
0, 0, 0, 0, 0, 0, 0, 0;...
0, 0.049, 0.094, 0.137, 0.176, 0.214, 0.24, 0, 0, 0, 0, 0, 0, 0,...
0, 0, 0, 0, 0, 0, 0;...
0, 0.046, 0.089, 0.129, 0.166, 0.194, 0, 0, 0, 0, 0, 0, 0, 0, 0,...
0, 0, 0, 0, 0, 0;...
0, 0.042, 0.084, 0.121, 0.149, 0, 0, 0, 0, 0, 0, 0, 0, 0, 0, 0, 0,...
0, 0, 0, 0;...
0, 0.041, 0.078, 0.107, 0, 0, 0, 0, 0, 0, 0, 0, 0, 0, 0, 0, 0, 0,...
0, 0, 0;...
0, 0.037, 0.068, 0, 0, 0, 0, 0, 0, 0, 0, 0, 0, 0, 0, 0, 0, 0, 0,...
0, 0;...
0, 0.031, 0, 0, 0, 0, 0, 0, 0, 0, 0, 0, 0, 0, 0, 0, 0, 0, 0, 0, 0;...
0, 0, 0, 0, 0, 0, 0, 0, 0, 0, 0, 0, 0, 0, 0, 0, 0, 0, 0, 0, 0];

norm_f_inv = [
0, 0.0754, 0.1348, 0.1952, 0.2516, 0.3058, 0.3595, 0.4128, 0.4632,...
```

```
0.5136, 0.5650, 0.6139, 0.6622, 0.7094, 0.7561, 0.8007, 0.8420,...
0.8827, 0.9220, 0.9611, 1;...
0, 0.0745, 0.1333, 0.1930, 0.2489, 0.3026, 0.3557, 0.4084, 0.4583,...
0.5082, 0.5589, 0.6072, 0.6549, 0.7013, 0.7472, 0.7910, 0.8313,...
0.8708, 0.9086, 0.9265, 0;...
0, 0.0729, 0.1308, 0.1895, 0.2444, 0.2972, 0.3494, 0.4011, 0.4502,...
0.4992, 0.5488, 0.5961, 0.6425, 0.6878, 0.7323, 0.7747, 0.8135,...
0.8508, 0.8685, 0, 0;...
0, 0.0712, 0.1281, 0.1856, 0.2394, 0.2913, 0.3425, 0.3931, 0.4413,...
0.4893, 0.5376, 0.5838, 0.6290, 0.6730, 0.7159, 0.7569, 0.7938,...
0.8110, 0, 0, 0;...
0, 0.0695, 0.1253, 0.1816, 0.2342, 0.2852, 0.3353, 0.3848, 0.4321,...
0.4790, 0.5261, 0.5711, 0.6149, 0.6576, 0.6989, 0.7384, 0.7564,...
0, 0, 0, 0;...
0, 0.0677, 0.1224, 0.1775, 0.2290, 0.2790, 0.3280, 0.3764, 0.4227,...
0.4685, 0.5143, 0.5582, 0.6007, 0.6419, 0.6816, 0.7033, 0, 0, 0, 0,...
0;...
0, 0.0659, 0.1195, 0.1734, 0.2237, 0.2727, 0.3206, 0.3678, 0.4132,...
0.4580, 0.5024, 0.5452, 0.5862, 0.6261, 0.6488, 0, 0, 0, 0, 0, 0;...
0, 0.0641, 0.1166, 0.1692, 0.2184, 0.2664, 0.3132, 0.3592, 0.4037,...
0.4473, 0.4905, 0.5321, 0.5717, 0.5960, 0, 0, 0, 0, 0, 0, 0;...
0, 0.0623, 0.1137, 0.1651, 0.2130, 0.2600, 0.3057, 0.3506, 0.3941,...
0.4367, 0.4785, 0.5189, 0.5440, 0, 0, 0, 0, 0, 0, 0, 0;...
0, 0.0604, 0.1107, 0.1609, 0.2076, 0.2536, 0.2983, 0.3420, 0.3845,...
0.4260, 0.4664, 0.4937, 0, 0, 0, 0, 0, 0, 0, 0, 0;...
0, 0.0586, 0.1078, 0.1567, 0.2023, 0.2472, 0.2908, 0.3333, 0.3748,...
0.4153, 0.4433, 0, 0, 0, 0, 0, 0, 0, 0, 0, 0;...
0, 0.0568, 0.1048, 0.1525, 0.1969, 0.2409, 0.2833, 0.3246, 0.3652,...
0.3946, 0, 0, 0, 0, 0, 0, 0, 0, 0, 0, 0;...
0, 0.0549, 0.1019, 0.1483, 0.1915, 0.2344, 0.2758, 0.3160, 0.3466,...
0, 0, 0, 0, 0, 0, 0, 0, 0, 0, 0, 0;...
0, 0.0531, 0.0989, 0.1441, 0.1861, 0.2280, 0.2682, 0.2991, 0, 0, 0,...
0, 0, 0, 0, 0, 0, 0, 0, 0, 0;...
0, 0.0513, 0.0960, 0.1399, 0.1807, 0.2216, 0.2537, 0, 0, 0, 0, 0,...
0, 0, 0, 0, 0, 0, 0, 0, 0;...
0, 0.0494, 0.0930, 0.1356, 0.1753, 0.2092, 0, 0, 0, 0, 0, 0, 0, 0,...
0, 0, 0, 0, 0, 0, 0;...
0, 0.0476, 0.0900, 0.1314, 0.1647, 0, 0, 0, 0, 0, 0, 0, 0, 0, 0, 0,...
0, 0, 0, 0, 0;...
0, 0.0457, 0.0871, 0.1232, 0, 0, 0, 0, 0, 0, 0, 0, 0, 0, 0, 0, 0,...
0, 0, 0, 0;...
0, 0.0439, 0.0813, 0, 0, 0, 0, 0, 0, 0, 0, 0, 0, 0, 0, 0, 0, 0, 0,...
0, 0;...
0, 0.0403, 0, 0, 0, 0, 0, 0, 0, 0, 0, 0, 0, 0, 0, 0, 0, 0, 0, 0, 0;...
0, 0, 0, 0, 0, 0, 0, 0, 0, 0, 0, 0, 0, 0, 0, 0, 0, 0, 0, 0, 0];

new_a_hys = [alpha0_hys:-(alpha0_hys-beta0_hys)/(size(norm_f,2)...
-1):beta0_hys]; % this is the new scaled limits for alpha
new_b_hys = [beta0_hys:(alpha0_hys-beta0_hys)/(size(norm_f,2)...
-1):alpha0_hys]; % this is the new scaled limits for beta
new_f_hys = norm_f*(alpha0_hys-beta0_hys);
% this is the new scaled input mesh for first order transition curves

new_a_hys_inv = [alpha0_hys_inv:-(alpha0_hys_inv-...
beta0_hys_inv)/(size(norm_f_inv,2)-1):beta0_hys_inv];
% this is the new scaled limits for alpha
```

```
new_b_hys_inv = [beta0_hys_inv:(alpha0_hys_inv-...
beta0_hys_inv)/(size(norm_f_inv,2)-1):alpha0_hys_inv];
% this is the new scaled limits for beta
new_f_hys_inv = norm_f_inv*(alpha0_hys_inv-beta0_hys_inv);
% this is the new scaled input mesh for first order transition curves

% the slope scales the output of the function separately. It is applied
% to the output of the hysteresis function as a separate gain block.
slope_hys = (alpha0_hys_out - beta0_hys_out)/(alpha0_hys - beta0_hys);
slope_hys_inv =(alpha0_hys_out_inv...
- beta0_hys_out_inv)/(alpha0_hys_inv - beta0_hys_inv);
```

Code listing for “norm_preisach_xx…” which contains the code for the Preisach hysteresis simulink block

```
% this implementation is based on the "classical" preisach model for
% hysteresis
% found in section 1.4 of "Mathematical Models of Hysteresis and Their
% Applications" 2ed, by Isaak D. Mayergoyz, Elsevier Science,
% Amsterdam, 2003

% the implementation is called "norm_preisach_xx..."
% and calls an interpolation function "norm_intp_xx..." which is
% linear in both alpha and beta directions and uses a set of normalized
% mesh values "norm_f" for the first order transition curves. "norm_f"
% may be loaded as part of "norm_intp_xx" or loaded in
% "norm_load_xx..."

function [sys,x0,str,ts] = norm_preisach_v2g(t,x,u,flag)
% “Preisach” is the same as the file name.

switch flag
case 0
[sys,x0,str,ts] = mdlInitializeSizes();

case 3
sys = mdlOutputs(t,x,u);

case { 1, 2, 4, 9 }
sys = [];

otherwise
error(['Unhandled flag =', num2str(flag)]);
end

function [sys,x0,str,ts] = mdlInitializeSizes()
sizes = simsizes;
sizes.NumContStates = 0;
sizes.NumDiscStates = 1;
sizes.NumOutputs    = -1;   % dynamically sized
sizes.NumInputs     = -1;   % dynamically sized
sizes.DirFeedthrough    = 1;    % has direct feedthrough
sizes.NumSampleTimes    = 1;

sys = simsizes(sizes);
str = [];
x0 = [0];
ts = [-1 0];    % inherited sample time

% The above code is given as default when you choose a M-file
% S-function template.
%-------------------------------------------------------------------

function sys = mdlOutputs(t,x,u)
```

```
       % define global variables
global u_pre_hys num_alpha_hys num_beta_hys u_dir_be_hys u_dir_temp_hys
u_dir_cu_hys
global alpha_hys beta_hys alpha0_hys beta0_hys slope_hys new_f_hys
new_a_hys new_b_hys

       % u_pre_hys: previous input value
       % num_alpha: The number of alpha in the input signal
       % num_beta: The number of beta in the input signal
       % u_dir_be: previous input direction (positive(1), zero(0), or
       % negative(-1))
       % alpha, beta: data set of alpha and beta, respectively
       % u_dir_temp: input direction used temporarily
       % alpha0, beta0: alpha0 and beta0 are the upper and lower limits
       % of the half plane
       % triangle "T" of book section 1.2. they are parameters for the
       % function.
       % new_f, new_a, new_b: these are the scaled values for the
       % hysteresis output, the alpha and beta limits respectfully
       % u_dir_cu: current input direction (positive(1), zero(0), or
       % negative(-1))

if t <= 0
    u_pre_hys=0; num_alpha_hys=0; num_beta_hys=0; u_dir_be_hys=0;
    alpha_hys=0; beta_hys=0;
    u_dir_temp_hys=0; u_dir_cu_hys=0;
    sys = 0;

end

       % Determine an input direction
if u - u_pre_hys > 0          % if an input direction is positive,
       u_dir_cu_hys = 1;      % define a current input direction
                              % (u_dir_cu_hys) as 1
    elseif u - u_pre_hys < 0      % if an input direction is negative,
           u_dir_cu_hys = -1;     % define a current input direction
                                  % (u_dir_cu_hys) as -1
    else   u_dir_cu_hys = 0;      % if u - u_pre_hys = 0, a current input
                                  % direction (u_dir_cu_hys) = 0
end
if u_dir_be_hys ~= 0 && u - u_pre_hys == 0
% when a current input is the same as a previous input,
       u_dir_temp_hys = u_dir_be_hys;
% memorize the previous direction
end

%----------------------------------------------------------------------
% when input is between saturation limits and changing
if u_dir_cu_hys ~= 0 && u - beta0_hys > 0 && u - alpha0_hys < 0

% Find values of alpha and beta
% when an input direction changes,
    if u_dir_cu_hys * u_dir_be_hys == -1
% if a current direction is negative,
```

```
         if u_dir_cu_hys == -1
% increase the number of alpha,
            num_alpha_hys = num_alpha_hys + 1;
% save the previous input value in the alpha data set
            alpha_hys(num_alpha_hys) = u_pre_hys;
% if a current direction is positive,
         elseif u_dir_cu_hys == 1
% increase the number of beta,
            num_beta_hys = num_beta_hys + 1;
% save the previous input value in the beta data set
            beta_hys(num_beta_hys) = u_pre_hys;
         end
    end

           % Find values of alpha and beta, when two consecutive input
           % values were the same and now changed direction
    if u_dir_cu_hys * u_dir_be_hys == 0 && u_dir_cu_hys *
u_dir_temp_hys == -1
        if u_dir_cu_hys == -1
           num_alpha_hys = num_alpha_hys + 1;
           alpha_hys(num_alpha_hys) = u_pre_hys;
        elseif u_dir_cu_hys == 1
           num_beta_hys = num_beta_hys +1;
           beta_hys(num_beta_hys) = u_pre_hys;
        end
    end

% if a current input is bigger than the smallest value of alpha data
% set,
% delete the recent alpha value and beta value
    while num_alpha_hys > 0 && u > alpha_hys(num_alpha_hys)
               alpha_hys(num_alpha_hys) = 0;
               beta_hys(num_alpha_hys) = 0;
               num_alpha_hys = num_alpha_hys - 1;
               num_beta_hys = num_alpha_hys;
    end

% if a current input is smaller than the biggest value of beta data
% set,
% delete the recent alpha value and beta value
    while num_beta_hys > 0 && u < beta_hys(num_beta_hys)
               beta_hys(num_beta_hys) = 0;
               alpha_hys(num_beta_hys + 1) = 0;
               num_alpha_hys = num_beta_hys;
               num_beta_hys = num_beta_hys - 1;
    end

           % calculate the final displacement
           % when an input is increasing and there is no alpha value
    if num_alpha_hys == 0 && u_dir_cu_hys == 1
           sys = norm_intp_v2e(u,u,new_f_hys,new_a_hys,new_b_hys);
    end

           % when an input is decreasing,
    if u_dir_cu_hys == -1
        if num_alpha_hys == 0
```

```
            num_alpha_hys = 1;
            alpha_hys(num_alpha_hys) = alpha0_hys;
        end
        sys =
norm_intp_v2e(alpha_hys(num_alpha_hys),u,new_f_hys,new_a_hys,new_b_hys)
;
        if num_alpha_hys > 1
            for j = 1:num_alpha_hys - 1
                sys = sys +
norm_intp_v2e(alpha_hys(j),beta_hys(j),new_f_hys,new_a_hys,new_b_hys);
            end
            for j = 1:num_alpha_hys - 1
                sys = sys -
norm_intp_v2e(alpha_hys(j+1),beta_hys(j),new_f_hys,new_a_hys,new_b_hys)
;
            end
        end
    end

           % when an input is increasing,
    if u_dir_cu_hys == 1 && num_alpha_hys ~= 0
           sys = norm_intp_v2e(u,u,new_f_hys,new_a_hys,new_b_hys) -
norm_intp_v2e(u,beta_hys(num_beta_hys),new_f_hys,new_a_hys,new_b_hys);
           for j = 1:num_alpha_hys
           sys = sys +
norm_intp_v2e(alpha_hys(j),beta_hys(j),new_f_hys,new_a_hys,new_b_hys);
           end
           for j = 1:num_alpha_hys - 1
           sys = sys -
norm_intp_v2e(alpha_hys(j+1),beta_hys(j),new_f_hys,new_a_hys,new_b_hys)
;
           end
    end

% Initialize variables when an input is beta0 or alpha0.
%    if u - beta0_hys == 0
%           u_pre_hys = beta0_hys;
%           num_alpha_hys = 0;
%           num_beta_hys = 0;
%           u_dir_cu_hys = -1;
%           alpha_hys = beta0_hys;
%           beta_hys=beta0_hys;
%    elseif u - alpha0_hys == 0
%           u_pre_hys = beta0_hys;
%           num_alpha_hys = 0;
%           num_beta_hys = 0;
%           u_dir_cu_hys = 1;
%           alpha_hys = alpha0_hys;
%           beta_hys=alpha0_hys;
%    end

%    u_pre_hys = u;
%    u_dir_be_hys = u_dir_cu_hys;
    sys = beta0_hys + sys;

% when input is between saturation limits and not changing
```

```
elseif u_dir_cu_hys == 0 && u - beta0_hys > 0 && u - alpha0_hys < 0
    sys = x;
% when input is larger than upper hysteresis limit
elseif u - alpha0_hys >= 0
    sys = u; % sys = alpha0_hys;
% pass through input to output (one can also saturate @ alpha0)
    num_alpha_hys = 0;      % reset alpha and beta matrices
    num_beta_hys = 0;
    alpha_hys = alpha0_hys;
    beta_hys = alpha0_hys;
    u_dir_be_hys = 0; u_dir_temp_hys = 0;
% when input is smaller than lower hysteresis limit
elseif u - beta0_hys <= 0
% pass through input to output (one can also saturate @ beta0)
    sys = u;  % sys = beta0_hys;
    num_alpha_hys = 0;      % reset alpha and beta matrices
    num_beta_hys = 0;
    alpha_hys = beta0_hys;
    beta_hys = beta0_hys;
    u_dir_be_hys = 0; u_dir_temp_hys = 0;

end

    u_pre_hys = u;
    u_dir_be_hys = u_dir_cu_hys;
    x = sys;
```

Code listing for "norm_intp_xx…" which contains the code for the Preisach weight function interpolation called by the hysteresis and inverse hysteresis functions

```
function y = norm_intp_v2e(alpha,beta,new_f,new_a,new_b)

    % new_f, new_a and new_b are used as global
    % Based on a linear spline interpolation function, a displacement
    % value is computed with the information of alpha and beta.

%======================================================================
for i = 1:length(new_a) - 1
    if alpha >= new_a(i+1) & alpha <= new_a(i)  % position of alpha
% alpha1 and alpha2 in a cell having alpha value
    alpha1 = new_a(i); alpha2 = new_a(i+1);

        % When the position of alpha is known
    for j = 1:length(new_b) - 1
        if beta >= new_b(j) & beta <= new_b(j+1)    % position of beta
% beta1 and beta2 in a cell having beta value
           beta1 = new_b(j); beta2 = new_b(j+1);

            % When the position of beta is known
% (alpha,beta) is positioned in a triangular cell.
            if alpha2 == beta1

% the procedure of the linear spline interpolation in a triangular cell
                   new_f11 = new_f(i,j); new_f12=new_f(i,j+1);
                   new_f21=new_f(i+1,j);
                   new_a_t = inv([1 alpha1 beta1; 1 alpha1 beta2; 1
alpha2 beta1]) * [new_f11 new_f12 new_f21]';
% y is the output displacement value.
                   y = new_a_t' * [1 alpha beta]';
% (alpha,beta) is placed in a square cell.
            else

% the procedure of the linear spline interpolation in a square cell
                   new_f11 = new_f(i,j); new_f12 = new_f(i,j+1);
new_f21 =new_f(i+1,j); new_f22=new_f(i+1,j+1);
                   new_a_s = inv([1 beta1 alpha1 alpha1*beta1; 1 beta2
alpha1 alpha1*beta2;...
                        1 beta1 alpha2 alpha2*beta1; 1 beta2 alpha2
alpha2*beta2]) * [new_f11 new_f12 new_f21 new_f22]';
                   y = new_a_s' * [1 beta alpha alpha*beta]';
            end

% the output becomes zero when alpha < beta.
            if alpha < beta
                   y = 0;
            end

% Once the output is obtained, the FOR loops are terminated.
            break
        end
```

```
    end;
end;
end
```

Code listing for “norm_preisach_inv_xx…” which contains the code for the Preisach inverse hysteresis simulink block

```
% this implementation is based on the "classical" preisach model for
% hysteresis found in section 1.4 of "Mathematical Models of Hysteresis
% and Their Applications" 2ed, by Isaak D. Mayergoyz, Elsevier Science,
% Amsterdam, 2003

% the implementation is called "norm_preisach_xx..."
% and calls an interpolation function "norm_intp_xx..." which is
% linear in both alpha and beta directions and uses a set of normalized
% mesh values "norm_f" for the first order transition curves. "norm_f"
% may be loaded as part of "norm_intp_xx" or loaded in
% "norm_load_xx..."

% “Preisach” is the same as the file name.
function [sys,x0,str,ts] = norm_preisach_v2g_inv(t,x,u,flag)


switch flag
case 0
[sys,x0,str,ts] = mdlInitializeSizes();

case 3
sys = mdlOutputs(t,x,u);

case { 1, 2, 4, 9 }
sys = [];

otherwise
error(['Unhandled flag =', num2str(flag)]);
end

function [sys,x0,str,ts] = mdlInitializeSizes()
sizes = simsizes;
sizes.NumContStates = 0;
sizes.NumDiscStates = 1;
sizes.NumOutputs    = -1;   % dynamically sized
sizes.NumInputs     = -1;   % dynamically sized
sizes.DirFeedthrough    = 1;    % has direct feedthrough
sizes.NumSampleTimes    = 1;

sys = simsizes(sizes);
str = [];
x0 = [0];
ts = [-1 0];    % inherited sample time

% The above code is given as default when you choose a M-file
% S-function template.
%-----------------------------------------------------------------------

function sys = mdlOutputs(t,x,u)
```

```
       % define global variables
global u_pre_hys_inv num_alpha_hys_inv num_beta_hys_inv
u_dir_be_hys_inv u_dir_temp_hys_inv u_dir_cu_hys_inv
global alpha_hys_inv beta_hys_inv alpha0_hys_inv beta0_hys_inv
slope_hys_inv new_f_hys_inv new_a_hys_inv new_b_hys_inv

       % u_pre_hys_inv: previous input value
       % num_alpha_hys_inv: The number of alpha in the input signal
       % num_beta_hys_inv: The number of beta in the input signal
       % u_dir_be_hys_inv: previous input direction (positive(1),
       % zero(0), or negative(-1))
       % alpha, beta: data set of alpha and beta, respectively
       % u_dir_temp_hys_inv: input direction used temporarily
       % alpha0, beta0: alpha0 and beta0 are the upper and lower limits
       % of the half plane triangle "T" of book section 1.2. they are
       % parameters for the function. new_f, new_a, new_b: these are
       % the scaled values for the hysteresis output, the alpha and
       % beta limits respectfully u_dir_cu_hys_inv: current input
       % direction (positive(1), zero(0), or negative(-1))

if t <= 0
    u_pre_hys_inv=0; num_alpha_hys_inv=0; num_beta_hys_inv=0;
u_dir_be_hys_inv=0;
    alpha_hys_inv=0; beta_hys_inv=0;
    u_dir_temp_hys_inv=0; u_dir_cu_hys_inv=0;
    sys = 0;
end

% Determine an input direction
% if an input direction is positive,
if u - u_pre_hys_inv > 0
% define a current input direction (u_dir_cu_hys_inv) as 1
    u_dir_cu_hys_inv = 1;
% if an input direction is negative,
    elseif u - u_pre_hys_inv < 0
% define a current input direction (u_dir_cu_hys_inv) as -1
           u_dir_cu_hys_inv = -1;
% if u - u_pre_hys_inv = 0, a current input direction
% (u_dir_cu_hys_inv) = 0
    else   u_dir_cu_hys_inv = 0;
end
% when a current input is the same as a previous input,
if u_dir_be_hys_inv ~= 0 && u - u_pre_hys_inv == 0
% memorize the previous direction
       u_dir_temp_hys_inv = u_dir_be_hys_inv;
end

%-----------------------------------------------------------------------
% when input is between saturation limits and changing
if u_dir_cu_hys_inv ~= 0 && u - beta0_hys_inv > 0 && u - alpha0_hys_inv
< 0

% Find values of alpha and beta
% when an input direction changes,
    if u_dir_cu_hys_inv * u_dir_be_hys_inv == -1
```

```
% if a current direction is negative,
         if u_dir_cu_hys_inv == -1
% increase the number of alpha,
            num_alpha_hys_inv = num_alpha_hys_inv + 1;
% save the previous input value in the alpha data set
            alpha_hys_inv(num_alpha_hys_inv) = u_pre_hys_inv;
% if a current direction is positive,
         elseif u_dir_cu_hys_inv == 1
% increase the number of beta,
            num_beta_hys_inv = num_beta_hys_inv + 1;
% save the previous input value in the beta data set
            beta_hys_inv(num_beta_hys_inv) = u_pre_hys_inv;
         end
    end

% Find values of alpha and beta, when two consecutive input
% values were the same and now changed direction
    if u_dir_cu_hys_inv * u_dir_be_hys_inv == 0 && u_dir_cu_hys_inv *
u_dir_temp_hys_inv == -1
        if u_dir_cu_hys_inv == -1
           num_alpha_hys_inv = num_alpha_hys_inv + 1;
           alpha_hys_inv(num_alpha_hys_inv) = u_pre_hys_inv;
        elseif u_dir_cu_hys_inv == 1
           num_beta_hys_inv = num_beta_hys_inv +1;
           beta_hys_inv(num_beta_hys_inv) = u_pre_hys_inv;
        end
    end

% if a current input is bigger than the smallest value of alpha data
% set,
% delete the recent alpha value and beta value
    while num_alpha_hys_inv > 0 && u > alpha_hys_inv(num_alpha_hys_inv)
               alpha_hys_inv(num_alpha_hys_inv) = 0;
               beta_hys_inv(num_alpha_hys_inv) = 0;
               num_alpha_hys_inv = num_alpha_hys_inv - 1;
               num_beta_hys_inv = num_alpha_hys_inv;
    end

% if a current input is smaller than the biggest value of beta data
% set,
% delete the recent alpha value and beta value
    while num_beta_hys_inv > 0 && u < beta_hys_inv(num_beta_hys_inv)
               beta_hys_inv(num_beta_hys_inv) = 0;
               alpha_hys_inv(num_beta_hys_inv + 1) = 0;
               num_alpha_hys_inv = num_beta_hys_inv;
               num_beta_hys_inv = num_beta_hys_inv - 1;
    end

% calculate the final displacement
% when an input is increasing and there is no alpha value
    if num_alpha_hys_inv == 0 && u_dir_cu_hys_inv == 1
           sys =
norm_intp_v2e(u,u,new_f_hys_inv,new_a_hys_inv,new_b_hys_inv);
    end

% when an input is decreasing,
```

```
    if u_dir_cu_hys_inv == -1
        if num_alpha_hys_inv == 0
            num_alpha_hys_inv = 1;
            alpha_hys_inv(num_alpha_hys_inv) = alpha0_hys_inv;
        end
        sys =
norm_intp_v2e(alpha_hys_inv(num_alpha_hys_inv),u,new_f_hys_inv,new_a_hy
s_inv,new_b_hys_inv);
        if num_alpha_hys_inv > 1
            for j = 1:num_alpha_hys_inv - 1
                sys = sys +
norm_intp_v2e(alpha_hys_inv(j),beta_hys_inv(j),new_f_hys_inv,new_a_hys_
inv,new_b_hys_inv);
            end
            for j = 1:num_alpha_hys_inv - 1
                sys = sys -
norm_intp_v2e(alpha_hys_inv(j+1),beta_hys_inv(j),new_f_hys_inv,new_a_hy
s_inv,new_b_hys_inv);
            end
        end
    end

% when an input is increasing,
    if u_dir_cu_hys_inv == 1 && num_alpha_hys_inv ~= 0
           sys =
norm_intp_v2e(u,u,new_f_hys_inv,new_a_hys_inv,new_b_hys_inv) -
norm_intp_v2e(u,beta_hys_inv(num_beta_hys_inv),new_f_hys_inv,new_a_hys_
inv,new_b_hys_inv);
           for j = 1:num_alpha_hys_inv
           sys = sys +
norm_intp_v2e(alpha_hys_inv(j),beta_hys_inv(j),new_f_hys_inv,new_a_hys_
inv,new_b_hys_inv);
           end
           for j = 1:num_alpha_hys_inv - 1
           sys = sys -
norm_intp_v2e(alpha_hys_inv(j+1),beta_hys_inv(j),new_f_hys_inv,new_a_hy
s_inv,new_b_hys_inv);
           end
    end

% Initialize variables when an input is beta0 or alpha0.
%    if u - beta0_hys_inv == 0
%           u_pre_hys_inv = beta0_hys_inv;
%           num_alpha_hys_inv = 0;
%           num_beta_hys_inv = 0;
%           u_dir_cu_hys_inv = -1;
%           alpha_hys_inv = beta0_hys_inv;
%           beta_hys_inv=beta0_hys_inv;
%    elseif u - alpha0_hys_inv == 0
%           u_pre_hys_inv = beta0_hys_inv;
%           num_alpha_hys_inv = 0;
%           num_beta_hys_inv = 0;
%           u_dir_cu_hys_inv = 1;
%           alpha_hys_inv = alpha0_hys_inv;
%           beta_hys_inv=alpha0_hys_inv;
%    end
```

```
%    u_pre_hys_inv = u;
%    u_dir_be_hys_inv = u_dir_cu_hys_inv;

    sys = beta0_hys_inv + ((u - beta0_hys_inv) + ((u - beta0_hys_inv) -
sys)); %    sys = beta0_hys_inv + sys;


% when input is between saturation limits and not changing
elseif u_dir_cu_hys_inv == 0 && u - beta0_hys_inv > 0 && u -
alpha0_hys_inv < 0
    sys = x;

% when input is larger than upper hysteresis limit
elseif u - alpha0_hys_inv >= 0

% pass through input to output (one can also saturate @ alpha0)
    sys = u; % sys = alpha0_hys_inv;
    num_alpha_hys_inv = 0;      % reset alpha and beta matrices
    num_beta_hys_inv = 0;
    alpha_hys_inv = alpha0_hys_inv;
    beta_hys_inv = alpha0_hys_inv;
    u_dir_be_hys_inv = 0; u_dir_temp_hys_inv = 0;
% when input is smaller than lower hysteresis limit
elseif u - beta0_hys_inv <= 0
% pass through input to output (one can also saturate @ beta0)
    sys = u;  % sys = beta0_hys_inv;
    num_alpha_hys_inv = 0;      % reset alpha and beta matrices
    num_beta_hys_inv = 0;
    alpha_hys_inv = beta0_hys_inv;
    beta_hys_inv = beta0_hys_inv;
    u_dir_be_hys_inv = 0; u_dir_temp_hys_inv = 0;

end

    u_pre_hys_inv = u;
    u_dir_be_hys_inv = u_dir_cu_hys_inv;
    x = sys;
```

APPENDIX B: SIMULATION TUNING ANALYSIS

1^{st} order Han_1 Function velocity control tuning analysis

For small error signals where the system does not command saturated control, the 1^{st} order Han_1 Function equations are those of the Isochronic Region alone:

$$\begin{aligned} &u = fst_1(x, r, h) \\ &d = rh \\ &fst_1 = -r\frac{x}{d} = -\frac{x}{h}, \quad |x| \le d \Rightarrow |x| \le rh \end{aligned} \tag{B1}$$

The nonlinear action of the control, to drive large error quickly into the Isochronic Region, is a heuristic tuning process to achieve some performance parameters, and then fine tune to achieve a non-cycling control while in the IR. One can tune the linear response within the IR, if one has the benefit of a system model. The transfer function from control to velocity is:

$$\frac{K_{vf}}{(b_{eq}+m)s+k_{eq}} * G_{elec}(s) \tag{B2}$$

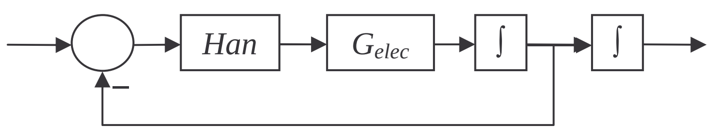

Figure 59 Han_1 Function velocity

(The electrical subsystem harmonic zero and pole pairs are beyond the mechanical complex poles, shown in the Bode plots, and are negligible for the tuning.) One may choose a stable closed loop controller $C(s) = -7e^9$ with greater than unity gain above $1e^9$ rad/sec as a starting point, which gives the Bode plots in Figure 60. The result was the accuracy was “optimum”, but with almost constant control cycling, with slow control magnitude decay until some input change occurred.

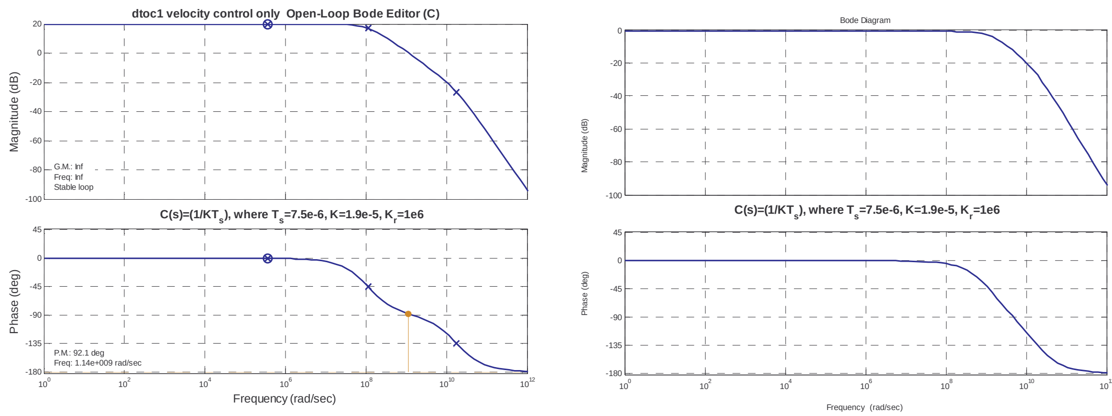

Figure 60 Han$_1$ Function velocity, open and closed loop Bode tuning plots:

Increasing the value of the tuning variables h and r in the simulation blocks allows one to improve the performance to the point where the state remains in the Isochronic Region without cycling the control, any beyond this point may improve accuracy and disturbance rejection at the expense of control energy. Small Signal $C(s) = -8e^{11}$ The velocity tracking error in this case is $<2e^{-7}/8e^{-5} = 0.25\%$. We tuned the Han$_1$ Function without benefit of a model, using the previous heuristic method, arriving at values close to these.

1^{st} order Han_1 Function velocity plus PI position control tuning analysis

The equivalent SMALL SIGNAL control is a PID configuration, where the Han_1 Function gain, $1/K_hT_s$, is the overall control gain, the derivative gain, $K_d = 1$, and the values of $K_p/2=133k$ and $K_i = K_p/4$ are chosen to place the pair of real zeros in the left half plane and critically damped at the plant resonant poles. This gives one a stable system with no phase lag past 180°. (One should err on the low gain side if tuning manually, $K_p < 8e^5/3$)

$$\begin{aligned} u(s) &= \left(\frac{1}{K_hT_s}\right)\left(se(s) + K_pe(s) + \frac{K_pK_i}{s}e(s)\right) \\ &= \left(\frac{1}{K_hT_s}\right)\left(\frac{s^2 + K_ps + K_pK_i}{s}\right)e(s) \end{aligned} \tag{B3}$$

If one chooses, as before, to start designing with a stable system with no phase lag past 180° and gain > 1 below the resonant frequency, then one has, $K_h=4e^{-9}/3$, $K_r = 1e^{10}$,

$$u(s) = -1e^{14}\left(\frac{s^2 + \left(8e^5/3\right)s + \left(16e^{10}/9\right)}{s}\right)e(s) \tag{B4}$$

What one discovers from this initial tuning setting is that one is at the boundary where the control cycles constantly if the input is at this resonant frequency. If one then increases sample time h (K_h) and/or the saturation limit r (K_r) one immediately observes the control will begin to enter the Isochronic Region for the Han_1 Function, and stop cycling for short periods. This is a practical result to be desired, so one can choose $K_r = 1e^8$, as for the velocity controller only. Doing so still provides a stable system with practical performance:

$$u(s) = -8.3e^{11}\left(\frac{s^2 + \left(8e^5/3\right)s + \left(16e^{10}/9\right)}{s}\right)e(s) \tag{B5}$$

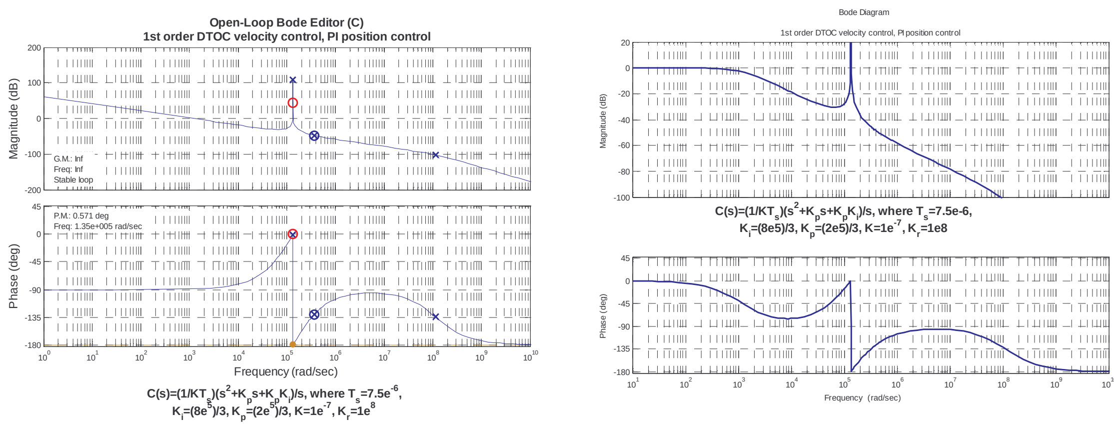

Figure 61 Han$_1$ Function velocity with PI position control: Bode tuning plots.

1^{st} order Han_1 Function velocity plus 2^{nd} order Han_2 position control tuning analysis

$$
\begin{aligned}
C(s) &= Han_2(s) + Han_1(s) \\
&= \left(\frac{2}{K_h T_s^2}\right)\left(s + \frac{1}{2K_h T_s}\right) + \left(\frac{1}{K_h T_s}\right)s \\
&= \left(\frac{2+T_s}{K_h T_s^2}\right)\left(s + \frac{1}{(2+T_s)K_h T_s}\right)
\end{aligned}
\tag{B6}
$$

As a starting point exercise one can place the zero at the resonance and calculate the gain values for gain > 1 below the resonant frequency.

Small Signal $C(s) \approx -\frac{1e^{13}}{3}\left(s + \frac{4e^5}{3}\right)$ but there is not enough steady state error correction in this tuning choice, even though the performance is acceptable otherwise. One would next raise the value of $K_{r2} = 1.33e^{15}$ and test. $C(s) \approx -\frac{1e^{15}}{3}\left(s + \frac{4e^5}{3}\right)$

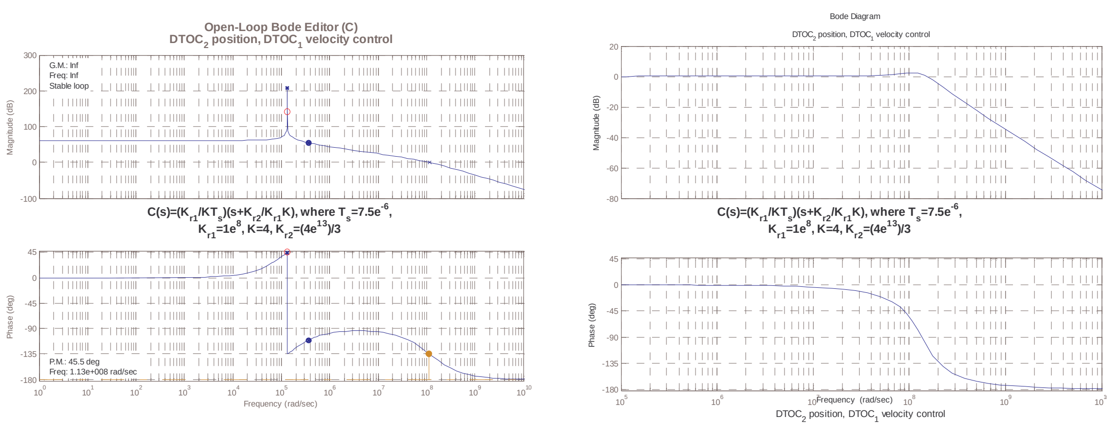

Figure 62 Han Function position and velocity control: Bode tuning plots.

Linear Active Disturbance Rejection Control(LADRC) tuning analysis

The LESO presents an equivalent double integrator plant to the controller:

$$G_p(s) \approx \frac{b}{s^2} = \frac{-25.33}{s^2} \tag{B7}$$

Using these heuristics that observer frequency $\omega_o \approx 10x$ the max frequency at which one desires to operate, and then use a controller frequency $\omega_c = \omega_o/3$. the initial PD controller is:

$$G_c(s) = K_d s + K_p = 2\omega_c s + \omega_c^2 = 2\omega_c\left(s + \frac{\omega_c}{2}\right) = \frac{8e^6}{9}\left(s + \frac{2e^6}{9}\right) \tag{B8}$$

The open loop Bode plot and disturbance response for this design indicates that the response will lag the input ~ 1°, which is not acceptable performance, but the system is stable with excellent phase margin.

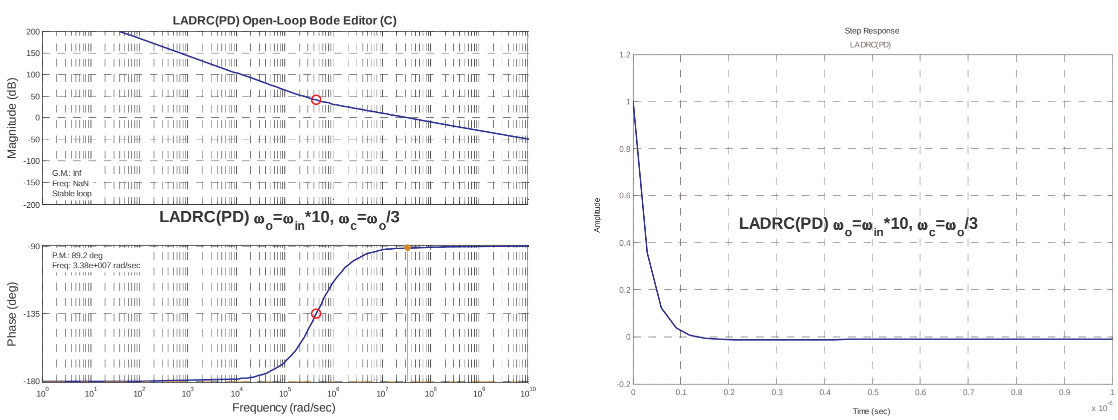

Figure 63 LADRC(PD), Bode plot & Disturbance Response

Active Disturbance Rejection Control with Han$_1$ velocity and Proportional position control tuning analysis

The Han$_1$ Function velocity control has the transfer function:

$$u(s) = \left(\frac{1}{K_h T_s}\right) s \cdot e(s) = C(s)e(s) \tag{B9}$$

so that the Han$_1$ Function in velocity mode appears as a linear derivative control for small signals.

The small signal transfer function for Han$_1$ Function combined with proportional position control is:

$$u(s) = \left(\left(\frac{1}{K_h T_s}\right)s + K_p\right)e(s) = \left(\frac{1}{K_h T_s}\right)\left(s + K_p K_h T_s\right)e(s) = C(s)e(s) \tag{B10}$$

One may tune the preferred response with K_h = *1e-7*, K_p = *1e*^{7} to give a small signal control: $C(s) = -\frac{4e^{12}}{3}\left(s + 7.5e^{-6}\right)$

What one discovers from this tuning setting is that if one the decreases gain K_h and/or reduces K_r one immediately observes the control will begin to leave the Isochronic Region for the Han$_1$ Function, and start cycling for short periods, the same results as for the Han$_1$ Function alone.

APPENDIX C: STABILITY OF HYSTERESIS AND ITS DERIVATIVE

Any analysis of necessity assumes the physical process is accurately represented by the model equation, in this case our assumptions are not only Newtonian mechanics but also that the hysteresis model is an accurate representation. Recalling Equations (3.4) and (3.5) for the Preisach and Prandtl-Ishlinskii hysteresis in terms of the "relay" basis function:

$$\begin{aligned} &P[u](t) = \\ &w_P(t) = \int_0^\infty \int_{-\infty}^\infty \mu(r,s) R_{s-r,s+r}[u](t)\,ds\,dr \end{aligned} \tag{C.1a}$$

$$\begin{aligned} &PI[u](t) = \\ &w_{PI}(t) = \int_0^\infty \int_{-\infty}^\infty -\frac{\rho(r)}{2} R_{s-r.s+r}[u](t)\,ds\,dr + u(t)\int_0^\infty \rho(r)\,dr \end{aligned} \tag{C.1b}$$

it becomes apparent, as Krejci [76,77] demonstrates, the quasilinear equation encompasses a Prandtl-Ishlinskii operator inverse, which is itself a Prandtl-Ishlinskii operator, where the integral of the weight equals the identity operator, in our case = 1. It is the character of the weight function, $\rho(r)$, more so than the simple integral value, that is important for our proof. Specifically, are $\rho(r)$ and $\dot{\rho}(r)$ and/or $\mu(r,s)$ and $\dot{\mu}(r,s)$ Lipschitz bounded over the operating range?

The mathematic models of hysteretic behavior are composed of infinite sums or integrals of weighted basis "relay", "play" or "stop" operators. It is usual to pass from the double integral of the weighted basis operator to an area integral of the weight function over the "Preisach Plane", whereby the "memory evolution" curve which bisects the plane into positive and negative regions contains all current condition and history to calculate the output for any input. This is also the technique most used in practical applications.

The progression for the analysis in this appendix, which can be attributed to Brokate & Sprekels [10], is first to demonstrate the Lipschitz continuity and boundedness of the constituent basis operators, and then extend that Lipschitz condition to the memory curve, and finally to the full hysteresis function itself. Similar proofs to this are available in Krejci [76,77] and Visintin [127]. Once Lipschitz boundedness is established for the hysteresis transformation it is straightforward to show the BIBO stability of the LESO observer and the closed loop LADRC feedback control itself, as we claimed in Chapter 6.

C.1 Lipschitz Properties of the "play" and "stop" basis operators

One primary condition for the Lipschitz property of the hysteresis function is the assumption of continuous piecewise monotonic input functions. This is not a constraint in practical applications, control signal power amplifiers have rise time and saturation limits. Most applications have smooth input profile designs. The strategy of the proof are consideration of a continuous input as a sequence of piecewise monotonic functions and then extended to the limit. Before proceeding to provide the main result in this section we introduce the sets of appropriate inputs.

$$\begin{aligned} &M_{pm}[0,T] \; \textit{the set of all piecewise monotone functions on} [0,T], \\ &C_{pm}[0,T] = M_{pm}[0,T] \cap C[0,T] \\ &\textit{the set of all continuous piecewise monotone functions on} [0,T]. \end{aligned} \tag{C.2}$$

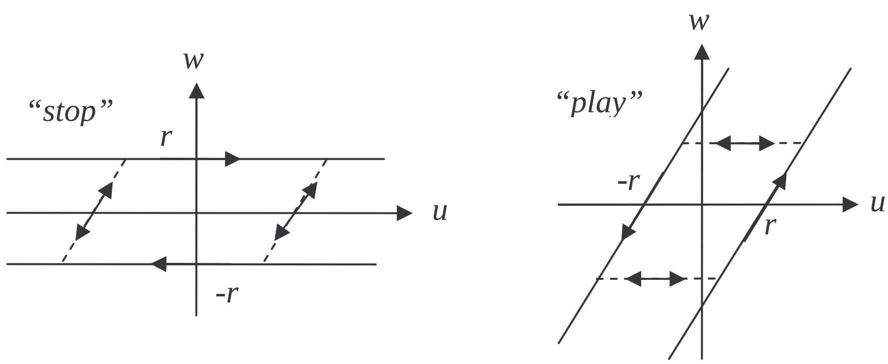

Figure 64 "Stop" and "Play" Operators

Recalling the definitions of Equation (3.3)

$$
\begin{aligned}
& F_r[\lambda^0, u](t) = w(t), \\
& w(0) = f_r(u(0), 0), \\
& w(t) = f_r(u(t), w(t_i)), \ \ for\ \ t_i < t \le t_{i+1},\ 0 \le i \le N-1, \\
& where\ u(t)\ is\ monotone\ in\ N\ subintervals\ of\ [0,T], \\
& f_r(u,w) = \max\left\{u-r, \min\left\{u+r, w\right\}\right\}, r \ge 0,
\end{aligned} \tag{C.3a}
$$

$$
\begin{aligned}
& E_r[\lambda^0, u](t) = w(t), \\
& w(0) = e_r(u(0)), \\
& w(t) = e_r(u(t) - u(t_i) + w(t_i)),\ for\ t_i < t \le t_{i+1},\ 0 \le i \le N-1, \\
& where\ u(t)\ is\ monotone\ in\ N\ subintervals\ of\ [0,T], \\
& e_r(u) = \min\left\{r, \max\left\{-r, u\right\}\right\}, r \ge 0,
\end{aligned} \tag{C.3b}
$$

$$
F_r + E_r = I_d \quad \text{such that} \quad F_r[u](t) + E_r[u](t) = u(t), \tag{C.3c}
$$

it follows that

$$
\begin{aligned}
& F_r[u](t) \le u(t)\ and\ E_r[u](t) \le u(t), \\
& F_r[u]'(t) + E_r[u]'(t) = \dot{u}(t), \\
& and\ F_r[u]'(t) \le \dot{u}(t)\ and\ E_r[u]'(t) \le \dot{u}(t).
\end{aligned} \tag{C.3d}
$$

From the definition (C.3a)

$$\begin{aligned}
&f_r(u+c, w+c) = f_r(u, w) + c, \\
&f_r(-u, -w) = -f_r(u, w), \\
&f_r(u, f_r(u, w)) = f_r(u, w),
\end{aligned} \tag{C.3e}$$

one obtains (*straightforward proof omitted*):

$$\begin{aligned}
&w_0 = F_r[\lambda^0, u](0), \\
&F_r[u; w_0] = F_r[u - w_0] + w_0, \\
&F_r[-u; -w_0] = -F_r[u; w_0], \\
&F_r[u; F_r[u; w_0](0)] = F_r[u; w_0], \\
&F_r[F_s[u; y_0]; w_0] = F_{r+s}[u; w_0] = F_r \circ F_s, \ \textit{for } |y_0 - w_0| \le r \\
&\textit{and} \\
&F_r[u_1; w_{0,1}] \le F_r[u_2; w_{0,2}], \textit{ if } \ u_1 \le u_2 \ \textit{ and } \ w_{0,1} \le w_{0,2}.
\end{aligned} \tag{C.3f}$$

<u>Lemma C.1 (Continuity of the “play” operator’s update function f_r)</u>

Function $f_r : \mathbb{R} \times \mathbb{R} \to \mathbb{R}$ *defined by*

$$f_r(u, w) = \max\{u - r, \min\{u + r, w\}\}, r \ge 0 \tag{C.4a}$$

satisfies the inequality

$$|f_{r1}(u_1, w_1) - f_{r2}(u_2, w_2)| \le \max\{|u_1 - u_2| + |r_1 - r_2|, |w_1 - w_2|\} \tag{C.4b}$$

for any $r_j \ge 0, u_j, w_j \in \mathbb{R}, j = 1, 2.$

Proof: For any $a, b, c, d \in \mathbb{R}$, *one has*

$$|\max\{a, b\} - \max\{c, d\}| \le \max\{|a - c|, |b - d|\}. \tag{C.4c}$$

The same holds for “min” function on left side. Therefore

$$\begin{aligned}
&|f_{r1}(u_1, w_1) - f_{r2}(u_2, w_2)| \\
&\le \max\{|(u_1 - r_1) - (u_2 - r_2)|, |(u_1 + r_1) - (u_2 + r_2)|, |w_1 - w_2|\}
\end{aligned} \tag{C.4d}$$

which implies Equation (C.4a). ■

From Lemma C.1 (Continuity of the "play" operator's update function f_r) one can conclude

$$\begin{aligned} &\left|F_{r1}[u_1, w_{0,1}](t) - F_{r2}[u_2, w_{0,2}](t)\right| \\ &\leq \max\left\{\left|r_1 - r_2\right| + \sup_{0\leq\tau\leq t}\left|u_1(\tau) - u_2(\tau)\right|, \left|w_{0,1} - w_{0,2}\right|\right\}, \qquad \text{(C.5)} \\ &\textit{for all } u_1, u_2 \in M_{pm}[0,T] \textit{ and any } t \in [0,T] \end{aligned}$$

by induction.

One then may continue from the boundedness of the "play" operator update function to that for the basis operator itself.

Lemma C.2 (Lipschitz continuity of "play" operator $F_r[u](t)$ on C[0,T])

For any $r \geq 0$ and the "play" operator $F_r : C[0,T]\times\mathbb{R} \to C[0,T]$ we have

$$\left\|F_r[u_1; w_{0,1}] - F_r[u_2; w_{0,2}]\right\|_\infty \leq \max\left\{\left\|u_1 - u_2\right\|_\infty, \left|w_{0,1} - w_{0,2}\right|\right\}, \qquad \text{(C.6a)}$$

$$\left|F_r[u; w_0](t) - F_r[u; w_0](t')\right| \leq \sup_{t'\leq\tau\leq t}\left|u(\tau) - u(t')\right|, \qquad \text{(C.6b)}$$

$$F_r[u; w_0] = F_r[u - w_0] + w_0, \qquad \text{(C.6c)}$$

$$F_r[u_1; w_{0,1}] \leq F_r[u_2; w_{0,2}], \textit{ if } u_1 \leq u_2 \textit{ and } w_{0,1} \leq w_{0,2}, \qquad \text{(C.6d)}$$

$$F_r[F_s[u; y_0]; w_0] = F_{r+s}[u; w_0], \textit{ if } \left|y_0 - w_0\right| \leq r. \qquad \text{(C.6e)}$$

for all $u, u_1, u_2 \in C[0,T]$ and for any $s \geq 0$, where $w_0, w_{0,1}, w_{0,2}, y_0 \in \mathbb{R}$ and $0 \leq t' \leq t \leq T$.

Proof: For $u, u_1, u_2 \in M_{pm}[0,T]$ Equation (C.6c), (C.6d) and (C.6e) follow from Equation (C.3f). Equation (C.6a) follows directly from Equation (C.5). If one sets

$u_1 = u$, and $u_2 = u_{t'}$ then (C.6b) follows from (C.6a) and one can extend F_r continuously on the dense subset $C_{pm}[0,T]\times\mathbb{R} \subset C[0,T]\times\mathbb{R}$ onto $C[0,T]\times\mathbb{R}$ itself. ■

Similarly, one may also follow the same process for the "stop" operator as for the "play" operator to show the Lipschitz boundedness.

<u>Lemma C.3 (Lipschitz continuity of "stop" operator $E_r[u](t)$ on $C[0,T]$)</u>

Define $e_r : \mathbb{R} \to \mathbb{R}$ as a Lipschitz continuous operator as in Equation (C.3b)

$$\begin{aligned} &E_r[\lambda^0, u](t) = e_r(u(t) - u(t_i) + w(t_i)), \\ &e_r(u) = \min\{r, \max\{-r, u\}\}, r \geq 0. \end{aligned} \tag{C.7a}$$

Then for any initial value $w_0 \in \mathbb{R}$, $E_r : C[0,T]\times\mathbb{R} \to C[0,T]$ holds for all $u, u_1, u_2 \in C[0,T]$ and for any $s \geq 0$, where $w_0, w_{0,1}, w_{0,2} \in \mathbb{R}$, and $0 \leq t' \leq t \leq T$, we have

$$\|E_r[u_1] - E_r[u_2]\|_\infty \leq 2\|u_1 - u_2\|_\infty, \tag{C.7b}$$

$$|E_r[u](t) - E_r[u](t')| \leq 2 \sup_{t' \leq \tau \leq t} |u(\tau) - u(t')|, \tag{C.7c}$$

$$|E_r[u](t) - E_r[u](t')| \leq 2 \sup_{t' \leq \tau, \tau' \leq t} |u(\tau) - u(\tau')|, \tag{C.7d}$$

$$E_r[u; w_0] + F_r[u; w_0] = u, \tag{C.7e}$$

$$E_r[u; w_0] = E_r[u - w_0], \tag{C.7f}$$

$$E_r[u_1; w_{0,1}] \leq E_r[u_2; w_{0,2}], \text{ if } u_1 \leq u_2 \text{ and } w_{0,1} \leq w_{0,2}, \tag{C.7g}$$

$$E_r[E_s[u; y_0]; w_0] = E_{r+s}[u; w_0], \text{ if } |y_0 - w_0| \leq r. \tag{C.7h}$$

Proof: Equation (C.7e) follows from (C.3c) and the proof of (C.7g) is elementary from (C.3b). Equations (C.7b), (C.7c), (C.7f) and (C.7h) follow from comparable equations of Lemma C.2. Equation (C.7d) may be proved by setting $u \in C_{pm}[0,T]$, *and* $t' < t \in [0,T]$, *and* $w = E_r[u]$. *Consider the case*

$$w(t) - u(t) < w(t') - u(t'). \tag{C.7i}$$

From Figure 65 it is clear that $P = (u(t) + r - w(t), r)$ *must be passed at some time* $\tau \in [t', t]$ *so that:*

$$w(\tau) = r,\ u(\tau) - u(t) = r - w(t) \tag{C.7j}$$

Since r is an upper bound for both w(t′) and w(t) one obtains from (C.7i) and (C.7j)

$$\begin{aligned} \left| w(t) - w(t') \right| &\leq \max\left\{ r - w(t'), r - w(t) \right\} \\ &\leq \max\left\{ u(\tau) - u(t'), u(\tau) - u(t) \right\} \end{aligned} \tag{C.7k}$$

which proves the assertion. ■

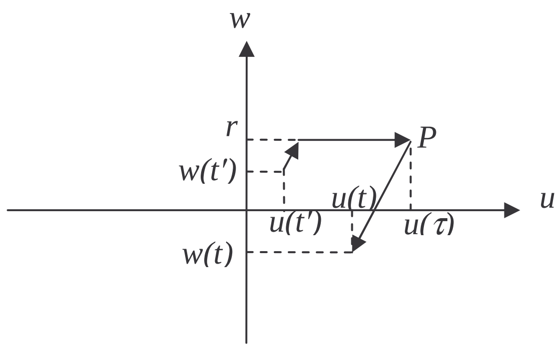

Figure 65 The case $w(t) - u(t) < w(t') - u(t')$

C.2 Lipschitz Properties of the "play" and "stop" basis operator derivatives

As important as the boundedness of the basis operators themselves for the stability property of the ADRC is the boundedness of their derivatives. Let us define a new subset of continuous functions: $C_{pl}[0,T] = \left\{ u \in C[0,T] \,\middle|\, u \text{ is } \textit{piecewise linear} \right\}$

<u>Lemma C.4 (Lipschitz properties of $F_r[u](t)$and $E_r[u](t)$ derivatives)</u>

Let $r \geq 0$ *and* $u_1, u_2 \in C_{pl}[0,T]$. *Then*

$$\left| F_r[u_1]'(t) - F_r[u_2]'(t) \right| + \left| E_r[u_1] - E_r[u_2] \right|'(t) \leq \left| \dot{u}_1(t) - \dot{u}_2(t) \right| \tag{C.8a}$$

for all $t \in [0,T]$ *except for at most a finite number of points.*

Proof: Let

$$\sigma(t) = sign\left(E_r[u_1](t) - E_r[u_2](t) \right). \tag{C.8b}$$

Choose an open interval (t_i,t_{i+1}) where the derivatives in (C.8a) exist and σ *is identically zero or nowhere zero. If* $\sigma = 0$ *then (C.7e) implies (C.8a) is an equality. Otherwise*

$$\left| F_r[u_1]'(t) - F_r[u_2]'(t) \right| = \left(F_r[u_1]'(t) - F_r[u_2]'(t) \right) \sigma(t). \tag{C.8c}$$

Since

$$\left| E_r[u_1] - E_r[u_2] \right|'(t) \equiv \left(E_r[u_1]'(t) - E_r[u_2]'(t) \right) \sigma(t), \tag{C.8d}$$

one may add (C.8c) and (C.8d) and apply (C.7e) to prove the assertion. ■

<u>*Lemma C.5 (Lipschitz continuity of F_r and E_r on $W^{1,1}(0,T)$)*</u>

The operators F_r and E_r are Lipschitz continuous on $W^{1,1}(0,T)$ and

$$\left\|F_r[u_1]-F_r[u_2]\right\|_{BV} \le \int_0^T \left|\dot{u}_1(t)-\dot{u}_2(t)\right| dt + 2\left|u_1(0)-u_2(0)\right|, \tag{C.9a}$$

$$\left\|E_r[u_1]-E_r[u_2]\right\|_{BV} \le 2\left\|u_1-u_2\right\|_{BV}, \tag{C.9b}$$

for all $u_1,u_2 \in W^{1,1}(0,T)$.

Proof: Let $u_1,u_2 \in C_{pl}[0,T]$ One infers from Equation (C.8a) that

$$\begin{aligned}
&\int_0^T \left|F_r[u_1]'(t)-F_r[u_2]'(t)\right|dt + \left|E_r[u_1](T)-E_r[u_2](T)\right| \\
&\le \int_0^T \left|\dot{u}_1(t)-\dot{u}_2(t)\right|dt + \left|E_r[u_1](0)-E_r[u_2](0)\right| \\
&\le \int_0^T \left|\dot{u}_1(t)-\dot{u}_2(t)\right|dt + \left|u_1(0)-u_2(0)\right|.
\end{aligned} \tag{C.9c}$$

Adding $\left|F_r[u_1](0)-F_r[u_2](0)\right|$ to both sides one concludes from (C.9a) from (C.6a) that

$$\begin{aligned}
&\int_0^T \left|E_r[u_1]'(t)-E_r[u_2]'(t)\right|dt \\
&\le \int_0^T \left|F_r[u_1]'(t)-F_r[u_2]'(t)\right|dt + \int_0^T \left|\dot{u}_1(t)-\dot{u}_2(t)\right|dt.
\end{aligned} \tag{C.9d}$$

Thus (C.9b) follows from (C.9c). Since $C_{pl}[0,T]$ is dense in $W^{1,1}(0,T)$ both (C.9a) and (C.9b) extend to $W^{1,1}(0,T)$. ■

C.3 Lipschitz Properties of the Memory function

Referring again to Section 3.2 Hysteresis Transforms: An Infinite Series of Basis Functions one may easily comprehend that the memory evolution curves $\lambda(r) := F_r[u;\lambda^0]$ define the boundary between the positive and negative regions of the "Preisach Plane" and contain equivalent information of the state of the basis operator for all points in the plane. Thus the use of the memory evolution function in the integral evaluated along the single dimension *r* is equivalent to integration of the basis function along both dimensions *r* and *s* at any instant, and for all its history. This memory evolution function, integrated along *r* and a σ-finite Borel measure ν *on* $\mathbb{R}_+$, enables one to alternatively evaluate the Preisach and Prandtl-Ishlinskii hysteresis functions.

We introduce the following definitions from Brokate & Sprekels [10]:

- Continuous memory evolution: $\left(F[u;\lambda^0](t)\right)(r) := F_r[u;\lambda^0(r)](t)$.
- Hysteresis operator of Preisach type: $W[u](t) = Q\left(\lambda(t)\right)$ where Q is the "output mapping".
- Memory evolution: $\left(\lambda(t)\right)(r) = F_r[u;\lambda^0](t) = f_r\left(u,\lambda^0(r)\right) = f_r\left(u,w_0\right)$, which implies $\lambda(t)$ is the memory evolution curve $\lambda(t) := F[u;\lambda^0](t)$ at time *t* for all *r*.

__Lemma C.6 (Regularity Properties of the Memory Evolution)__

Suppose that $u_1,u_2 \in C[0,T]$ *and the initial memory curves* $\lambda^{0,1},\lambda^{0,2} \in \Lambda$ *are given, and let* $\lambda_i := F[u_i;\lambda^{0,i}], i = 1,2.$ *Then*

$$\left\|\lambda_1(t)-\lambda_2(t)\right\|_\infty \le \max\left\{\sup_{0\le\tau\le t}\left|u_1(\tau)-u_2(\tau)\right|, \left\|\lambda^{0,1}-\lambda^{0,2}\right\|_\infty\right\} \tag{C.10a}$$

holds. Moreover, for any $u \in C[0,T]$ *and* $\lambda^0 \in \Lambda$, *the memory evolution* $\lambda := F[u;\lambda^0]$ *satisfies*

$$\left\|\lambda(t)-\lambda(t')\right\|_\infty \le \sup_{t'\le\tau\le t}\left|u(\tau)-u(t')\right|,\ 0\le t'\le t\le T. \tag{C.10b}$$

Finally, if $u \in W^{1,1}(0,T)$, *then the distributional time derivative* $\partial_t\lambda$ *belongs to* $L^1((0,T)\times\mathbb{R}_+;\lambda\otimes\nu)$ *for every* σ*-finite Borel measure* ν *and satisfies*

$$\frac{\partial\lambda}{\partial t}(t,r) = F_r[u;\lambda^0(r)]'(t),\ \left|\frac{\partial\lambda}{\partial t}(t,r)\right| \le \left|\dot{u}(t)\right| \tag{C.10c}$$

a.e. in $(0,T)\times\mathbb{R}_+$ *as well as a.e. in (0,T) for every fixed r.*

Proof: The estimates (C.10a) and (C.10b) are direct consequence of Lemma C.2. Equation (C.10c) holds a.e. in t for every $r \ge 0$ *from Equation (C.3d) and Lemma C.5.* ■

The following definitions then formalize our narrative regarding the properties of the memory evolution and transition to integration of the memory function along $r,\nu \in \mathbb{R}_+$.

<u>Definitions C.7:</u>

The σ*-finite Borel measure* ν *on* $\mathbb{R}_+$, *where* $\rho \in L^1(\mathbb{R}_+)$ *is any density function and* γ *is a one dimensional Lebesque measure on* $\mathbb{R}_+$*:*

$$\nu = \int_0^\infty \rho(p)dp\cdot\delta_0 - \rho\gamma. \tag{C.11a}$$

The output mapping for the Prandtl-Ishlinskii function is defined by

$$Q(\lambda) = \int_0^\infty \lambda(r)dv(r). \tag{C.11b}$$

The output mapping for the Preisach function is defined by

$$\begin{aligned} &Q(\lambda) = \int_0^\infty q(r, \lambda(r))dv(r) + w_{00}, \\ &\text{where } q(r,s) = 2\int_0^s \mu(r,\sigma)d\sigma, w_{00} \in \mathbb{R},\ \mu \in L^1(\mathbb{R}_+ \times \mathbb{R}; \nu \otimes \gamma). \end{aligned} \tag{C.11c}$$

The modulus of continuity of output mappings is defined by

$$\eta(\delta; Q) = \sup_{\substack{\varphi,\psi \in \lambda^0 \\ \|\varphi-\psi\|_\infty \le \delta}} \left| Q(\varphi) - Q(\psi) \right| \tag{C.11d}$$

C.4 Lipschitz Properties of the Preisach and Prandtl type operators and derivatives

We state the following *Proposition C.7 and C.8* needed in Chapter 6. In all cases it is assumed that the input to the hysteresis operator, $u \in C_{pm}[0,T]$, is piecewise continuous monotonic. *Proposition C.7* establishes properties of operators of Preisach type, a set including Prandtl-Ishlinskii operators, when the modulus of continuity of the memory function output mapping is bounded. *Proposition C.8* quantifies the bound of the Preisach and the Prandtl-Ishlinskii functions, *and their derivatives*, based on the bounds for the corresponding "relay" basis operator weight function $\mu(r,s)$, *and its derivative*. The condition for the boundedness of the weight functions is thus established, additional to the previous bounded condition on the input.

Proposition C.7: (Regularity properties of Preisach-type Operators)

Let W denote a hysteresis operator of Preisach type associated with the output mapping $Q:\Lambda\to\mathbb{R}$. *Then the following statements (i), (ii) and (iii) hold:*

(i) *If*

$$\lim_{\delta\downarrow 0}\eta(\delta;Q)=0 \tag{C.12a}$$

then W is uniformly continuous on $C[0,T]\times\Lambda$ *and thus maps bounded subsets of* $C[0,T]\times\Lambda$ *onto bounded subsets of* $C[0,T]$.

(ii) *If*

$$\eta(\delta;Q)\le C\delta^{\alpha} \tag{C.12b}$$

for some constants C>0 and $\alpha\in(0,1]$, *then W is* α*-Holder continuous on* $C[0,T]\times\Lambda$. *That is, whenever* $(u_i,\lambda^{0i})\in C[0,T]\times\Lambda,\ i=1,2$, *then*

$$\left\|W[u_1,\lambda^{0,1}]-W[u_2,\lambda^{0,2}]\right\|_\infty\le C\max\left(\left\{\left\|u_1-u_2\right\|_\infty,\left\|\lambda^{0,1}-\lambda^{0,2}\right\|_\infty\right\}\right)^{\alpha}, \tag{C.12c}$$

and W maps bounded subsets of $C^{0,\beta}[0,T]\times\Lambda$ *onto bounded subsets of* $C^{0,\alpha\beta}[0,T]\times\Lambda$ *for any* $\beta\in(0,1]$.

(iii) *If (C.12b) holds for* α*=1, then W is Lipschitz continuous on* $C[0,T]\times\Lambda$ *and maps bounded subsets of* $X\times\Lambda$ *onto bounded subsets of X, where X equals either* $BV[0,T]$ *or* $W^{1,p}(0,T)$ *with* $1\le p\le\infty$, *endowed with their standard norms. And*

$$\left|W[u]'(t)\right|\le C\left|\dot{u}(t)\right| \tag{C.12d}$$

at every $t\in[0,T]$ *where both derivatives exist.*

Proof: To apply Lemma C.6, we let $u_i\in C[0,T]$, $\lambda^{0,i}\in\Lambda$, *and* $\lambda_i := F[u_i;\lambda^{0,i}]$, $i=1,2$ *be given. Then for every* $t\in[0,T]$ *Equation (C.10a) yields*

$$\begin{aligned}&\left|W[u_1;\lambda^{0,1}](t)-W[u_2;\lambda^{0,2}](t)\right|\le\eta\left(\left\|\lambda_1(t)-\lambda_2(t)\right\|_\infty;Q\right)\\&\le\eta\left(\max\left\{\left\|u_1-u_2\right\|_\infty,\left\|\lambda^{0,1}-\lambda^{0,2}\right\|_\infty\right\};Q\right).\end{aligned}\tag{C.12e}$$

Now if any $(u,\lambda^0)\in C[0,T]\times\Lambda$ *is given, setting* $\lambda:=F[u;\lambda^0]$ *(and omitting the assumed reference to* λ^0 *in remainder of proof) one infers from Equation (C.10b) that*

$$\left|W[u](t)-W[u](t')\right|\le\eta\left(\left\|\lambda(t)-\lambda(t')\right\|_\infty;Q\right)\le\eta\left(\sup_{t'\le\tau\le t}\left|u(\tau)-u(t')\right|;Q\right)\tag{C.12f}$$

for any $t,t'\in[0,T]$. *In particular,* $W[u]\in C[0,T]$ *if (C.12a) holds. All the other assertions of (i) follow from (C.12e).*

Next, suppose Equation (C.12b) holds, then one obtains from (C.12f) that

$$\frac{\left|W[u](t)-W[u](t')\right|}{\left|t-t'\right|^{\alpha\beta}}\le C\left(\frac{\sup_{t'\le\tau\le t}\left|u(\tau)-u(t')\right|}{\left|t-t'\right|^{\beta}}\right)^{\alpha}\tag{C.12g}$$

for any $t,t'\in[0,T]$ *with* $\beta\in(0,1]$. *Thus W maps bounded subsets of* $C^{0,\beta}[0,T]\times\Lambda$ *into bounded subsets of* $C^{0,\alpha\beta}[0,T]$. *If Equation (C.12b) is satisfied with* $\alpha=1$ *then (C.12f) implies*

$$\left|W[u](t)-W[u](t')\right|\le C\sup_{t'\le\tau\le t}\left|u(\tau)-u(t')\right|,\ \forall t,t'\in[0,T].\tag{C.12h}$$

Consequently, for any partition $\Delta=\{t_i\}_{0\le i\le N}$ *of* $[0,T]$, *we obtain*

$$\sum_{i=1}^{N}\left|W[u](t_i)-W[u](t_{i-1})\right|\leq C\sum_{i-1}^{N}\sup_{t_{i-1}\leq\tau\leq t_i}\left|u(\tau)+u(t_{i-1})\right|\leq CVar[u]. \tag{C.12i}$$

Hence it follows that the operator W maps bounded subsets of $BV[0,T]\times\Lambda$ *into bounded subsets of* $BV[0,T]$*. Now assume that* $u\in W^{1,1}(0,T)$ *and let* $\varepsilon>0$*. Since u is absolutely continuous there exists some* $\delta>0$ *such that*

$$\sum_{i\in I}\left|t_i-t'\right|_i<\delta\Rightarrow\sum_{i\in I<}\left|u(t_i)-u(t_i')\right|<\varepsilon \tag{C.12j}$$

for any finite collection $\left(\left[t_i',t_i\right]\right)_{i\in I}$ *of disjoint subintervals of [0,T]. Choosing* $\tau_i\in\left[t_i',t_i\right]$ *suitably one finds from Equation (C.12h) that*

$$\sum_{i\in I}\left|W[u](t_i)-W[u](t_i')\right|\leq C\sum_{i\in I}\left|u(\tau)-u(t')\right|\leq C\varepsilon. \tag{C.12k}$$

Hence W is absolutely continuous. Dividing (C.12h) by $\left|t-t'\right|$ *and passing to the limit as* $t'\to t$ *one obtains Equation (C.12d). Since (C.12d) holds a.e. if* $u\in W^{1,1}(0,T)$ *the assertions concerning* $W^{1,p}(0,T)$ *follow.* ■

Proposition C.8: (Regularity Properties of the Preisach and Prandtl functions)

Let P be the Preisach operator having the initial state $\lambda^0\in\Lambda$*. Then the following statements (i) and (ii) hold:*

(i) *If*

$$C_1:=\int_0^\infty\sup_{s\in\mathbb{R}}\left|\mu(r,s)\right|d\left|v\right|(r)<\infty \tag{C.13a}$$

then

$$\eta(\delta;Q) \le 2C_1\delta \tag{C.13b}$$

and $P[u](t)$ *is Lipschitz continuous on* $C[0,T]$. $P[u](t)$ *also maps bounded subsets of X onto bounded subsets of X, where X equals* $C^{0,\alpha}[0,T]$ *with* $\alpha \in (0,1]$, *or* $W^{1,p}(0,T)$ *with* $1 \le p \le \infty$, *or* $BV[0,T]$. *Moreover, for a.e.* $t \in [0,T]$,

$$P[u]'(t) = 2\mu(r, F_r[u,\lambda^0(r)](t)) \cdot F_r[u,\lambda^0(r)]'(t)d\nu(r). \tag{C.13c}$$

In particular,

$$\left|P[u]'(t)\right| \le 2C_1\left|\dot{u}(t)\right| \tag{C.13d}$$

at all points $t \in [0,T]$ *where both derivatives exist.*

(ii) *If* $\dfrac{\partial\mu(r,s)}{\partial s}$ *is measurable and if, in addition to (C.13a),*

$$C_2 := \int_0^\infty \sup_{s\in\mathbb{R}}\left|\frac{\partial\mu(r,s)}{\partial s}\right| d\left|\nu\right|(r) < \infty \tag{C.13e}$$

then

$$\left\|P[u_1]' - P[u_2]'\right\|_{L^1} \le 2\left(C_2\left\|\dot{u}_1\right\|_{L^1} + C_1\right)\left\|u_1 - u_2\right\|_{BV}. \tag{C.13f}$$

Therefore, $P[u](t)$ *is a Lipschitz continuous mapping on bounded subsets of* $W^{1,1}(0,T)$ *and* $P: W^{1,p}(0,T) \to W^{1,p}(0,T)$ *is continuous for* $1 \le p \le \infty$. *For the Prandtl function the above conditions hold if the measure* ν *is finite.*

Proof: By the definition of $P[u](t)$ *one has:*

$$Q(\lambda) = \int_0^\infty\int_0^{\lambda(r)} 2\mu(r,s)dsd\nu(r) + w_{00} \tag{C.13g}$$

so that

$$\begin{aligned} \left|Q(\lambda_1)-Q(\lambda_2)\right| &\le \left|\lambda_1(r)-\lambda_2(r)\right| 2\sup_{s\in\mathbb{R}}\left|\mu(r,s)\right| d\left|\nu\right|(r) \\ &\le 2C_1\left\|\lambda_1-\lambda_2\right\|_\infty . \end{aligned} \tag{C.13h}$$

Except Equation (C.13c) all assertions in (i) follow from Proposition C.7. To prove (C.13c) set $\lambda := F[u,\lambda^0]$ *and observe that*

$$\begin{aligned} &P[u](t)-P[u](0)=\int_0^\infty\int_{\lambda(0,r)}^{\lambda(t,r)} 2\mu(r,s)dsd\nu(r) \\ &=\int_0^\infty\int_0^t 2\mu(r,\lambda(\tau,r))\frac{\partial\lambda}{\partial t}(\tau,r)d\tau d\nu(r) \\ &=\int_0^t\int_0^\infty 2\mu(r,\lambda(\tau,r))\frac{\partial\lambda}{\partial t}(\tau,r)d\nu(r)d\tau. \end{aligned} \tag{C.13i}$$

Now we are ready to prove Equation (C.13f). Let $\lambda_i := F[u_i;\lambda^0],\ i=1,2.$ *From Equation (C.3d), Lemma C.2 and Lemma C.5 one finds:*

$$\begin{aligned} &\left\|P[u_1]'-P[u_2]'\right\|_{L^1} \\ &\le 2\int_0^T\int_0^\infty\left|\mu(r,\lambda_1(t,r))\frac{\partial\lambda_1}{\partial t}(t,r)-\mu(r,\lambda_2(t,r))\frac{\partial\lambda_2}{\partial t}(t,r)\right| d\left|\nu\right|(r)dt \\ &\le 2\int_0^\infty\int_0^T\left(\left|\frac{\partial\lambda_1}{\partial t}(t,r)\right|\sup_{s\in\mathbb{R}}\left|\frac{\partial\mu}{\partial s}(r,s)\right|\left|\lambda_1(t,r)-\lambda_2(t,r)\right|\right. \\ &\qquad\left.+\sup_{s\in\mathbb{R}}\left|\mu(r,s)\right|\left|\frac{\partial\lambda_1}{\partial t}(t,r)-\frac{\partial\lambda_2}{\partial t}(t,r)\right|\right)dtd\left|\nu\right|(r) \\ &\le 2\left\|u_1'\right\|_{L^1}C_2\left\|u_1-u_2\right\|_\infty+2C_1\left\|u_1-u_2\right\|_{BV} \end{aligned} \tag{C.13j}$$

from which Equation (C.13f) follows.

Next suppose that $u_n \to u$ *in* $W^{1,p}(0,T)$ *for some fixed* $p\in(1,\infty)$. *From the proof of (C.13f) one infers that*

$$P[u_n]' \to P[u]' \text{ in } L^1(0,T). \tag{C.13k}$$

Since

$$\left|P[u_n]'(t)\right| \le 2C_1 \left|\dot{u}_n(t)\right|, \text{ a.e. in } (0,T) \tag{C.13l}$$

and since $\dot{u}_n \to \dot{u}$ *in* $L^p(0,T)$ *Lebesque's theorem yields*

$$P[u_n]' \to P[u]' \text{ in } L^p(0,T). \tag{C.13m}$$

Hence $P[u](t)$ *is continuous on* $W^{1,p}(0,T)$. *Finally, in the case of the Prandtl function one has* $\mu = \dfrac{1}{2}$ *and* $w_{00} = 0$, *thus Equation (C.13a) and (C.13e) are satisfied if* ν *is finite. This concludes the proof.* ■

<u>*Conclusion*</u>

The proofs in this Appendix C then establish the bounded behavior of the Preisach and Prandtl-Ishlinskii hysteresis functions *and their derivatives*. This bounded behavior, and the conditions which lead to this bounded behavior, support the BIBO stability proof for the LADRC control of the hysteretic system in Chapter 6.